

Review

Cold Spray Coatings of Complex Concentrated Alloys: Critical Assessment of Milestones, Challenges, and Opportunities

Desmond Klenam ^{1,2}, Tabiri Asumadu ³, Michael Bodunrin ², Mobin Vandadi ⁴, Trevor Bond ⁵,
Josias van der Merwe ², Nima Rahbar ^{4,5} and Wole Soboyejo ^{5,*}

- ¹ Academic Development Unit, Faculty of Engineering and the Built Environment, University of the Witwatersrand, 1 Jan Smuts Avenue, Johannesburg 2001, South Africa
² School of Chemical and Metallurgical Engineering, University of the Witwatersrand, 1 Jan Smuts Avenue, Johannesburg 2001, South Africa
³ Department of Materials Engineering, Sunyani Technical University, Sunyani P.O. Box 206, Ghana
⁴ Department of Civil Engineering, Worcester Polytechnic Institute, 100 Institute Road, Worcester, MA 01609, USA
⁵ Department of Mechanical Engineering, Worcester Polytechnic Institute, 100 Institute Road, Worcester, MA 01609, USA
* Correspondence: wsoboyejo@wpi.edu; Tel.: +1-508-831-4694

Abstract: Complex concentrated alloys (CCAs) are structural and functional materials of the future with excellent mechanical, physical, and chemical properties. Due to the equiatomic compositions of these alloys, cost can hinder scalability. Thus, the development of CCA-based coatings is critical for low-cost applications. The application of cold spray technology to CCAs is in its infancy with emphasis on transition elements of the periodic table. Current CCA-based cold spray coating systems showed better adhesion, cohesion, and mechanical properties than conventional one-principal element-based alloys. Comprehensive mechanical behavior, microstructural evolution, deformation, and cracking of cold spray CC-based coatings on the same and different substrates are reviewed. Techniques such as analytical models, finite element analysis, and molecular dynamic simulations are reviewed. The implications of the core effects (high configurational entropy and enthalpy of mixing, sluggish diffusion, severe lattice distortion, and cocktail behavior) and interfacial nanoscale oxides on the structural integrity of cold spray CCA-based coatings are discussed. The mechanisms of adiabatic heating, jetting, and mechanical interlocking, characteristics of cold spray, and areas for future research are highlighted.

Keywords: complex concentrated alloys; cold spray; adiabatic heating; solid-state coating; metallurgical bonding; mechanical interlocking; severe lattice distortion; Johnson–Cook model; finite element method; sluggish diffusion; microstructural evolution



Citation: Klenam, D.; Asumadu, T.; Bodunrin, M.; Vandadi, M.; Bond, T.; van der Merwe, J.; Rahbar, N.; Soboyejo, W. Cold Spray Coatings of Complex Concentrated Alloys: Critical Assessment of Milestones, Challenges, and Opportunities. *Coatings* **2023**, *13*, 538. <https://doi.org/10.3390/coatings13030538>

Academic Editors: Ashish Kumar Srivastava and Amit Rai Dixit

Received: 30 January 2023

Revised: 21 February 2023

Accepted: 24 February 2023

Published: 1 March 2023



Copyright: © 2023 by the authors. Licensee MDPI, Basel, Switzerland. This article is an open access article distributed under the terms and conditions of the Creative Commons Attribution (CC BY) license (<https://creativecommons.org/licenses/by/4.0/>).

1. Introduction

Complex concentrated alloys (CCAs) are the new frontier for the design of bulk materials and coatings for structural and functional applications [1–5]. This approach by design has disrupted ~5000 years of conventional and serendipitous material discovery processes. The CCA design approach is based on mixing elements in equal amounts without any distinct solvent and solute atoms [5]. This is counterintuitive to the well-established physical metallurgy of using one or two base elements, while systematically adding minute secondary alloying elements to induce the designed and desired properties. These properties could be mechanical, corrosional, thermal, magnetic, electrical, and physical. The approach deviates from exploring compositions at the corners of typical ternary and higher order phase diagrams. This new approach shows promise and is being touted as the future of materials, providing superior structural and functional properties to most conventional alloys [1].

Cold spray is classified as a thermal spray coating technique and an additive manufacturing process [3,6–16]. The technique has been used to deposit coatings [7,9,17,18], to repair materials [6,8,19], and for design of bulk materials for various structural and functional applications [14–16]. The main advantages are: (i) easily applicable to a wide variety of ductile, dissimilar, and thermally sensitive materials, (ii) able to retain initial properties of the feedstock powder material, (iii) high flexibility and precise near-net shape manufacturing, (iv) deposits possess cold-worked microstructural features contributing to high hardness and relatively low porosity, and (v) superior deposition efficiency and rates compared to other types of conventional coating process. Lastly, the method has the unique characteristic of being operated under relatively low temperature (below the melting temperature) of the coating material. The layer-by-layer deposition satisfies the principles of additive manufacturing.

The inherent design principles of bulk materials from CCAs make them expensive compared to most conventional structural and functional alloys [1,2,20]. This hinders scalability and stiff competition from commercially available conventional alloys is inevitable [2,20]. To reduce overall costs, coatings using various techniques are being explored.

Cold spray technology is gaining traction and has been commercialized for various functional and structural applications as coatings and for bulk alloy design. It is instrumental for material repair. As one of the hotspot research areas, there has been increased and timely experimental and published literature on the subject. Since its discovery over 40 years ago in Russia, there have been thematic reviews, book chapters, and books on various aspects of cold spray technology [3,6,9,10,17,21–26]. These ranged from fundamental principles and applications to material perspectives [9,21–25]. Some of the reviews focused on various bonding mechanisms [6,17,27]. The latest review on the bonding mechanism focused on single-particle impact approaches [17]. Similarly, there have been lab-scale experimental approaches augmented with numerical simulations to understand the process better.

Bulk CCAs are expensive with stiff competition from dilute conventional alloys. The design of CCA-based coatings is one of the solutions to reduce the cost. Various types of CCA-based coatings have been developed and reviewed. The cold spray approach, since its proof of concept on CrCoFeMnNi alloy in 2019, is still in its infancy. Apart from a mini review of structural integrity and material aspects of CCA-based cold spray coating published by the authors [3], there is yet to be published a general overview, which critically assesses the current stage of knowledge in the area. This is ideal in highlighting areas for future research direction. By combining the advantages of CCA-based coating and the cold spray technique, robust and next generation multifunctional coatings can be developed and applied in various industries.

2. Thermal Spray Technology—Brief Overview

Thermal spray coating is a coating process that sprays the surface of any substrate with melted or heated particulate matter [28,29]. The thermal energy that heats or even melts the feedstock (precursor coating material) is generated via electrical or chemical means. The molten or heated (semi-molten) particulate matter possesses kinetic energy which helps in accelerating the particles onto the substrate. Adhesion and cohesion are induced by the high temperature and high velocity of the particle which in effect leads to severe plastic deformation. The deformed coating material produces a splat on the substrate, which is a pancake-like impacted particle. The bonding mechanisms are: (i) mechanically induced bonding of the coating particles' splatter on substrate with an interlocking effect, (ii) localized diffusion of the coating and the substrate material, and (iii) bonding is achieved from the interactions of the van der Waals forces of attraction. The main benefits are the ability to repair and strengthen damaged surfaces and high applicability to metals and ceramics. It also requires less heating for effective bonding at the coating and substrate interface. A schematic diagram showing the process is given in Figure 1.

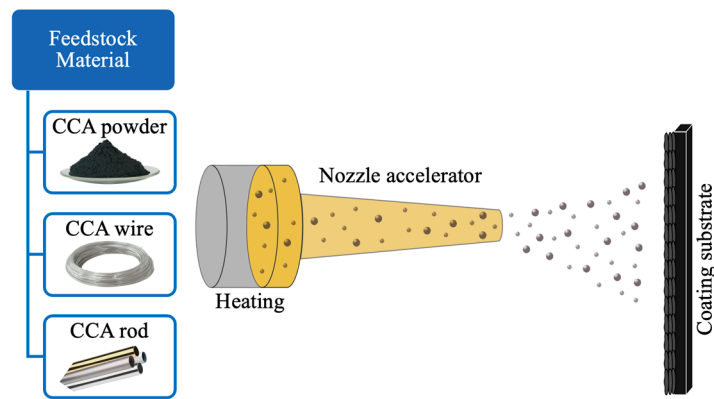


Figure 1. Schematic diagram showing the thermal spray process.

Thermal spray coatings are in three categories based on application of combustion heat sources (flame, detonation gun, and high-velocity oxygen fuel spray), electrical energy sources (plasma or an arc) and thermal energy sources (kinetic, cold, and hypersonic spray) from gas expansion. The classification of thermal spray based on the interdependence of multiplicity of input variables is represented by a process map (Figure 2) [29]. These input variables include the particle temperature at optimized stand-off distance, the particle velocity, and feedstock particle size distribution with its associated physical and mechanical properties [29]. The process map provides a guide for the classes of materials and the suitability of the coating method and their effects on porosity and cohesion strength. The relatively high operation temperatures of conventional thermal spray coatings have some drawbacks. These include high tensile residual stresses, high oxidation rates, defects nucleated in the form of cracks, and phase transformation. These features affect the mechanical, chemical, and physical properties of the coating, hence some of these coatings cannot be used in temperature-sensitive operations. The development of cold spray coatings is one of the ways to minimize the challenges posed by other thermal spray processes.

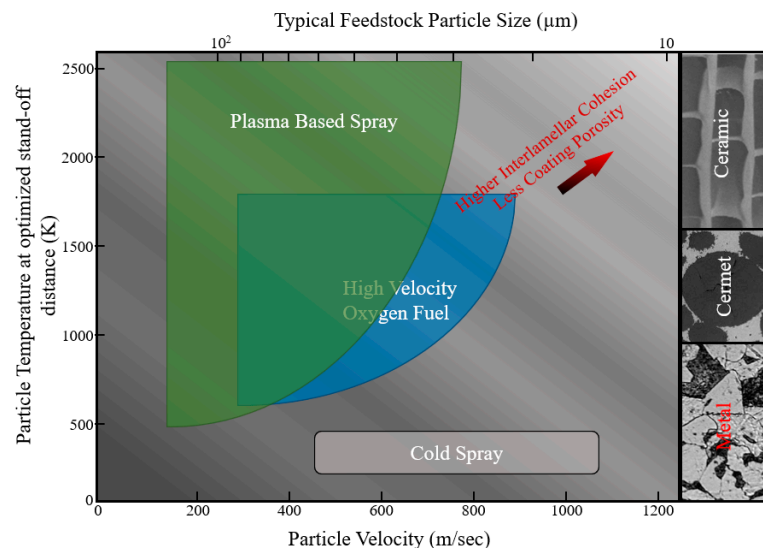


Figure 2. Classification of thermal spray coating methods based on processing parameters such as particle velocity, feedstock particle size distribution, and particle temperature at optimized stand-off distance.

3. Cold Spray Technology: An Overview

3.1. Introduction and General Concepts

The cold spray process of thermal spray coating was discovered and operationalized in 1980s. It is based on the principle that when a particle-laden supersonic gas jet impinges

onto a solid substrate above a critical minimum particle velocity, there is a transition of the metallic particles from a state of abrasion to adhesion, which through plastic deformation are deposited on the substrate. These minute unmelted particles are typically in a size distribution range of approximately 1–50 μm . The system was fully commercialized after the Russian and United States patents were granted. The technological and innovation timeline of cold spray is given in Figure 3 with a project plateau of productivity by 2030.

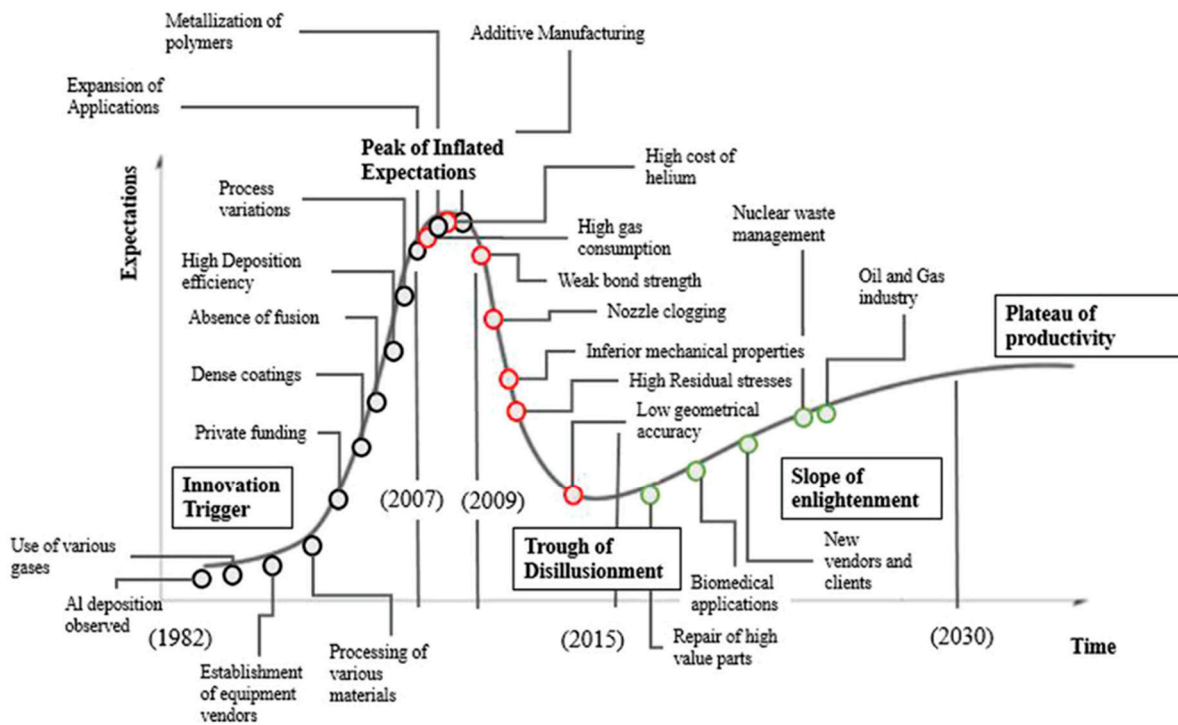


Figure 3. Technology and innovation maturation timeline and projection for cold spray technology [9].

The operational principle is as follows with the schematic diagram shown in Figure 4. The whole architecture of the system is built on high pressure (Figure 4a) [15]. However, recent modification led to the low-pressure system as shown in Figure 4b. Based on Figure 4a, high-pressure gas, which is typically, air, nitrogen, or helium, enters the system and then splits into 5 and 95%. The 5% of the gas goes to the particle feeder adding particles to the flow, whereas the 95% goes to the gas heater. The gas is heated to ~ 500 to 1000 $^{\circ}\text{C}$ and the two streams recombine at the converging–diverging nozzle (the same as that used in rocket engines, which is called a de Laval nozzle) entrance, then accelerated through the nozzle. The velocity at the nozzle entrance is generally low which increases to as much as ~ 1000 m/s depending on the gas used. In the case of He, the velocity is very low as He is relatively lighter than nitrogen. The stream then impinges on the substrate while the gas turns away, whereas the particles crash on the surface of the substrate due to the high momentum they possess. The longer the flow is kept, the thicker the deposit. The working principle of cold spray is based on the conservation of energy. The impacting feedstock material possesses kinetic energy, which is converted to heat and deformation energies, causing localized severe plastic deformation upon impact. The heat energy is then transferred to the surface of the substrate, resulting in some adiabatic heating but not high enough to induce phase transformation.

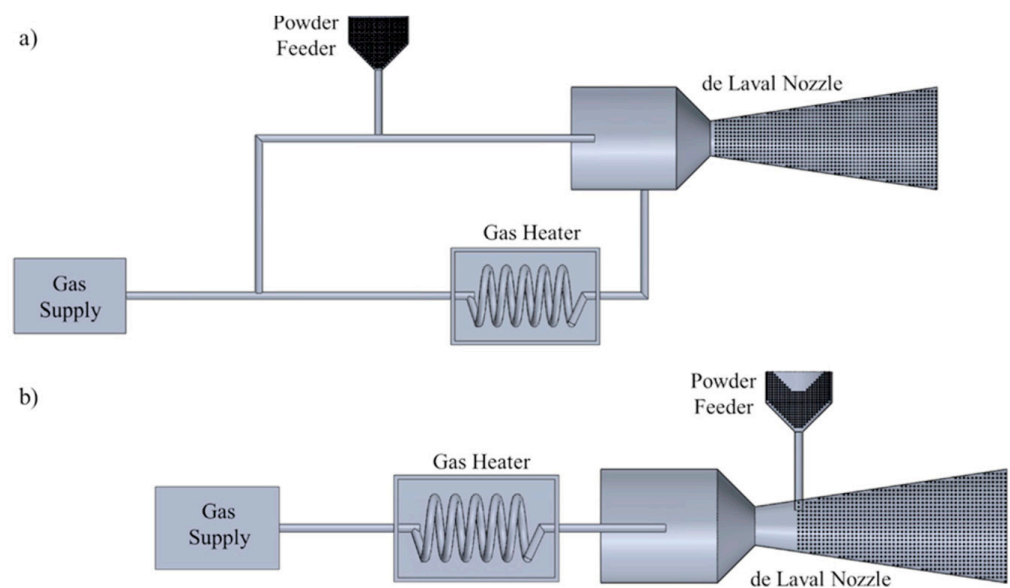


Figure 4. Schematic diagram showing typical cold spray system showing (a) high-pressure and (b) low-pressure systems. Reprinted with permission from Ref. [3]. Copyright 2022, Elsevier.

The gas is heated to take advantage of the supersonic nozzle design. The nozzle converts the high thermal energy of the gas to kinetic energy at the exit of the nozzle. Thus, the process starts with a hot but slow mixture of gases and feedstock particles at the entrance of the nozzle and ends with a cold fast mixture at the exit. Generally, temperatures as high as 500 °C can be observed at the entrance of the nozzle but they reduce drastically to ~100 °C at the exit of the nozzle, resulting in no melting of the feedstock particles. Therefore, it is a solid-state process of surface coating where deposition of coating can occur from 0 to 800 °C, which is lower than the melting point of the feedstock.

3.2. Processing Parameters of Cold Spray Coatings

Typical cold spray processes have been used to manufacture various bulk mechanical components [10–16]. Among these components are flanges, cylindrical walls, tubes, heat exchanger array fins, and metal labels. The flexibility of the coating process and no detrimental effect on the substrate make it applicable for repair of worn parts of any mechanical component. As a form of additive manufacturing process, comparative analyses of the techniques with three methods of fusion-based additive manufacturing are given in Table 1. The comparison was also made using as-fabricated (AF) and heat treatment (HT) specimens.

Table 1. Comparison of cold spray technology with three methods under powder-based additive manufacturing process.

Property and Parameter	Cold Spray	SLM	EBM	LMD
Powder feed mode	Direct deposition	Powder bed	Powder bed	Direct deposition
Feedstock drawback	Difficult to process high-strength materials	Difficult to process poorly flowable and highly reflective metals	Not suitable for low-melting and non-conductive metals	Difficult to process for highly reflective metals
Powder melting	Not applicable	Applicable	Applicable	Applicable
Product size	Large	Limited	Limited	Large
Dimensional accuracy	Low	High	High	Medium
As-fabricated mechanical properties	Low	High	High	High

Table 1. *Cont.*

Property and Parameter	Cold Spray	SLM	EBM	LMD
Heat treated mechanical properties	High	High	High	High
Production time	Short	Long	Long	Long
Flexibility of equipment	High	Low	Low	Low
Possibility of material repair	Applicable	Not applicable	Not applicable	Applicable

SLM—Selective Laser Melting, EBM—Electron Beam Melting, and LMD—Liquid Metal Deposition.

Gas propulsion parameters are required to accelerate the particles of the powder required to bombard the substrate to induce bonding. The parameters are the nature, type, temperature, and pressure of the gas system. For instance, the pressure of the gas is used to classify cold spray technology as either a high- or low-pressure cold spray system. The high-pressure cold spray system has pressures exceeding 1 MPa. The effects of processing parameters of cold spray coating are summarized in Table 2.

Table 2. Effects of the processing parameters on defects, adhesion, and deposition efficiency of cold spray coatings.

Parameter	Porosity	Residual Stress	Adhesion	Deposit Strength and Efficiency
Pressure of gas	↓	↑	↑	↑
Gas temperature	↓	↑	↑	↑
Gas molecular weight	↑	↓	↓	↓
Particle velocity	↓	Inconclusive	↑	↑
Powder feed rate	↑	↑	↓	↓
Spray angle	↑	↑	↑	↑
Stand-off distance	Effect is inconclusive and indiscernible			

Note: ↑ shows an increase whereas ↓ shows a decrease in most observed experiments.

The effect of particle velocity on residual stresses in the cold spray method is inconclusive for most systems studied [30–38]. The three main residual stress states are peening, thermal, and quenching stresses [31,32,38]. The high-impact velocity of the impinging particles contributes to the peening effects [30]. The mechanism is likened to shot peening for increased fatigue strength in most structural components [38–44]. The quenching stresses are attributed to the compaction of impacted particles often impeded or restricted by the underlying coatings or substrate materials. Thermal stresses are due to differences in the coefficient of thermal expansion (CTE) of the substrate and coating materials. Based on the magnitude of the CTE mismatch of the coating and substrate, tensile or compressive residual stresses can be induced [38,45]. Typical compressive residual stresses are observed in the coatings and tensile stresses in the substrate when $CTE_{\text{substrate}} > CTE_{\text{coating}}$ [29]. Due to the low deposition temperature of the cold spray coating technique, the cumulative effects of thermal and quench stresses are negligible [29]. However, these effects are pronounced when the temperature of the substrate is above 400 °C and, vice versa, below 400 °C [29].

There is no clear and discernible relationship between residual stresses and impact velocity from both experiments and simulations [33–38,46]. In most instances, residual stresses increase with increasing particle velocity [33,34,36,37], but that is largely dependent on substrate-to-coating pairs and microstructural characteristics. However, this opens opportunities for further research to optimize the process parameters to obtain properties within acceptable limits. A typical example is Cu coatings on Cu substrate, where the difference in CTE is negligible [35]. The residual stresses increased with increasing impact velocity from 300 to 500 m/s. However, when particle velocities increased from 500 to

700 m/s, no discernible relationship was observed. For a Cu/Al substrate–coating pair, residual stresses increased for particle velocities between 300 and 500 m/s. The compressive residual stresses were increased for particle velocities between 500 and 700 m/s [35]. A similar trend of increasing residual stresses with increasing particle velocities has been reported for Ti6Al4V on Ti6Al4V [46]. The residual stress profiles for particle velocities from 700 to 800 m/s were comparable.

Particle size, distribution, and morphology: This is a useful parameter which affects the deposition behavior and quality of cold spray coatings [47]. It is characterized by the particle size, distribution, and morphology. The acceleration of large particles is poor due to the lower velocity of the particles compared to small particles. However, the larger the particle size, the easier it is to reach high temperatures, which contributes to reduced critical velocities [47]. A schematic diagram showing the effect of particle size on the particle impact velocity is given in Figure 5 [48]. There is always an optimum particle size range that impacts the substrate above the critical velocity and below erosion velocities. The optimized particle size range, which is specific to the coating material, leads to good adhesive, cohesive, and quality coatings.

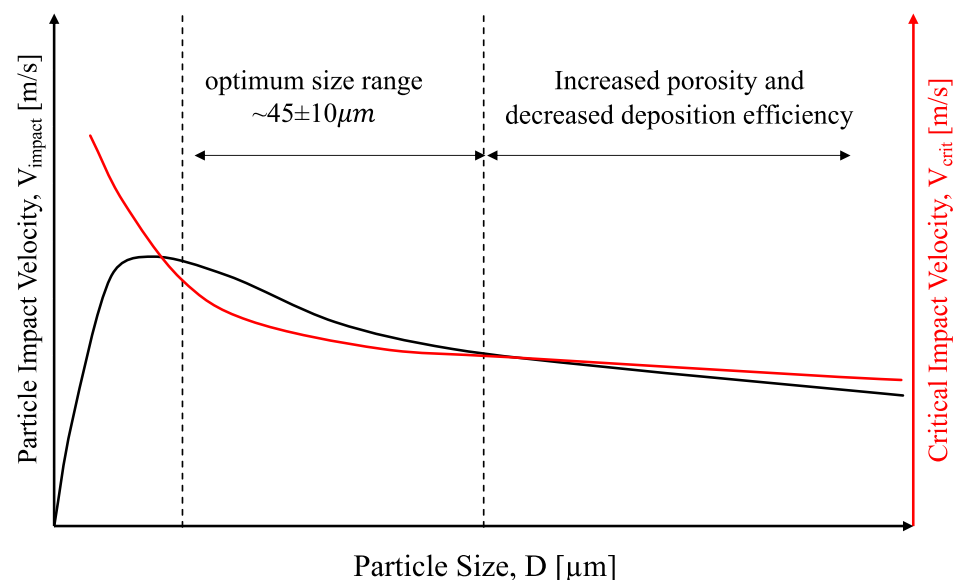


Figure 5. Effect of particle size distribution on the particle impact velocity during a cold spray deposition [49].

3.3. Bonding Mechanisms of Cold Spray of Metallic Materials

The bonding mechanism of cold spray technology shows how the coating and substrate achieve adhesion and cohesion [17,27,47]. While it is known to be a solid–solid bond interaction, the overarching bonding mechanisms are still a bone of contention. However, the core mechanism is based on the ballistic impingement theory where particles are consolidated into coatings on substrate by ballistic impingement [50]. Two main conditions for the theory are the need for particles of certain sizes (below 5 mm) to be accelerated to certain critical velocities ($50\text{--}3000\text{ ms}^{-1}$) to induce impact [50,51]. The high kinetic energy impingement of the particle on the substrate results in increased plastic strain and strain rates. Upon impact, the kinetic energy is converted to heat and sound which induce adiabatic heating leading to thermal softening and dynamic hardening effects. There are few reviews on the subject focusing on particle–substrate and particle–particle interactions and bonding mechanisms [52–57]. Metallurgical bonding has been observed using various microstructural characterization techniques [17,27,47,52,53,55–57]. These include scanning and transmission electron microscopy [55,58,59] and various empirical models [48,56,57] have been developed to explain the mechanism.

The schematic representation of the bonding mechanism of a typical cold spray process (tantalum particle on 4340 steel substrate) is given in Figure 6. The process commences with high kinetic energy of the impinging particles from the high velocities and high pressures, generating extreme plastic deformation at the surface of the contact region. This process disrupts any thin surface oxides and exposes clean surfaces of the substrate, aiding the metallurgical bonding process (Figure 6). As the impact progresses, the plastic flow of the materials at the interface extrudes much of the crushed pieces of oxide films to the periphery of the contact interface, enabling an intimate contact of newly exposed clean metal between the particle and substrate (Figure 6). Some of the oxides are removed from the interface altogether through “jetting” observed for particle impacts above the critical velocity. This is shown experimentally in a wide range of engineering materials. For a strong bond to be achieved in non-ductile materials, the systems require the addition of ductile matrix to induce metallurgical bonding and mechanical interlocking, which are critical for adhesion strength [53,54,57].

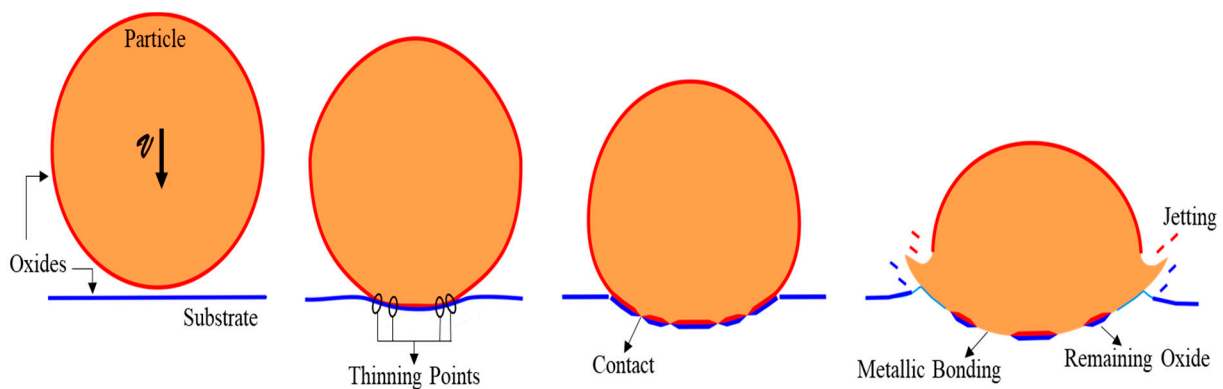


Figure 6. Schematic showing the bonding mechanism of a typical cold spray process.

The presence of oxide-free surfaces due to the initial particle–substrate is the precursor for metallurgical bonding. Surface preparation methods are used to create the oxide-free surfaces. Jetting contributes to removal of interfacial oxides. For many materials, the bulk plastic deformation of particle and substrate results in mechanical interlocking, a characteristic bonding mechanism. Typical bonding strength of cold spray coatings ranges from 10–60 MPa [57]. For the bonding mechanism to be effective, the following conditions should be met [47,52,55,57]:

- The velocity of the particles should be higher than a critical nominal velocity (critical velocity) to induce sufficient kinetic energy, a characteristic of velocity for enough plastic deformation to initiate the interaction between the particle and oxide films on substrate. There are instances where there are no oxide layers, but the particle critical velocity is crucial for cold spray.
- The kinetic energy of the particle upon impact should be lower than the required energy needed to melt the coating particle. Thus, there should not be any melting for the solid-state deposition mechanism [17,27,48,55,56].

The cold spray process is a solid-state process without any element of melting. However, there is localized heating when the particle impinges on the substrate. This is known as adiabatic shear instability (ASI). This is a critical contribution factor to the overall bonding mechanism and strength of the coating. The high strain rates at which the particles are accelerated onto the surface of the substrate result in the localized adiabatic heating.

4. Computational and Numerical Simulation Models—An Overview

Three main types of models are used to simulate the cold spray processes. These include the finite element-based models, constitutive equations, and models for describing

the bonding at the particle–substrate and particle–particle interfaces [39,58]. A summary of the models and their applications to cold spray processes are highlighted.

4.1. Modeling Approaches Using Numerical Simulations

The numerical approaches used for simulating the cold spray processes focus on impact and deformation associated with particle–substrate and particle–particle interaction [17,27,60–73]. The main numerical methods are the Lagrangian [74,75], Eulerian [17,27,60,61,63,64], coupled Eulerian–Lagrangian [57,61,62,76,77], smooth-particle hydrodynamics [65–73], and molecular dynamics [17–19,38].

4.1.1. Lagrangian Approach

The Lagrangian finite element-based approach applies mesh which deforms with the material under applied loads [59]. Tracking particle–substrate and particle–particle interaction is easy during impact even if complex boundary conditions are imposed [74,75]. It is also a good approach to trace any history-dependent variables, hence it is one of the pioneering approaches for simulating solid-state bonding processes. It is widely used due to reduction in computational time as the impact process is assumed as symmetric and quarter (axisymmetric) models are representative and cost effective [38].

The Lagrangian model is great for showing material jetting, which is characteristic for most impact-induced bonding. Although the jets are sharp and sharps are unphysical, they result in severe mesh distortions. This severe distortion of the meshes could compromise the simulation, resulting in premature termination and reducing computational accuracy significantly [60,75,78], sometimes at 19 ns [60]. Severe mesh distortion can be attributed to large strains imposed on the structure, resulting in failure, attributed to near-zero or negative element Jacobians. Localized strains could be as high as 450% in the jetting region, which could lead to overestimation of the bond modeling.

Ways to mitigate the mesh distortion have been explored [57,61,62]. One approach is the use of the arbitrary Lagrangian–Eulerian (ALE) which combines the Lagrangian and Eulerian analyses [59]. The ALE allows for the redefinition of the mesh in a continuous fashion arbitrarily while moving the mesh away from the material. The major challenges associated with the ALE technique are high computational cost [17,27,57,59], unrealistic deformation of particles at high impact velocities [61,62], inaccurate prediction of the particle–particle interactions, and overall reduction in equivalent plastic strains [17,27,60,63]. For the ALE method, the inherent interpolation errors are due to high strain gradients at the particle–substrate interface and adaptive remeshing [60]. In a nutshell, the pure Lagrangian approach is not the ideal technique for a high-strain cold spray modeling process.

4.1.2. Eulerian Approach

The Eulerian approach to modeling cold spray processes improves on the inefficiencies of the pure Lagrangian formulation [27,61,64], thus solving the severe mesh distortions and large deformations induced by high strains. The Eulerian approach allows the flow of material mass through stationary points where deformation is independent of the material [64]. This process assumes two overlapping meshes where one is fixed as the background and the other, mesh for the material which allows flows through it easily. The model is flexible, allowing for assigning different parameters to the different parts of the model. Due to the ease of flowability of the material in the mesh, it is easy to model the severe plastic deformation associated with the cold spray process. The error associated with the Eulerian approach is negligible compared to experimental data [64]. For instance, the predicted critical velocity of Cu was compared to the experimental value. It is the right method for modeling the material jetting process of the particle and the substrate. Generally, the demerits associated with this method are long simulation and computational times due to the fine mesh and severe plastic deformation, the difficulty with modifying boundary conditions, and the inability to modify contact properties such as the coefficient of

friction [64]. The inability to track the history-dependent variables in the Eulerian method and numerical dissipation are also possible shortcomings.

4.1.3. Combined (Coupled) Eulerian–Lagrangian Approach

This approach uses the Eulerian and Lagrangian approaches simultaneously to model aspects of the cold spray process [59,64,76,77]. This allows for the merits associated with each technique to be applied in a robust fashion, thus, solving the false positives or impractical results associated with particle–substrate deformation and mesh distortions associated with the Lagrangian method, while being able to track the particle–substrate interface, which is difficult under the Eulerian method. For the Eulerian part, the volume of fluid method is applied [77].

4.1.4. Particle-Based Approach

The particle-based approach is ideal for modeling severe plastic deformation associated with the cold spray process [65–67]. Results from this technique are comparable to experiments that do not underestimate, or overestimate, as observed for most mesh-based techniques [65,66,69]. The approach possesses merits that are not observed for the conventional mesh-based FEM Lagrangian and Eulerian methods [66,67]. A typical example is the smoothed particle hydrodynamics (SPH), a meshless discretization process that deviates from finite 3D meshed elements to discretized particles, the carrier of the information [65–68]. The particles are assigned state variables which describe material based on weight, velocity, and stress states. An authoritative review of the mathematical underpinnings of the SPH [66–70] and key advantages are as follows:

- The SPH, being a particle-based method, allows for the handling of large deformations. This is because connections between the particles are generated as part of the computations and changes with time, especially for the high-velocity impact phenomenon which underpins cold spray technology.
- The SPH method has been successfully applied to conceptualized problems with deformable boundaries with extremely large deformations, free surface, and moving interfaces.
- The SPH is a particle approach of the Lagrangian kind with the Galilean invariant algorithm. It can easily estimate time history of the particles of the material, which are relevant for determining the transport and advection of the system.
- The SPH method, being one of the oldest mesh-free particle methods, has approached maturation and been successfully integrated into commercial software packages for practical applications.
- The SPH is ideal for free surface and interfacial flow modeling characteristics with the cold spray process. The specific location of the particles prior to the commencement of any analysis is critical. This leads to accurate and easily traceable material interfaces and free surfaces by the SPH simulation irrespective of the complexity of the particle movement and interaction, which may be challenging for mesh-based methods.
- The SPH approach is extensively used in applications ranging from the microscale to macroscale and even astronomical scale, and in discrete to continuum systems. It is easy to combine with other methods such as classical molecular dynamics and dissipative particle dynamic methods for various applications.
- Numerical simulations associated with SPH have the objects not under continuum, which is vital for bio- and nanoengineering across the nano- to the microscale.
- The SPH method is comparatively easy to implement and to use to develop 3D numerical models than the mesh-based approaches. It has also gained an acceptable level of accuracy for practical engineering applications.

Considering that SPH is a mesh-free technique, an important factor is the interpolation theory. This is the process where continuum fluid dynamics laws of conservation are converted to integral equations with an interpolation function. While the application of the shape functions is difficult to implement, a weighting SPH kernel function according

to Equation (1) is applied [19,71–73]. Thus, kernel approximation of the function $f(r')$ at specific positions is obtainable by using smooth kernels, W , which are integrated over a certain computational domain. Other governing equations and detailed assumptions are documented elsewhere [66,69,72].

$$f(r) = \int f(r')W(r - r', h)dr' \tag{1}$$

where: W = weighting function, h = support scale satisfying the normalization process when $\int W(r - r', h)dr' = 1$, the delta function property achieved when smoothing length tends to zero is given as $\lim_{h \rightarrow 0} W(r - r', h) = \delta(r - r')$.

Some of the different interpolation kernels used in SPH modeling are given in Table 3 [66,79–81]. These kernel expressions cater for 2D domains only. Typical factors to consider in deciding the type to use are the desirable mathematical behavior and the lack of complexity to adequately describe the properties of the particle. Detailed derivation and the mathematical underpinnings of the kernel function have been summarized elsewhere [66]. The material parameters used for the SPH simulations include material properties (density, Young’s modulus, and Poisson ratio), strength parameters (yield strength, hardening coefficient, strain rate constant, softening exponent, strain hardening exponent, heat capacity, thermal conductivity, melting and reference temperatures, reference strain rate) and equation of state (EOS) parameters (speed of sound, gradient of shock velocity, and Gruneisen coefficient).

Table 3. Typical interpolation kernels used for SPH modeling.

Kernel Name	Mathematical Expression [$W(r, h)(m^{-2})$]
Cubic spline kernel [66]	$\frac{15}{7\pi h^2} \left\{ \begin{aligned} & \left[\frac{2}{3} - \left(\frac{ r-r_b }{h}\right)^2 + \frac{1}{2} \left(\frac{ r-r_b }{h}\right)^3 \right], 0 \leq r - r_b \leq h \\ & \left[\frac{1}{6} \left(2 - \frac{1}{2} \left(\frac{ r-r_b }{h}\right)^3 \right) \right], h \leq r - r_b \leq 2h \end{aligned} \right.$
Quartic kernel [81]	$\frac{5}{\pi h^2} \left\{ 1 + 3 \left[\left(\frac{ r-r_b }{h}\right) \right] \left[1 - \left(\frac{ r-r_b }{h}\right) \right]^3, 0 \leq r - r_b \leq h \right.$
Quartic kernel [80]	$\frac{15}{7\pi h^2} \left\{ \frac{2}{3} + \frac{9}{8} \left(\frac{ r-r_b }{h}\right)^2 + \frac{19}{24} \left(\frac{ r-r_b }{h}\right)^3 - \frac{5}{32} \left(\frac{ r-r_b }{h}\right)^3, \right.$ $0 \leq r - r_b \leq h$
Quintic spline [79]	$\frac{7}{478\pi h^2} \left\{ \begin{aligned} & \left[3 - \left(\frac{ r-r_b }{h}\right) \right]^5 - 6 \left[2 - \left(\frac{ r-r_b }{h}\right) \right]^5 + 15 \left[1 - \left(\frac{ r-r_b }{h}\right) \right]^5, \\ & \quad 0 \leq r - r_b \leq h \\ & \left[3 - \left(\frac{ r-r_b }{h}\right) \right]^5 - 6 \left[2 - \left(\frac{ r-r_b }{h}\right) \right]^5, \\ & \quad 0 \leq r - r_b \leq 3h \\ & \left[3 - \left(\frac{ r-r_b }{h}\right) \right]^5, 2h \leq r - r_b \leq 3h \end{aligned} \right.$

Some examples of SPH models for cold spray include SPH simulation of cold spray oblique impacting Cu particles which showed well-fitted results to the experimental data [72]. The issues of mesh distortions were completely avoided when the SPH method was applied [72]. There was reduced dependency on the particle weight in the case of the SPH technique compared to the mesh based Lagrangian methods [73]. The effect of interfacial oxide layers on the impact processes during the cold spray was investigated using the particle based SPH technique [65]. Excessive deformation, complex time evolution associated with free surfaces, and large thermal transport processes associated with the mesh based Lagrangian FE model were overcome using the SPH approach [65,66,69,70].

Ceramic particles were deposited using cold spray at room temperature and studied using the SPH [82]. The contact surfaces were free, which was vital in predicting critical velocities and their effects on deposition efficiency. Two main mechanisms were observed through simulation and experiment, which are fragmentation from the submicron- to the

nanoscale and the bombardment of the submicron particles, providing enough bonding energy as pressure and thermal energy for the fragmented particles through the shock waves [82–84]. Although the deformation behavior was adequately simulated, the method was not appropriate for determining the critical and maximum velocities. The technique provided the basis for understanding the deposition behavior numerically.

An SPH and experimental study on cold spray between similar and dissimilar substrates was carried out [84,85]. The ratio of the deposition and rebound energy was used for the cold spray coating evaluation based on porosity rate, hardness, and bonding strength. The quality of the coating on similar metals was better than those of similar metals, as predicted based on high deposition energy and low rebound energy. The effect of interfacial oxides has also been studied using the SPH approach and the results correlated well with experiments [65]. Thus, the application of SPH to cold spraying has been successfully implemented in optimizing process parameters. However, the issues of computational cost and tensile instability are still a strategic research direction.

4.2. Finite Element-Based Numerical Models for Cold Spray Processes

Six main computational models have been used to explain and simulate cold spray particle impacts. These models are used for high strain rate plasticity of various feedstock metallic powders and the overall deposition properties. The models include the Johnson–Cook (JC) plasticity model [85,86], Zerilli–Armstrong (ZA) model, Voyiadjis–Abed (VA) model, Preston–Tonk–Wallace (PTW) model [87], Khan–Huang–Liang (KHL) model, and the Gao–Zhang (GZ) model. The shortcomings of the models led to modified models where initial assumptions are improved to fit predicted data to the experiment ones. The common and widely used model is the JC model which is built into the ABAQUS/Explicit finite element analysis platform.

4.2.1. Johnson–Cook Model

This model was designed by Johnson and Cook and relates the flow stress to the strain rate, plastic strain, and temperature [38,86]. It is simple to use and successful in estimating flow stress more accurately for various engineering applications. The model has three parts focusing on strain hardening, strain rate hardening, and thermal softening as shown in Equation (2) [86]. The model is not suitable for predicting relatively high flow stresses at very high strain rate. In the case of Cu, the JC model fails when the strain rate exceeds 10^{-5} s^{-1} [86]. There is a linear relation between the work hardening and the strain rate on a logarithmic scale. This is indicative of the shortcoming of the JC model as it underestimates the material and mechanical behavior at very high strain rates.

$$\sigma = \left(A + B \epsilon_p^n \right) \left[1 + C \ln \dot{\epsilon}_p^* \right] \left[1 - (T^*)^m \right] \quad (2)$$

The homologous temperature in the JC model, which is T^* , is given and defined in Equation (3), where the absolute, transition or reference, and melting temperatures are T , T_r , and T_m , respectively.

$$T^* = \begin{cases} 0, & T < T_r \\ \frac{T - T_r}{T_m - T_r}, & T_r < T < T_m \\ 1, & T > T_m \end{cases} \quad (3)$$

where: the parameters A , B , n , C , and m are material-dependent constants, ϵ_p is an equivalent plastic strain, $\dot{\epsilon}_p^*$ is an equivalent plastic strain (ratio of the plastic strain rate and reference strain rate).

The JC model is the most successful constitutive model for simulating cold spray behavior of various metallic alloys [38,48,85,86,88–92]. Typical applications of the JC model for Cu, Ni, and 316 steels with the respective JC parameters are given in Table 4. Similar studies have been carried out using refractory Ta powders on 4340 steel substrates [93] and

the effect of nanoscale interfacial oxides on the deformation and cracking phenomena on cold spray Al 6061 powders [94]. These studies used experimental and computational approaches. An overview of some of the ferrous and non-ferrous cold spray coating phenomena, deformation mechanisms, material jetting, and the effects of various microstructural features has been presented [3,95–97].

Table 4. Typical JC model and general parameters used for numerical simulation of cold spray for Cu, Ni, and 316SS extracted from published literature [48,86,95–97].

Parameters	Material		
	Cu	Ni	316
Johnson–Cook parameters			
A (MPa)	90	163	388
B (MPa)	292	648	1728
C	0.025	0.006	0.02494
m	1.09	1.44	0.6567
n	0.31	0.33	0.8722
Strain (1/s)	1	1	0.00001
Thermal and general properties			
Density (g/cm ³)	8.96	8.90	8.03
Conductivity (W/Km ²)	386	90.6	16
Specific heat (J/kgK)	383	435–446	457
Melting point (K)	1356	~1728	1643
Poisson ratio	0.34	0.31	0.3
Elastic modulus (GPa)	124	200	193

To make up for the lapses in the original JC model, a modified JC model is proposed for relatively high strain rates [96–101]. This is given in Equations (4) and (5) [102,103]. The JC and modified JC models have fewer material constants compared to the typical Preston–Tonk–Wallace (PTW) model. These JC models are extensively used for various materials with their constants are easily accessible in the literature [102–105].

$$\sigma = \left(A + B\dot{\epsilon}_p^n \right) \left[1 + C \ln \frac{\dot{\epsilon}_p}{\dot{\epsilon}_0} \left(\frac{\dot{\epsilon}_p}{\dot{\epsilon}_c} \right)^D \right] \left[1 - \left(\frac{T - T_r}{T_m - T_r} \right)^m \right] \quad (4)$$

$$D = \begin{cases} x, \dot{\epsilon}_p \geq \dot{\epsilon}_c \\ 0, \dot{\epsilon}_p \leq \dot{\epsilon}_c \\ \dot{\epsilon}_c = y s^{-1} \end{cases} \quad (5)$$

where: D is a non-zero (x) parameter when $\dot{\epsilon}_p$ (plastic strain rate) is within a certain critical strain rate ($\dot{\epsilon}_c$) value and $\dot{\epsilon}_0$ is the reference strain rate.

A typical bilinear JC model, which is an improvement on the previous JC models with the capacity for two-stage rate sensitivity, has been used for many systems [94,106,107]. The bilinear model incorporates a second constant to improve the approximation of high strain rate sensitivity [107]. A typical bilinear JC model has been implemented in ABAQUS–Explicit for the study of interfacial oxide effects on cold spray of Al [94].

4.2.2. Preston–Tonk–Wallace (PTW) Model

The PTW model was designed for estimating the material behavior of relatively high strain rates as shown in Equations (6) and (7) [87]. This is to correct the challenges associated with the JC model which breaks down at strain rates above 10⁴/s [17,108].

This is a constitutive parametric model designed based on the dislocation movement and mechanisms during plastic deformation [108]. Typical PTW models have been used for wide strain rate ranges (10^{-3} – 10^{13} /s) [17,108].

$$\sigma = 2 \left[\tau_s + \alpha \ln \left[1 - \varphi \exp \left(-\beta - \frac{\theta \epsilon_p}{\alpha \varphi} \right) \right] \right] \mu(p, T) \tag{6}$$

$$\alpha = \frac{S_0 - \tau_y}{d}, \beta = \frac{\tau_s - \tau_y}{\alpha}, \varphi = \exp(\beta) - 1 \tag{7}$$

where: τ_s = normalized work hardening saturation stress, s_0 = saturation stress at 0 K, τ_y = normalized yield stress, θ = strain hardening rate, ϵ = equivalent plastic strain, d = dimensionless material constant. The “ μ ” is the shear modulus, which is a function of the temperature and easily estimated using the mechanical threshold stress (MTS) shear modulus model given in Equation (8) [109]. The τ_s and τ_y are given in Table 5.

$$\mu(T) = \mu_0 - \frac{D}{\exp\left(\frac{T_0}{T}\right) - 1} \tag{8}$$

where: μ_0 = shear modulus at 0 K, D and T_0 = material constants, and T = temperature of the material [109]. The standard parameters for the PTW model are the strain rate dependence constant, strain hardening rate, strain hardening constant, yield stress constant at 0 K, yield stress constant at melting, medium strain rate constant, high strain rate constant, high strain rate exponent, saturation stress at 0 K, saturation strength at melting, temperature dependence constant, atomic mass, shear modulus, material constant (D), and temperature material constant [110].

Table 5. Parameters for normalized work hardening and normalized yield stress.

Parameters	Expression
Normalized work hardening saturation stress	$\tau_s = \max \left\{ S_0 - (S_0 - S_\infty) \operatorname{erf} \left[k \hat{T} \ln \left(\frac{\gamma \zeta}{\epsilon_p} \right) \right], S_0 \left(\frac{\epsilon_p}{\gamma \zeta} \right) \right\}$
Normalized yield stress	$\tau_y = \max \left\{ y_0 - (y_0 - y_\infty) \operatorname{erf} \left[k \hat{T} \ln \left(\frac{\gamma \zeta}{\epsilon_p} \right) \right], \min \left\{ y_1 \left(\frac{\epsilon_p}{\gamma \zeta} \right), S_0 \left(\frac{\epsilon_p}{\gamma \zeta} \right) \right\} \right\}$
Where $\zeta = \frac{1}{2} \left(\sqrt[3]{\left(\frac{4\pi\rho}{3M} \right)} \right) \left(\sqrt{\frac{\mu(\rho,T)}{\rho}} \right)$	

The PTW model is more complicated than the typical Johnson–Cook model, but there is more control of the material parameters. Recent investigations on dilute or conventional metallic materials such Cu and WC-Co and cold spray coating applications have been reported [104,108,111]. Plastic deformation during cold spray processes has been modeled using the PTW model for strain rates up to 10^7 /s with comparable results to experiments [87,109]. The PTW has also been applied within the ALE framework due to the good fit at very high strain rates [102].

4.2.3. The Zerilli–Armstrong (ZA) Model

The ZA model is for estimating plastic deformation behavior of materials, focusing on flow stress at relatively high temperatures [103,105,112]. The flow stress is given by the relation shown in Equation (9). The ZA model is a physical model and applies to a range of materials with varying crystal structures sensitive to temperature and strain rate. The exponential term in Equation (9) describes the thermal stress component which is derived experimentally. As the temperature tends to infinity, the thermal stress components become zero.

$$\sigma = (C_1 + C_2 \epsilon^n) \exp \left\{ - \left((C_3 + C_4 T^*) T^* + (C_5 + C_6 T^*) \ln \dot{\epsilon}^* \right) \right\} \tag{9}$$

where: $T^* = T - T_r$, $C_1, C_2, C_3, C_4, C_5, C_6$, and n = material constants, ε = equivalent plastic strain, $\dot{\varepsilon}^*$ = normalized equivalent plastic strain, T = absolute temperature, and T_r = reference temperature.

The modification of the ZA model is carried out to improve the temperature-dependent terms of the original model. The modified ZA model gives better results for temperatures above 300 K, and the work hardening is independent of strain rate and temperature, which is an assumption that drives the original model. The flow stress based on the modified ZA model is given in Equation (10).

$$\sigma = B\varepsilon_p^{0.5} \left(1 - \sqrt{x} - x + \sqrt{x^3} \right) + C_6 \quad (10)$$

4.2.4. The Voyiadjis–Abed (VA) Model

The Voyiadjis–Abed model was designed as an improvement on the ZA model [113]. The prediction is more efficient for higher strain rates and higher temperatures than the ZA model. The model is summarized in Equation (11).

$$\sigma = B\varepsilon_p^n \left(1 - (\beta_1 T - \beta_2 T \ln \dot{\varepsilon}_p)^{1/q} \right)^{1/p} + Y_a \quad (11)$$

where: ε_p = equivalent plastic strain, $\dot{\varepsilon}_p$ = plastic strain rate, T = temperature, and $B, Y_a, \beta_1, \beta_2, p, q$, and n = material constants.

4.2.5. The Other Types of Models

There are other types of models that have been used for estimating the mechanisms of cold spray methods [89]. These include the modified Zerilli–Armstrong [113,114], modified Khan–Huang–Liang (MKHL) [115,116], and the Gao–Zhang models [117]. The details of these models are summarized elsewhere [89].

The current state of the art, looking at numerical and experimental approaches for the design of cold spray coatings are discussed. Emphasis is on concentrated amorphous and crystalline coatings. The amorphous alloy coatings are mainly bulk metallic glasses (BMGs), whereas the crystalline materials are complex concentrated alloys (CCAs).

5. Bulk Metallic Glass Cold Spray Coatings

Bulk metallic glasses (BMGs) have gained traction since the 1990s [118–120]. These are mainly amorphous or partially crystallized materials with medium- to long-range disorder devoid of typical lattice defects such as dislocations and grain boundaries [120–126]. They undergo strain softening, localized shear instability, and easily rupture under applied loads. Most BMGs possess high elastic modulus and high strength [120]. There is a trade-off between strength and ductility, resulting in poor plasticity. Challenges associated with BMGs as structural materials include: (i) size limitation due to limited glass-forming abilities (GFAs) and very high cooling rates ($>10^5$ K/s) [123]. These alloys can be produced to about few centimeter sizes and are mainly wires, ribbons, and powders, restricting large scale and industrial applications [120–122]; and (ii) poor ambient temperature plasticity and deformation is constrained to concentrated shear zones [125,126]. Thus, they are not the right candidate for load-bearing structural applications [124,125].

Some of the main BMG coating systems include Al, Cu, Fe, Ni, and Zr. Characteristic features and suggested applications of these coatings are given in Table 6. Advantages of BMG cold spray coatings over traditional BMG coatings are:

- High hardness, high strength, and wear resistance: BMG coatings exhibit high hardness and wear resistance, making them suitable for use in harsh environments where traditional coatings may fail.
- Corrosion resistance: BMG coatings have excellent corrosion resistance, making them perfect for use in marine, aerospace, and other corrosive environments.

- Low porosity: BMG coatings have a low porosity, lowering the chance of corrosion and enhancing substrate adhesion.
- High bonding strength: BMG coatings have a strong bond to their substrate, reducing the chance of delamination or cracking.
- Low thermal conductivity: BMG coatings have a low thermal conductivity, making them suitable for use in high-temperature environments where thermal insulation is needed.
- Tailored properties: BMG coatings possess specific properties such as electrical conductivity, magnetic properties, or optical properties, making them useful in a variety of applications.
- Cost effectiveness: As a cost-effective substitute for conventional coating techniques, BMG cold spray coatings can be applied using a relatively inexpensive procedure.

Table 6. Thermal spray coating of various types of metallic glasses.

System	Features	Suggested Applications	Ref
Al based	Very dense structure Excellent corrosion resistance Great strength-to-weight ratio	Automobile and aircraft Sacrificial anode Environmental protection	[127–129]
Cu based	Great mechanical properties Excellent nanosize properties	Microelectromechanical systems Turbine applications	[130]
Fe based	Improved strength Improved wear resistance Excellent corrosion resistance Strong glass formability Low-cost material	Marine and coastal areas Power plants Hydraulic machinery	[131–135]
Ni based	Very high strength High thermal stability Expensive process cost Excellent corrosion resistance	Petrochemical applications Glass industries Nuclear applications	[136,137]
Zr based	Excellent fracture toughness Excellent ductility Excellent corrosion resistance High hardness	Biomedical applications Nuclear applications Bearings	[138,139]

Overall, the distinctive combination of qualities provided by BMG cold spray coatings makes them a desirable option for a variety of applications, including those in the aerospace, automotive, energy, and biomedical industries.

Bulk metallic cold spray coatings are desirable due to the low temperature and solid-state deposition mechanism [54,140–143]. These contribute to effective reduction in porosity and retard recrystallization during cyclic thermal stresses. The low temperature leads to restraining of distortions which could arise from thermal stresses and oxidation phenomena. The process does induce compressive residual stresses in BMG cold spray coatings, while improving metallurgical bonding at the coating–substrate interface and between the various layers of the coatings [140–143]. These alloys have been investigated using numerical and experimental approaches, showing excellent functional and structural properties. The BMG coatings produced from cold spray with processing parameters are given in Table 7.

Table 7. Bulk metallic glass cold spray coatings on various substrates with processing parameters.

BMG Coating	Substrate	Gas	Temperature (°C)	Pressure (MPa)	Ref.
Al ₈₈ Ni ₆ Y _{4.5} Co ₁ La _{0.5}	Al 7075	N ₂	300–400	3.0–4.0	[144]
Al _{90.05} Ni _{4.3} Y _{4.4} Co _{0.9} Sc _{0.35}	Al 6061		3.8	[145]	
Cu ₅₀ Zr ₅₀	Stainless steel		500–800	~4.0	[146]
Cu ₅₄ Ni ₆ Ti ₁₈ Zr ₂₂	Cu		~550	1.5–3	[147]
FeCrMoWCMnSiZrB	Al 6061	He	~300	1	[148]
Fe _{68.8} C ₇ Si _{3.5} B ₅ P _{9.6} Cr _{2.1} Mo ₂ Al ₂	Mild steel		~550	2.1–2.9	[149]
Fe ₄₄ Co ₆ Cr ₁₅ Mo ₁₄ C ₁₅ B ₆	Al/Cu/Ti	N ₂	900–950	~4.0	[150]
Fe ₇₃ Cr ₂ Si ₁₁ B ₁₁ C ₃	Carbon steel		900–1000	4–5	[142]
Ni ₅₇ Ti ₁₉ Zr ₂₀ Si ₃ Sn ₂	Mild steel	He	~600	~3	[151,152]
ZrCuAlNiTi	Cu		~500	2.4	[153]

5.1. Aluminum-Based BMG Cold Spray Coatings

Aluminum bulk metallic glass alloys have low density, high specific strength (1000–1500 MPa) [154,155], great corrosion resistance, and high modulus. They are difficult to deform due to the disordered arrangement of atoms with the low critical resolved shear stresses of Al [120]. A few Al-based BMG coatings have been designed and studied [120,144,145] and their compositions are based on the ternary system (Al–TM–RE), where TM stands for transition metal (Ni, Co, or Fe) and RE stands for rare earth (La, Ce, Gd, or Y) [103]. The transition metals are used to accelerate the atomic packing process, whereas the rare earth elements induce glass formation [103,129,145,156–158]. Some of the main cold spray coating systems are Al–Co–Ce [129,156], Al–Ni–Ce [103], Al–Y–Ni–Co–Sc [145], and Al–Ni–Y–Co–La [144].

The wear and mechanical behavior of Al-based BMG cold spray coatings on Al substrate has been studied. The coating had high hardness due to the glass-forming properties and superior wear resistance was observed compared to the substrate. For corrosion resistance, the coatings were over five times better than the substrate when tested in NaCl solution. The coating has two main factors contributing to the high corrosion resistance. Due to the amorphous nature of the coatings and the chemical homogeneity, it prevents the onset of the formation of galvanic cells [154]. Furthermore, the corrosion resistance improves due to the presence of nanocrystals which accelerate the formation of protective passive films resulting from rapid diffusion of passive element to the interface between the substrate and coatings as well as the surface. This has also been confirmed experimentally [155,157,158]. These nanocrystals were confirmed with high-resolution transmission electron microscopy. Similar results were obtained for AlNiYCoLa on Al 7075 substrate [144]. The combined effect of the amorphous phase and the Al₂O₃ passive oxide layer was the contributing factor to the superior corrosion resistance.

Wear behavior is dependent on the volume fraction of the amorphous phase of the Al-based BMG coatings. The amorphous phase proportion, thickness, strength, porosity, and hardness are dependent on the processing parameters (stand-off distance, gas pressure, and temperature). Excellent wear resistance was observed for Al-based coating with ~81% amorphous phase. The coefficient of friction was also reduced by more than 30%. The wear mechanism of the coating was abrasive grooving with minute surface splat delamination.

5.2. Copper-Based BMG Cold Spray Coatings

Copper-based BMG alloys have structural and functional properties for various engineering applications [159–162]. These properties include corrosion resistance and high strength and hardness which are applicable in biomedical, aerospace, electronics, and sport equipment. The binary systems which are the base for Cu-based BMG are Cu–Ti, Cu–Ni, and Cu–Zr [159–162]. For the 54Cu–22Zr–18Ti–6Ni BMG coating on Al 6061 substrate, a

porosity below 5% was observed with coating thickness ranging from 300–400 μm [161]. The hardness of the coating was 412.8 HV, whereas the wear resistance was three times better than that of the pure Cu coatings. The adhesion strength of the BMG coatings was better than that of the pure Cu coatings due to the synergistic effects of the alloy elements controlling the deformation mechanisms of the substrate. Poor corrosion resistance of the BMG coatings was observed, which is attributed to the high porosity in the amorphous coating layer [161].

Binary 50Cu–50Zr [146] and ternary Cu–Ti–Ni BMG cold spray coating systems have been studied for biomedical applications [163]. In the case of the equiatomic binary Cu–Zr coatings, the gas temperature was critical for the deposition efficiency. The main zones were no bonding, weak bonding, great bonding, and viscous flow. Due to the poor adhesion behavior associated with no bonding and weak bonding, there was no coating on the substrate. The deposition was carried out at 600 °C and 800 °C with the highest hardness and cohesive strength at 800 °C.

The BMG coatings of 50Cu–50– x (Ti)– x Ni were produced from low-energy ball milling (mechanical alloying) and cold spray [163]. The milling process reduced the particle sizes and offered some mixing, whereas the cold spray was used to deposit the coatings on austenite stainless steel substrate. The 50Cu–20Ti–30Ni and 51Cu–17Ti–13Ni coatings had the best wear resistance and relatively low coefficient of friction (0.32–0.45), with ~50% reduction in friction coefficient on 304 steel substrate (Figure 7) [163]. The coating sufficiently inhibited the formation of biofilm, thus being a promising coating for biomedical applications. This was mainly due to enhancement of antimicrobial effects of Ni by the relatively high amounts of Ti and Cu.

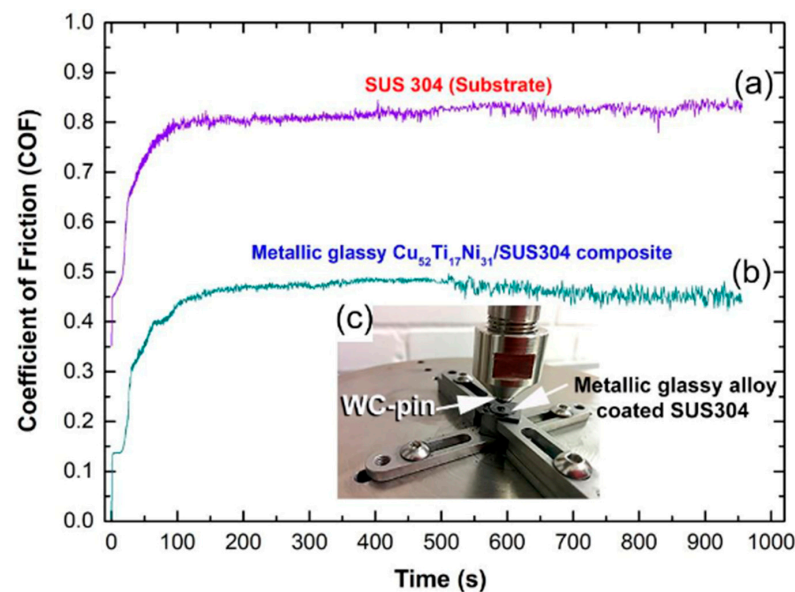


Figure 7. Comparison of the coefficient of friction of CuTiNi BMG cold spray coating with 304 steel substrate where (a) is the untreated 304 substrate, (b) the 304 substrate with Cu-based metallic glass coatings and (c) the experimental set-up for the wear testing [163].

Numerical and experimental approaches have been used to study the nanocrystallization of CuNiTiZr BMG coatings [147]. The numerical and experimental results showed that the kinetic energy of the impacting particles has a significant impact on the activation energy for nucleation and the fraction of crystallinity in BMG coatings [147]. The high-velocity impact resulted in a reduction in the free energy barrier and an increase in the driving force for the phase transition from amorphous to crystalline due to the kinetic energy of the particles. When the CuNiTiZr BMG was subjected to the cold spray technique, the microstructural characterization showed that the nanocrystallization of the substance was related to the strain energy produced by rapid plastic deformation.

5.3. Iron-Based BMG Cold Spray Coatings

These alloys have unique structural properties such as wear resistance and great strength behavior [120,134,164] and functional properties such as superior glass-forming ability, corrosion resistance [165–167], and soft magnetic properties. Initial works include production of cold spray coatings of Fe-Cr-W-Mo-Mn-C-Si-B-Zr on Al substrate showing ultralow porosity along the nominal microcracks [148,165]. Microhardness of the BMG cold spray coating is ~ 639 HV_{0.3}, which is about ten times higher than that of the Al substrate [148]. The degree of amorphization was poor as most of the particles were not fully amorphous. The drawback of the coating on the substrate is the small thickness of ~ 0.2 mm, which is not durable for long-term and aggressive corrosion or oxidation environments. The bonding mechanism is attributed to adiabatic shear instability which leads to metallurgical bonding at the BMG particles and Al substrate [143,148]. Localized deformation was observed at the particle–particle boundary and softening resulted from adiabatic deformation within the feedstock particles during the formation of the splat [88,168–170]. For typical BMG coatings, the deposition efficiency (DE) is one of the main parameters that ensure structural integrity and the quality of the coating [141,150,166,171]. The DE is also influenced by processing parameters such as gas temperature, stand-off distance, substrate temperature, and process gas pressure (Table 2) [150,166,171].

The tribological behavior of BMG coatings produced from cold spray on various metallic substrates has been studied [120,143,149]. For FeCSiBPCrAlMo coatings, a lower coefficient of friction was observed compared to bearing steel [149]. Similarly, the wear behavior of cold spray coatings of FeCrMoCBY is better than that of BMG coatings produced using other thermal spray methods [143]. The superior tribological behavior of cold spray coatings of BMG compared to high-velocity air fuel (HVOF) was due to excellent adhesion at the particle–particle and particle–substrate interface [18,172,173] and lack of oxidation due to the low heat input. The CS coating also had $\sim 2\%$ porosity and high hardness due to grain refinement resulting from the peening effect associated with cold spray [173–175].

5.4. Nickel-Based BMG Cold Spray Coatings

Typical Ni-based BMG coatings have high strength, high thermal stability, and great corrosion resistance [120,176,177]. The Ni-based BMG systems are from the ternary compositions of Ni–Ti–Zr, Ni–Zr–Al, and Ni–Nb–Ti with slight modification of the microstructure with minute addition of metalloids (Si or B) [120,176,177]. Some of the major compositions which have been studied extensively include 57Ni–18Ti–20Zr–3Si–2Sn [176–178], 59Ni–20Zr–16Ti–2Si–3Sn [151,178], and 53Ni–20Nb–10Ti–8Zr–6Co–3Cu [177], where the compositions are according to weight percent.

The main properties of interest for Ni-based BMG cold spray coatings on different substrates are wear and corrosion resistance [120,145,151,152,179,180]. Cold spray coatings showed better wear and corrosion resistance than other thermal spray techniques such as vacuum plasma and high-velocity oxy-fuel spraying. This is mainly due to negligible phase transformation of the BMG produced by cold spray [151]. The propelling gas plays a critical role in the deposition efficiency of the BMG on mild steel [103]. By switching from nitrogen to helium, there was significant improvement in deposition efficiency [151,152]. The high drag force of helium and the high heating rate of feedstock led to increased splat to crater ratio, enhancing mechanical properties and bond strength [120]. This has been observed in NiTiZrSiSn BMG coating [145,151,152,179,180].

5.5. Zirconium-Based BMG Cold Spray Coatings

Zirconium-based bulk metallic glass (BMG) cold coatings are protective coatings applied to a variety of substrates [118,120,121,123,181]. These amorphous metallic coatings have a unique combination of properties, including high strength, high corrosion resistance, excellent wear resistance, and excellent biocompatibility for biomedical applications [103,120,153,182,183]. These amorphous alloys have a wide supercooled region with excellent glass-forming abilities. The common compositions are based on the quaternary

and quinary systems of Zr–Cu–Al–Ni and Zr–Cu–Al–Ni–Ti [118,120,181]. There have been some additions of Be and Fe for excellent mechanical properties, corrosion and wear resistance [120,181].

The mechanical properties such as hardness and strength are functions of operating temperature and the volume fraction of the amorphous phase. For a typical ZrCuAl–NiTi/Cu metallic glass coating, the hardness increased from 500 HV at 400 °C to 620 HV with a 50°C increase in temperature.

6. Complex Concentrated Alloys—Brief Overview

Complex concentrated alloys are a broad class of structural and functional materials which are defined by their design strategy [5,184]. These encompass the medium-entropy alloys, high-entropy alloys (HEAs), and multiple principal element-based alloys (Figure 8). These alloys, by composition, occupy the central region of a typical phase or composition diagram as shown in Figure 9. The high-entropy alloys have multiple principal alloying elements with at least five components. They are in near-equiatomic ratios ranging from 5–35 at% [184]. The design philosophy of HEAs is premised on the assumption that forming solid solutions by constituent elements leads to high configurational entropy or entropy of mixing.

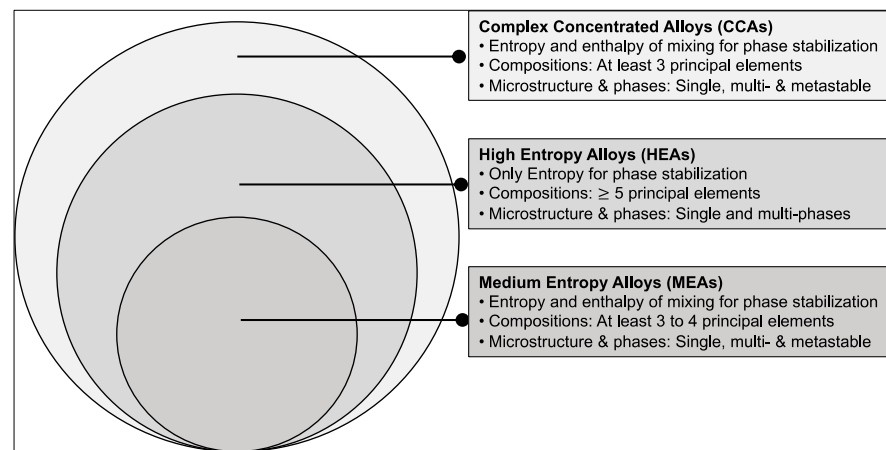


Figure 8. Complex concentrated alloys and their derivatives.

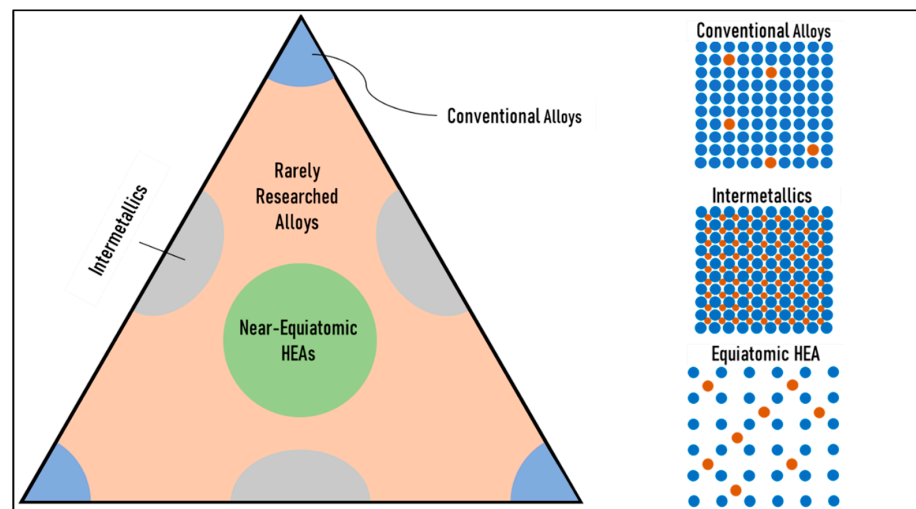


Figure 9. Typical illustration of dilute (compositions at the corners) and complex concentrated (compositions at and near the center) alloys.

These alloys extend the frontiers for alloy design beyond the conventional dilute alloying concentrations with potentially different properties for structural and functional applications [1–3,20,185]. The excellent structural and functional properties are attributed to four core effects.

6.1. Core Effects of Complex Concentrated Alloys

There are four main core effects associated with CCAs/HEAs, which are high configurational entropy of stabilization, sluggish diffusion, severe lattice distortions, and cocktail effects. The core effects and the relationship between the science and the physical metallurgy of CCAs are schematically shown in Figure 10. The entropy effect focuses on the thermodynamics; sluggish diffusion drives the kinetic phenomenon; severe lattice distortions focus on deformation theory, solid-state physics, and the strengthening mechanisms. The cocktail effects relate to how the structural and functional properties are impacted. The three core effects of high configurational entropy of stabilization, sluggish diffusions, and severe lattice distortions have been a bone of contention and require further investigation. They are not overarching and there is limited evidence that the “core effects” play significant roles in determining the unusual properties of CCAs. A brief description of the core effects is summarized.

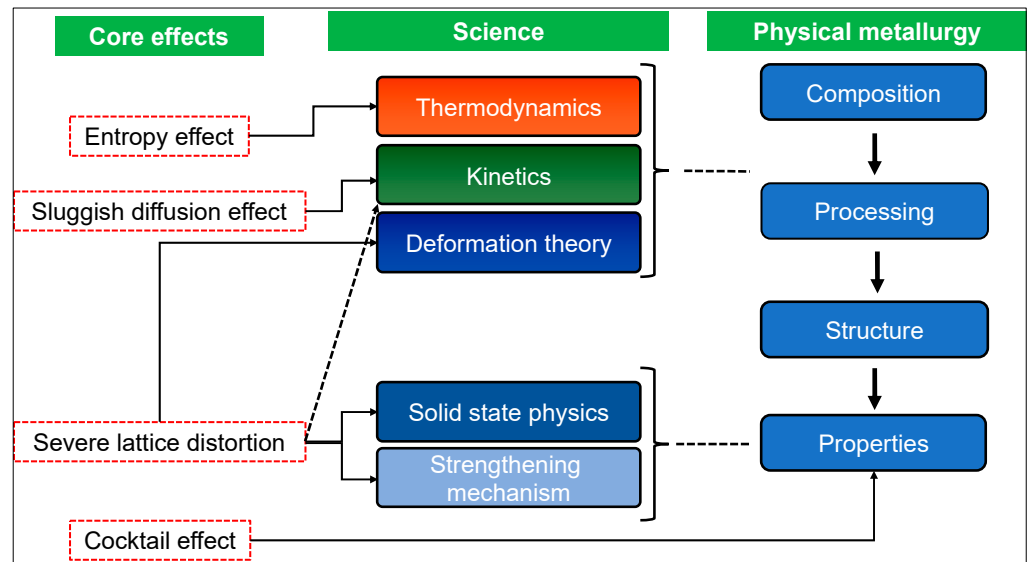


Figure 10. The interrelationship between core effects, the science, and physical metallurgy of CCAs.

High configurational entropy and enthalpy of mixing: The high entropy and enthalpy of mixing effects deviate from the Gibbs phase rule stabilizing phase proportions. This contributes to the observed properties, which are not common to most conventional one- or two-principal element-based materials. Increasing the constituent elements lowers the Gibbs free energy of the system, which outweighs the driving force for detrimental intermetallic phases and restricts their formation. Thus, most CCAs/HEAs should have simple and stabilized solid-solution phases. Configurational entropy and the enthalpy of mixing are related by Boltzmann’s relation (Equation (12)).

$$\Delta S_{\text{conf}} = k \ln w \quad (12)$$

where: k = Boltzmann’s constant, w = possible ways of mixing available energy.

Initial families of CCAs/HEAs supported the assumption of high configurational entropy of mixing. Recent families of HEAs deviate from the possibility of forming stabilized solid solutions across the full range of temperatures. For example, the Cantor alloy (CrCoFeMnNi) is observed to be stable as a face centered cubic solid solution at high temperatures. However, precipitates of tetragonal sigma phases can be observed at inter-

mediate temperatures. A few five-component CCAs are stable to intermetallic formation, hence the high configurational entropy stabilized is not an overarching effect and not quite strong enough for the observed properties in typical CCAs/HEAs. Common additions leading to the decomposition of the solid-solution phases are Ti, V, Cr, Cu, Al, and Mo due to their size difference and entropy. The concept of Hume-Rothery rules still applies to the dominance of enthalpy of formation. Thus, more investigation is required to establish the underlying factors and physical metallurgy principles.

Sluggish diffusion: Based on the atomic environment, there is slow diffusion due to variation in the potential energy of the lattices. This results in low kinetic transformation leading to sluggish diffusion effects. Slow diffusion of the mixing atoms results in variation of lattice potential energy due to differences in the atomic environment. Due to many constituent elements, some of the atoms are easily trapped, contributing to the sluggish diffusion phenomenon. This increases recrystallization temperature, reduces particle coarsening rate, and then leads to nanocrystalline structure.

Severe lattice distortion: This phenomenon is attributed to differences in size, bond energy, and crystal structures, resulting in mismatch [186–189]. It promotes the overall reaction rate [186,188]. Thus, localized and severely distorted lattices are observed but do not have the same effects of broadening X-ray diffraction peaks as in the case of dislocation defects [186,188]. The severe lattice distortions result in more incoherent scattering with reduced intensity of the XRD peaks [190,191]. The best way to measure the severe lattice distortions and quantify them is by a pair distribution function from the total scattering data, an extension of XRD, and neutron diffraction measurements [190–192]. In Figure 11, the weighted average distance to the nearest neighbors (interatomic distance) is shown and the width of the peaks estimates how much distortion occurs within the structure. Neutron diffraction has been used to estimate the lattice distortions in the Cantor alloy which is given in Figure 12 [186,188,189,193].

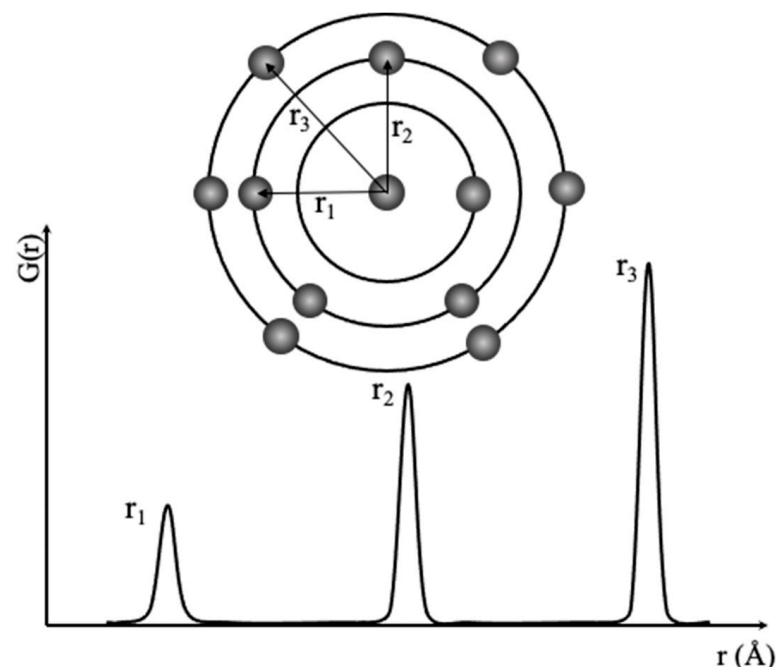


Figure 11. Schematics showing pair-wise distribution function for estimating the severe lattice distortions in CCAs.

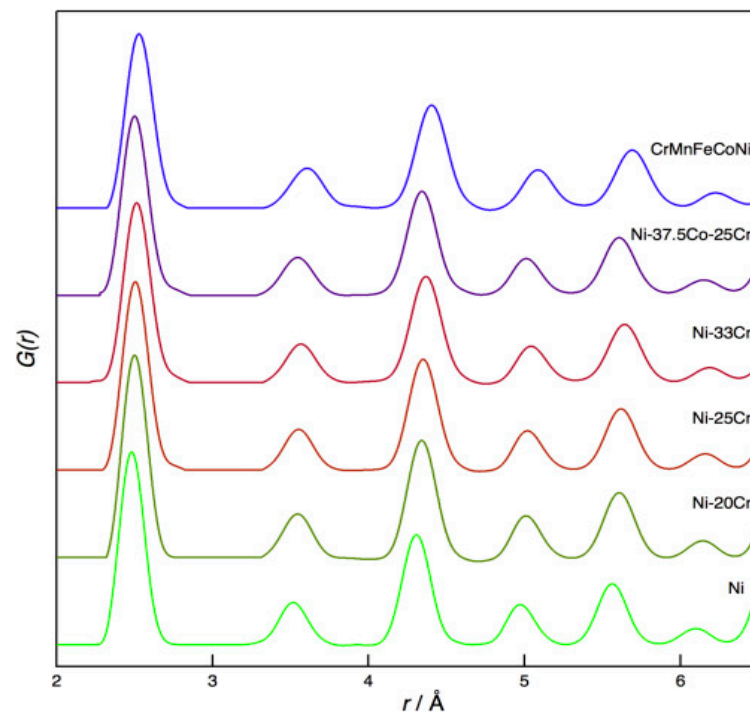


Figure 12. Normalized pair distribution function 3 for typical Ni-based alloys compared with the CrMnFeCoNi alloy based on the first six coordination shells [189].

Based on the pair distribution function, any severe distortions are easily quantified. Each peak in Figure 12 corresponds to a coordination shell around the atom at radius r and the area depends on the interaction of the atomic species and the respective coordination number [189]. In the case of severely distorted lattices, there is an increment in the width of individual peaks due to the noticeable displacement of the atoms from the original lattices or ideal positions. Once these displacements are significant within the coordination numbers with low “ r ” shells, the cumulative effect at a larger “ r ” causes more broadening of the peaks, resulting in poorly discernible features as opposed to that which is observed for the alloys in Figure 12. In Figure 12, no significant differences are observed for most of the peaks for the alloys studied, thus well-defined lattices are observed with no severe lattice distortions.

Cocktail effect: This is the overall effect from composition–processing–microstructure of the alloy. This effect is different from traditional or conventional alloys. Although this effect is not clear, it violates the rule-of-mixtures considering solute and solvent atoms are not easily discernible. There are unusual physical, mechanical, and chemical properties of the resulting CCAs, which are better than the average constituent elements. This is mainly attributed to the interaction between constituent elements and the indirect impact of these elements.

6.2. Complex Concentrated Alloy Coatings

Bulk CCAs are expensive due to the high amounts of constituent elements. This is a factor that could hinder massive application and scalability of bulk CCAs for structural and functional applications [1,2,20]. This has necessitated the need for the design of CCA-based coatings to solve the overall cost problem [22]. The superior functional properties of CCAs/HEAs such as wear, irradiation, thermal stability, corrosion, and oxidation resistance are linked to the associated mechanisms and how they differ from different classes of non-conventional coatings. The various approaches to depositing CCAs on various substrates have been reviewed [22]. The fabrication processes are mainly plasma/laser deposition, vapor deposition, and thermal spraying as shown in Figure 13 [22]. These coatings induce surface properties required to improve mechanical, physical, and chemical properties of

engineering components. Reviews focusing on laser and vapor depositions of CCAs/HEA-based alloys are available elsewhere [10,28]. Most of the CCA-based coatings that have been explored using the various techniques on different metallic substrates are given in Table 8.

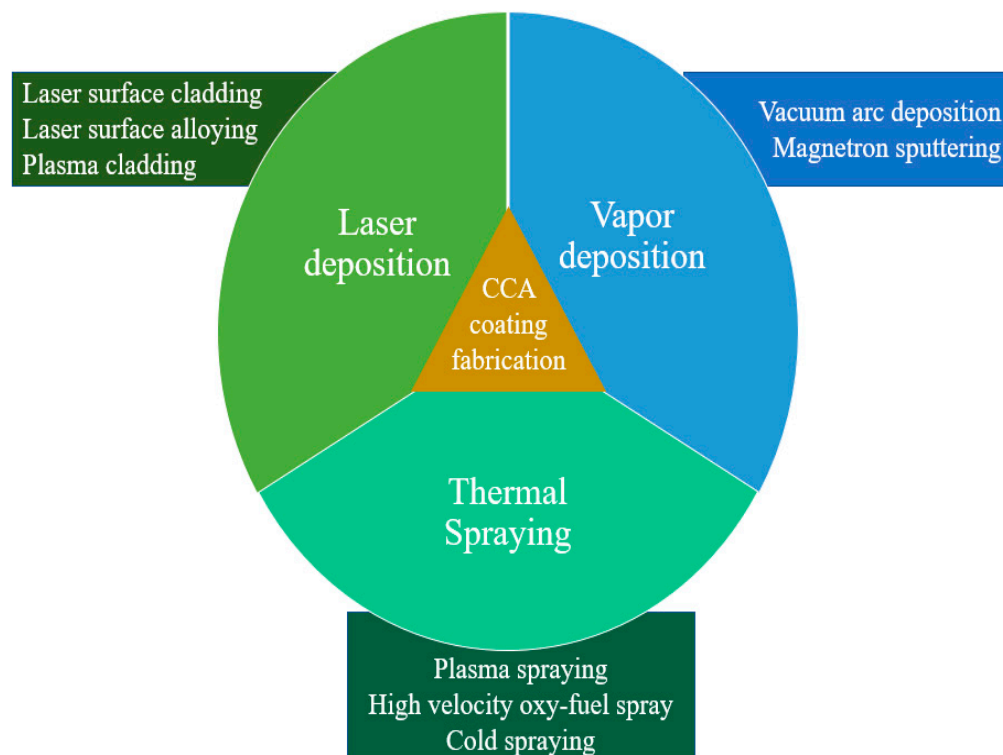


Figure 13. Typical fabrication methods of CCA/HEA coatings [194].

6.2.1. Complex Concentrated Alloy Cold Spray Coatings—An Outlook

Cold spray coatings have been used to deposit CCAs/HEAs on various substrate materials. These cold sprayed CCA/HEA-based coatings have shown excellent particle-to-substrate bonding, particle-to-particle bonding, adhesion strength, cohesive strength, relatively low porosity, and thickness of a few millimeters. These properties are essential in enhancing the physical, mechanical, and corrosion properties of these coatings in ways that induce structural integrity.

Trend analyses of publications with the keyword “cold spray + high entropy alloy” on Scopus and Web of Science were merged. A total of 37 peer-reviewed papers were found between 2019 and 2022, and their respective citations are shown in Figure 14. The first paper on cold spray of CrCoFeNiMn on an Al substrate was published in 2019. There is an increase in publications with an astronomical increase in citations since the pioneering works in March and June of 2019. In January 2023, two papers were published on the subject with 10 citations recorded based on the merged data from Scopus and Web of Science. The main papers are given in Table 9. The general theme is on the microstructural characterization of CCA-based cold spray coatings with a few focusing on the deposition of alloyed CCA-based powders on different metallic substrates. This has been successful as cold spray is a great way of depositing metals and intermetallics on various metallic substrates with ease.

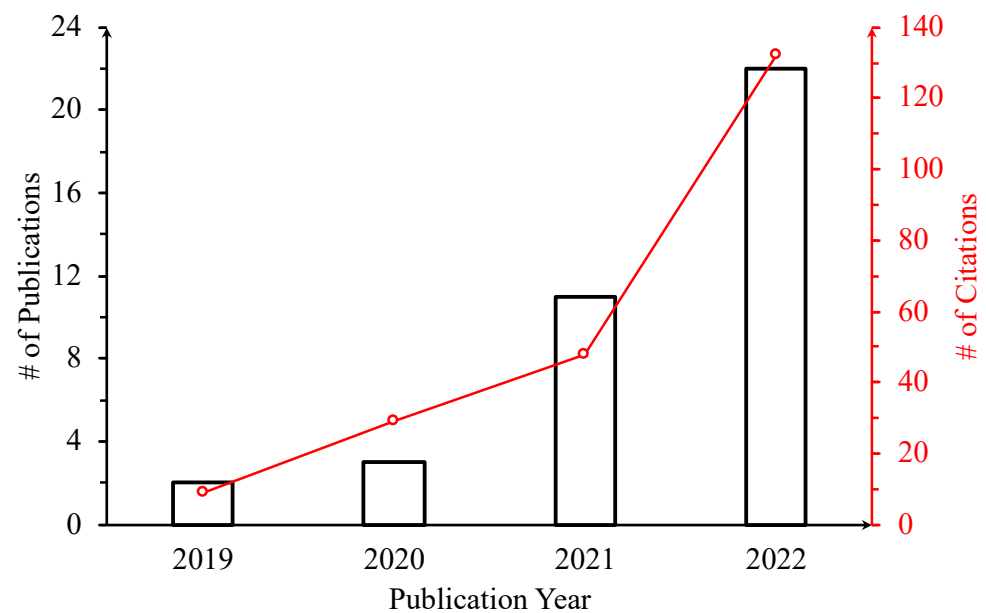


Figure 14. Yearly distribution of published journal articles indexed in Scopus and Web of Science with the corresponding citations from 2019 to 2022.

6.2.2. Mechanical Properties of Cold Sprayed CCAs on Different Metallic Substrates

Hardening mechanisms resulting from work hardening and grain refinements are associated with cold spray coatings in most conventional and complex concentrated alloys [9,27,55,56,88,89,195,196]. Deformation of the coating particles is due to high energy densities resulting in localized adiabatic shear [88,169,170]. The deformations are functions of particle distribution, morphology, size, and mechanical behavior of particles and processing parameters. The general behavior is also assisted by a peening effect of the coating particles, contributing to the enhanced mechanical properties. When the strain energy release rate is higher than the adhesive energy, propagating defects such as cracks interact with the interface layer, resulting in debonding of the coating. This ultimately leads to delamination, a process of the coating separating from the substrate, which is also due to poor wettability.

Strength and hardness properties: Strength and hardness of coatings are functions of composition of the substrate and coating material [27,105,112,197,198], the coating technique with optimized process parameters [91,199–201], quality, and microstructural features of the coating [28,202–206]. The bombardment of particle feedstock on the substrate induces severe plastic deformation [9,27,55,56,88,89,195,196]. This increases the strength and hardness of the cold sprayed coatings and the predominant strengthening mechanisms are mainly work hardening and grain refinement [88,168–170] as reported for CrMnFeCoNi [200] and CrFeNiMn [207] feedstock pre-alloyed through atomization. The porosity of the CrMnFeCoNi was observed to be ~0.47%, whereas that of CrFeNiMn was ~3.3%. The relatively low porosity in most CCA-based cold spray particles compared to other thermal spray processes shows the effect of the process on strengthening mechanisms.

Table 8. Different types of coating systems on different substrates and the resulting crystal structures and thickness.

Method	Substrate	CCA/HEA Coating	Structure	Thickness (μm)	References	
		Laser deposition techniques				
Plasma transferred arc cladding	Q 235	CoCrCuFeNiNb	FCC + Laves		[208]	
		TiC–TiB ₂ /CoCrCuFeNi	FCC + BCC + TiC + TiB ₂	~2000	[209]	
		CoNiCuFeCr	FCC		[210]	
Plasma cladding	AISI 1045 steel	CrCuFe _x NiTi	FCC + BCC + Fe ₂ Ti	~2500	[211]	
		FeCoNiAlCu		~1000	[212]	
		FeCoCrNiNbx	FCC + BCC	~1500	[213]	
	Pure Ti	CoCrFeNiNb	BCC + Cr ₂ Ti + Cr ₂ Nb	~500–600	[214]	
		AlTiVMoNb	BCC		[215]	
	Ti6Al4V	CoCrFeNi ₂ V _{0.5} Ti _{0.75}	BCC + (Co, Ni)Ti ₂ + Ti rich	~800	[216]	
	Laser cladding	Stainless steel	Al ₂ CrFeNiMox		-	[217]
6FeNiCoSiCrAlTi			BCC	1200	[218]	
Q 235 steel		MgMoNbFeTi ₂ Y _x		~1300	[219]	
		Al ₂ CrFeNiCoCuTi _x	FCC + BCC	~600	[220]	
		AlCoCrFeNi/NbC	FCC + BCC + NbC	1200	[221]	
		Al ₂ CoCrCuFeNiTi _x	-	500	[222]	
		FeCoNiCrCu(SiMnMo)	FCC	~2000	[223]	
		Al 5083	Al _{0.5} FeCu _{0.7} NiCoCr	FCC + BCC	~600	[224]
		H13 steel	Co ₃₄ Cr ₂₉ B ₁₄ Fe ₈ Ni ₈ Si ₇	Amorphous + FeNi ₃	~450	[225,226]
		45# steel	AlCoCrFeNi	FCC + FeAl ₃	-	[227]
AZ31 Mg	AlCoCrCuFeNiSi _{0.5} /Y ₂ O ₃	FCC + BCC	1500	[228]		
904L SS	CoCr ₂ FeNiTi _x /TiNi	FCC + TiN	1500	[229]		
M2 steel	MoFeCrTiWAlNb	BCC + (Nb, Ti)C + Fe ₂ Nb	1400	[230]		
253MA steel	Al _x CoCrFeNi	FCC + BCC	~900	[231]		
45 # steel	FeCrCoNiAlMo _x	BCC	~640	[232]		
H13 steel	FeCoCrBNiSi	Amorphous + FCC	~200	[233]		

Table 8. Cont.

Method	Substrate	CCA/HEA Coating	Structure	Thickness (μm)	References
Laser alloying	Ti6Al4V	CrCoNiTiVAl	BCC + (Ni, Co)Ti ₂		[234]
			BCC + (Ni, Co)Ti ₂ + HCP		[235]
	304 SS	FeCoCrAlNi		~600	[236]
	Q235	FeCoCrAlCu	BCC	800	[237]
	A36 steel	CrMnFeCoNi	FCC	2000	[238]
	Ni201	FeCoCrAlCuV _x Ni	FCC + BCC	400	[239]
	Pure Cu	FeCoCrAlCuNi _x		500	[240]
Vapor deposition techniques					
Vacuum arc deposition	Stainless steel	(TiZrNbAlYCr)N	FCC + BCC	~7	[241]
	C35 steel	(TiZrHfVNbTa)N	Amorphous + FCC + BCC	-	[242]
	C45 steel	(TiZrHfVNb)N	FCC	~4.78	[243]
Magnetron sputtering	304	FeCoCrNiMo _{0.1}	FCC	~0.85	[199]
		CrNbTiMoZr	Amorphous	~1.2	[244]
		CuMoTaWV	FCC + BCC	~0.9	[245]
	201	FeAlCuCrCoMn	FCC	~1.8	[246]
	M2 steel	CoCrNi/Ti	FCC + BCC + CoTi ₂	3.5	[247]
		(TiZrNbHfTa)C	FCC	2.0	[248]
	C45 steel	(TiZrNbHfTa)N	FCC	2.0	
	N36 Zr	AlCoMoNbZr	Amorphous + BCC	3.0	[249]
	Mild steel	(TiAlCrSiV) _x N _y	Amorphous + FCC	1.7	[250]
		(AlCrNbSiTiV)N		1.0	[251]
Si (100) wafer	(AlCrMnMoNiZr)N _x	FCC	1.5	[252]	
	(AlCrMoTaTi)Si _x N		1.0	[253]	
Si (100); SiO ₂ ; Al ₂ O ₃	(HfNbTiVr)N		1.2	[254]	
Ti6Al4V	TiTaHfNbZr	Amorphous	~0.8	[255]	
	Ag doped TiZrTaNbW		~1.1	[256]	

Table 8. Cont.

Method	Substrate	CCA/HEA Coating	Structure	Thickness (μm)	References
Thermal spray techniques					
High-velocity oxygen-fuel spraying	ASTM A572	Al _{0.6} TiCrFeCoNi		~300	[257]
	304/316	AlCoCrFeNiTi _{0.5}	BCC	~500	[258]
	304L	TiNbMoMnFe		-	[259]
	Incoloy 800H	Ni _{0.2} Co _{0.6} Fe _{0.2} CrSi _{0.2} AlTi _{0.2}	BCC + Cr ₃ Si	~1500	[260]
Plasma spray	316	AlCoCrFeNiTi/TiNi60	FCC + BCC		[261]
	Q235 steel	(CoCrFeNi) ₉₅ Nb ₅	FCC + Laves	500	[262]
	Mild steel	CoCrMnFeNi	FCC + BCC + Fe ₃ O ₄	-	[263]
		AlCoCrFeNi	FCC + BCC + Al ₂ (Cr, Fe)O ₄	-	
	304	FeCoNiCrMn	FCC	~195	[264]
		FeCoNiCrSiAl _x	BCC + FCC	~160	[265]
	Mild steel	AlCoCrFeNi	BCC + FCC		[266]
	Q 235	(CoCrFeNi) ₉₅ Nb ₅	BCC	~500	[262]
Atmospheric plasma spraying	304 SS	NiCo _{0.6} Fe _{0.2} Cr _{1.5} SiAlTi _{0.2}	FCC + BCC + Cr ₃ Si	-	[204]
		Ni _x Co _{0.6} Fe _{0.2} Cr _y Si ₂ AlTi _{0.2}	BCC + Cr ₃ Si	-	[267]
	316 SS	AlCoCrFeNiTi	BCC + FCC	240	[268]

Table 9. Summary of cold spray CCA-based coatings published from 2019 to 2023 from Web of Science and Scopus.

Database	Year	Title of the Published Paper	Refs
Web of Science	2019	Deposition of FeCoNiCrMn high entropy alloy (HEA) coating via cold spraying	[200]
		First report on cold-sprayed AlCoCrFeNi high-entropy alloy and its isothermal oxidation	[269]
	2020	Cold Gas Spraying of a High-Entropy CrFeNiMn Equiatomic Alloy	[207]
		Nanostructured AlNiCoFeCrTi high-entropy coating performed by cold spray	[270]

Table 9. Cont.

Database	Year	Title of the Published Paper	Refs
Web of Science	2021	Cold Spray Additive Manufacturing: Microstructure Evolution and Bonding Features	[271]
		Cold spray deposition characteristic and bonding of CrMnCoFeNi high entropy alloy	[272]
		Microstructure and properties of CuFeCrAlNiTi high entropy alloy coating prepared by cold spray assisted in-situ synthesis	
		Nanostructural AlNiCoFeCrTi High-Entropy Coatings Performed by Cold Spraying	[270]
		Solid-state cold spraying of FeCoCrNiMn high-entropy alloy: an insight into microstructure evolution and oxidation behavior at 700–900 °C	[273]
		Synthesis of High-Entropy AlNiCoFeCrTi Coating by Cold Spraying	[274]
		Tuning the Microstructure and Mechanical Properties of Cold Sprayed Equiatomic CoCrFeMnNi High-Entropy Alloy Coating Layer	[275]
	An inclusive numerical framework to assess the role of feedstock features on the quality of cold spray deposits	[276]	
	Cold Spray Additive Manufacturing of CoCrFeNiMn High-Entropy Alloy: Process Development, Microstructure, and Mechanical Properties	[206]	
	Cold Spray and Laser-Assisted Cold Spray of CrMnCoFeNi High Entropy Alloy Using Nitrogen as the Propelling Gas	[277]	
	Cold Spray: Over 30 Years of Development Toward a Hot Future	[9]	
	Deposition of High-Entropy Alloy Coating by Cold Spray Combined with Laser Melting: Feasibility Tests	[278]	
	Effect of Microstructure on Wear and Corrosion Performance of Thermally Sprayed AlCoCrFeMo High-Entropy Alloy Coatings	[202]	
	2022	Fatigue Bending of V-Notched Cold-Sprayed FeCoCrNiMn Coatings	[201]
Friction Stir Processing of Cold-Sprayed High-Entropy Alloy Particles Reinforced Aluminum Matrix Composites: Corrosion and Wear Properties	[279]		
Scopus		Mechanical and microstructural properties of a CoCrFe0.75NiMo0.3Nb0.125 high-entropy alloy additively manufactured via cold-spray	[169]
Web of Science		Microstructural, Mechanical and Wear Behavior of HVOF and Cold-Sprayed High-Entropy Alloys (HEAs) Coatings	[280]
		Microstructure and Mechanical Properties of the Plasma-Sprayed and Cold-Sprayed Al0.5CoCrFeNi2Ti0.5 High-Entropy Alloy Coatings	[197]
		Microstructure and Properties of Cold Spraying AlCoCrCuFeNi _x HEA Coatings Synthesized by Induction Remelting	[281]

Table 9. Cont.

Database	Year	Title of the Published Paper	Refs
Web of Science		Microstructure and tribological properties of Al ₂ O ₃ reinforced FeCoNiCrMn high entropy alloy composite coatings by cold spray	[282]
Scopus		Microstructure evolution and composition redistribution of FeCoNiCrMn high entropy alloy under extreme plastic deformation	[283]
Web of Science	2022	Microstructures, wear resistance and corrosion resistance of CoCrFeNi high entropy alloys coating on AZ91 Mg alloy prepared by cold spray	[284]
Scopus		Modification of cold-sprayed high-entropy alloy particles reinforced aluminum matrix composites via friction stir processing	[170]
Scopus		Numerical and Experimental Analysis of the Deformation Behavior of CoCrFeNiMn High Entropy Alloy Particles onto Various Substrates During Cold Spraying	[285]
Web of Science		Numerical Simulation of Cold Spray Bonding for CrFeNi Medium-Entropy Alloy	[286]
Web of Science		Structure Evolution and Corrosion Performance of CoCrFeMnNi High Entropy Alloy Coatings Produced Via Plasma Spray and Cold Spray	[287]
Scopus	2023	Cyclic behavior of FeCoCrNiMn high entropy alloy coatings produced through cold spray	[18]
Scopus		Sliding wear behavior of high entropy alloy coatings deposited through cold spraying and flame spraying: A comparative assessment	[288]

The core effects of CCAs, such as high configuration entropy of stabilization and enthalpy of mixing, sluggish diffusion, severe lattice distortion, and the cocktail effect due to interaction between atoms, could be contributing effects to the overall behavior of CCA-based coatings. The comparison of hardness of CCA-based coatings based on various thermal spray approaches is given in Figure 15 [28]. There are discernible trends for the approaches with the HVOF and APS having the highest hardness trends. Factors contributing the high hardness can be attributed to the approach used in producing the feedstock. For most of the HVOF and APS approaches, the feedstock was produced using mechanical alloying and high-pressure mechanical blending coupled with tubular mixing. This resulted in reducing the overall grain sizes to $\sim 10\text{--}40\ \mu\text{m}$. The strengthening mechanisms for these processes were a combination of solid solution strengthening, interstitial strengthening, precipitation hardening, cohesive strengthening, and dispersion strengthening. This observation is further strengthened by the mixed phases associated with methods used in producing the feedstock.

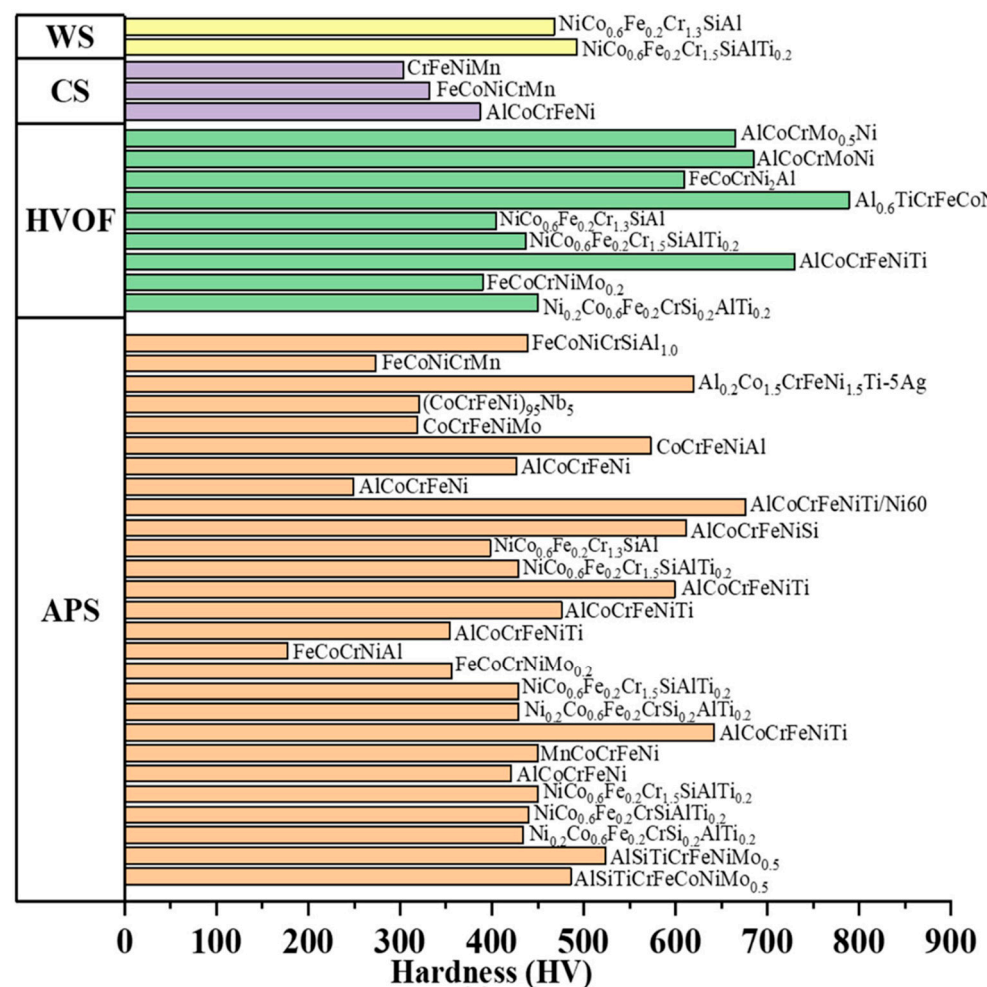


Figure 15. Variation of hardness of various CCA-based coatings through various thermal spray approaches [28].

Most of the coating phases for warm spraying, HVOF, and APS processes were mixtures of FCC, BCC, B_2 , and carbides and oxides of constituent elements. For instance, there is hardness variation between cold sprayed and atmospheric plasma spray coatings. The additional hardness of APS was attributed to additional effects from mixed phases of FCC and BCC, and how these phases interact with one-, two-, and three-dimensional defects across various microstructural length scales. The presence of oxide phases induced by the high-temperature APS is also a contributing factor to the higher hardness

than with the cold spray with predominantly a single phase with no formation of oxides or other precipitates. The comparison of the deposition of Cantor alloy (CrCoFeMnNi) using APS and cold spray showed an interesting trend. The cold sprayed coating had relatively high hardness of ~ 333 HV compared to the APS technique, which had a hardness of ~ 273 HV. This is due to dynamic recrystallization at highly deformed regions resulting from the plastic deformation, increased dislocation density coupled with numerous grain boundaries [19,51,84,86,163,187], and their interactions with various microstructural features and defects (Figure 16). The effect of the overarching mechanisms for adhesion and cohesion, which is metallurgical interlocking, was a contributing factor (Figure 17).

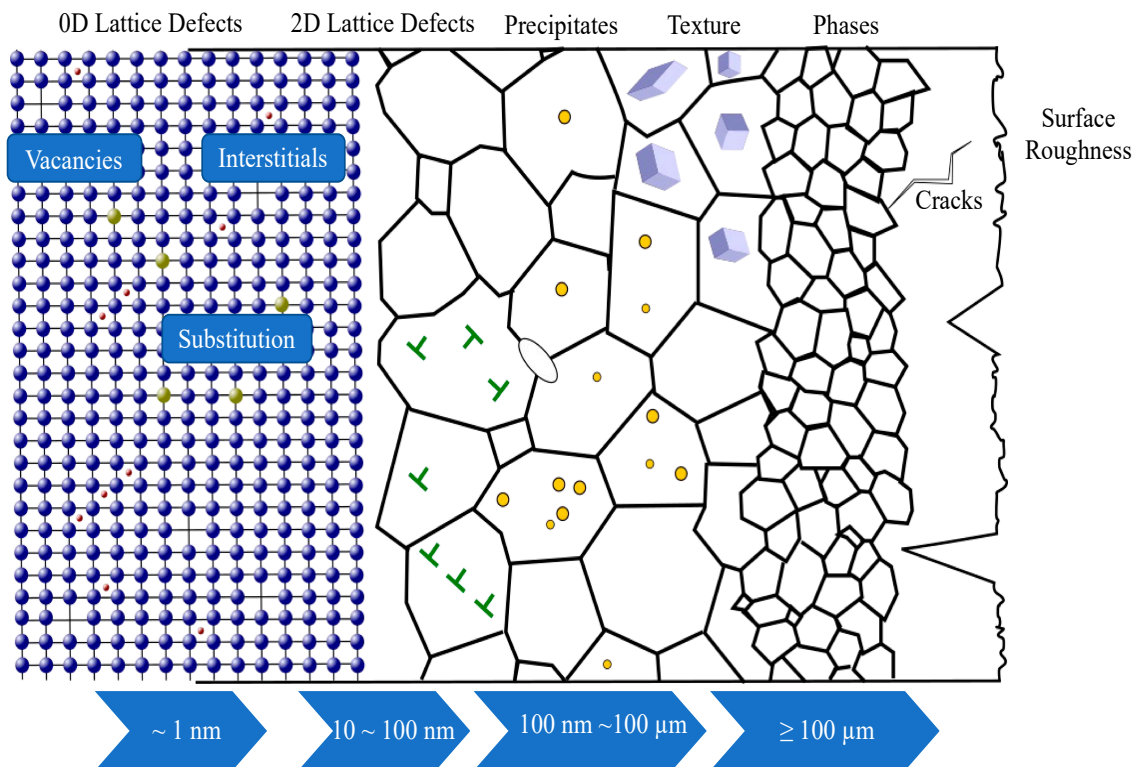


Figure 16. Schematic representation of different types of microstructural defects.

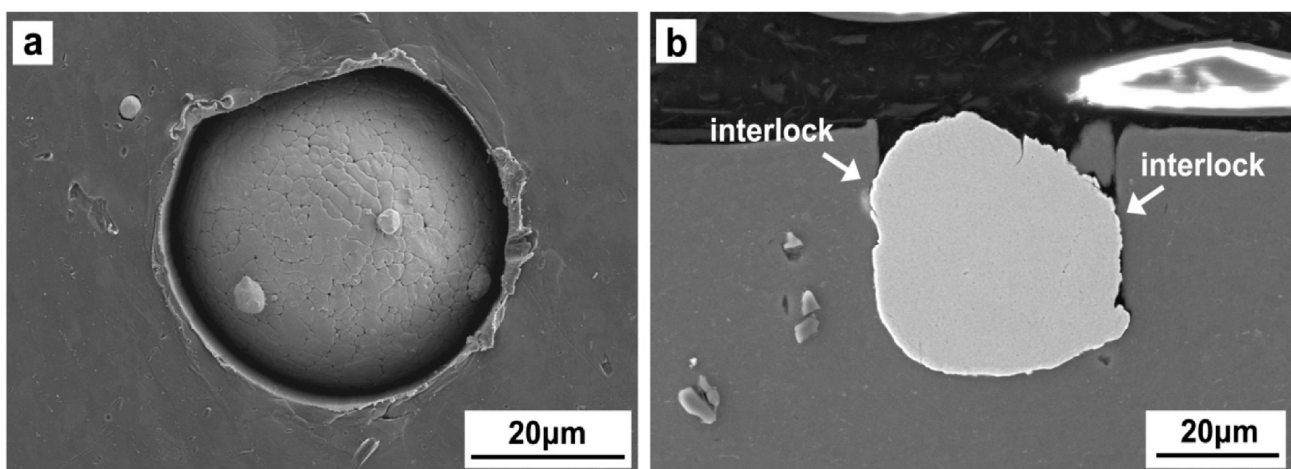


Figure 17. Microstructural characterization of Cantor alloy deposited on Al 6082 substrate showing (a) surface morphology and (b) cross-sectional view with the mechanical interlocking phenomena. Reprinted/adapted with permission from Ref. [200]. Copyright 2019, Elsevier.

The 6061Al and CrCoFeNi composites designed by using cold spray have showed enhanced strength and hardness after friction stir processing [279]. The replacement of conventional ceramic materials with CCAs is due to poor interface wettability between Al matrix composites reinforced with ceramics [289]. The cold spray process induced geometrically necessary dislocations (GNDs) of $17 \times 10^{15} \text{ m}^{-2}$ with an average grain size of 24 μm . The GNDs were further reduced to $9.8 \times 10^{15} \text{ m}^{-2}$ with average grain size of $\sim 4 \mu\text{m}$, resulting in great hardness and strength properties [279]. Although the strength and hardness behavior of CCA-based cold spray coatings are promising, these properties can be enhanced further by optimizing the process parameters of feedstock, cold spray processing parameters, and post-treatment processes.

Cold sprayed CrMnFeNi has been applied by varying the process parameters (feeding rate and gas pressure) with high hardness of $\sim 304 \text{ HV}_{0.3}$ [27]. This value was achieved at gas pressure of 60 bar and feed rate of 1 rpm. The hardness was attributed to work hardening from the severe plastic deformation from the high-impact process of the cold spray technique [19,54,174]. In the case of CrCoFeNi cold spray coatings on AZ91 Mg alloys [284], the hardness was $\sim 315 \text{ HV}$, exceeding conventional Al- and Zn-based cold spray coatings on Mg alloys. The enhanced hardness is due to grain refinement and the high hardness behavior of the CrCoFeNi compared to the Zr and Al alloys [290–297]. Apart from the peening effect resulting in grain refinement of the Mg surfaces, the alpha phase of AZ91 alloy also undergoes dynamic recrystallization contributing to the grain refinement [284].

Fatigue behavior and residual stresses: Fatigue performance of cold spray coatings is enhanced by properties of particles, processing parameters, and metallurgical factors [18]. Excellent fatigue and adhesion strengths were observed for FeCoCrNiMn alloy sprayed on metallic substrate. This was due to dense FeCoCrNiMn coating with optimized process parameters resulting in pancake-like appearance and high flattening ratio and severe grain refinement from the high-energy accelerated particles [18]. The peening effect resulting from the bombardment of the particles on the metallic surface induced high compressive residual stresses [173–175], which led to the high fatigue resistance and the observed adhesion strength [18,172,173]. From the XRD measurement, the maximum compressive residual stress was 200 MPa, about 100 μm from the coating–substrate interface.

Cracks were nucleated at the surface defects [18,172,174]. The first stages of deformation were along the trans-particle paths which were then followed with interparticle and mixed trans-particle fracture mechanisms. The differences in fracture mechanisms are dependent on microstructural features at the coating–substrate and particle–particle interfaces [18,172,174], due to the likelihood of geometric and continuous dynamic recrystallization at these interfaces [170].

The fracture behavior was mainly mixed mode with brittle characteristics during crack propagation and localized fatigue striation characteristics and localized ductile microvoid coalescence resulting from multiple crack initiation sites. The undeformed splat particles and microvoids were stress concentration points accelerating crack propagation rates [172,174].

Corrosion properties: The corrosion and electrochemical behavior of CCA cold spray coatings on various metallic substrates are comparable to their laser cladded or electric arc cladded CCA counterparts. In the case of CrCoFeNi cold spray coatings on AZ91 Mg alloys, an E_{corr} of $\sim -290 \text{ mV}_{\text{SCE}}$ was recorded [284]. The presence of mixed and multilayer oxides and passive films of FeO, Cr_2O_3 , and NiO retarded the rate of dissolution. This reduced the overall corrosion rate, thus improving the corrosion resistance. After 28 days of immersion, about 1% weight loss was recorded and a localized corrosion mechanism was observed with micropits of $\sim 1 \mu\text{m}$ on average [284]. The highly uniform and dense microstructure coupled with stable passive oxide films provide the shielding effect needed and contributed to significant improvement in corrosion resistance.

For most coatings derived from Cantor alloys and their derivatives with relatively high Cr, Mo, and Ni contents, the corrosion resistance is comparable and, in some instances,

better than conventional ferritic and austenitic stainless steels. There is still substantial work required and investigations to be carried out in this area.

6.2.3. Microstructural Characterization of Cold Sprayed CCAs

The microstructural defects associated with cold spray deposits, as for any other thermal spray coatings, include porosity, voids, delamination, spalling, interface contamination, cracks (transverse and interlamellar), pull-outs, oxide clusters, and metallic inclusions. Details of these defects and brief definitions are given in Table 10. Generally, oxides are associated with metallic-based coating systems. By understanding the nature, types, and geometries of the defects in cold spray coatings, a critical mechanical property, fracture toughness, can be assessed and quantified. Fracture toughness is used to estimate the stresses required to propagate or accelerate pre-existing defects or flaws. Generally, the main mechanism of the propagation of cracks or defects highlighted in Table 10 is by intersplat decohesion or intersplat cracking [28,29,297]. This can be further exacerbated by cracks or pores interlinking, pore compaction, and the sliding of splat. There can also be issues of bifurcation of cracks and secondary crack formation contributing to increased fracture surface area [28,29].

Table 10. Typical defects and characteristic features associated with thermal spray processes. Reprinted/adapted with permission from Ref. [29]. Copyright 2023, Taylor and Francis.

Defect Types	Characteristic Features and Definitions
Voids	Characteristic microstructural volume defects which are mainly cracks and porosity
Porosity	Volume defects which are mainly pores or holes within the coating—a characteristic microstructural feature with no particulate matter
Spalling	Defects are a result of flaking, detachment, or peeling of surface particles or coating layers
Delamination	This is associated with separation or cracking of a coating, which could be due to poor adhesion between the coating material and the substrate. This defect can be caused by residual stresses during the spray process. Coatings can delaminate without any applied load
Transverse cracks	These are perpendicular cracks resulting from the coating on the substrate
Interlamellar pores	Defects due to non-homogenous filling along intersplat boundaries attributable to relaxation of vertical stresses and incomplete splat stacking
Interlamellar cracks	These are cracks perpendicular to the substrate and in the vertical direction within the splat microstructure
Oxide stringer	Linear oxide striations that are continuous in nature and run parallel to the coating–substrate interface.
Cluster of oxides	Artifacts or oxide defects grouped together
Pull-outs	Porosity that is artificially induced from unsatisfactory and unwanted metallographic preparation
Metallic inclusions	Brittle metallic particles or compounds within the coating which could be stress concentration points or crack initiation sites

7. Areas for Future Research Direction and Implications

The areas for future research directions should focus on materials, methods, and mechanisms for CCA-based cold spray coating. They are schematically shown in Figure 18. For the materials, focus should be on the 3D transition metal based CCAs and the refractory CCAs. For the methods, the two main cold spray techniques: high-pressure and low-

pressure cold spray techniques, should be explored for depositing CCA-based particles on similar and dissimilar metallic materials. The mechanisms of cold spray coatings for structural integrity and failure modes still require some amount of work. Strategic research directions in each thematic area are discussed in the following.

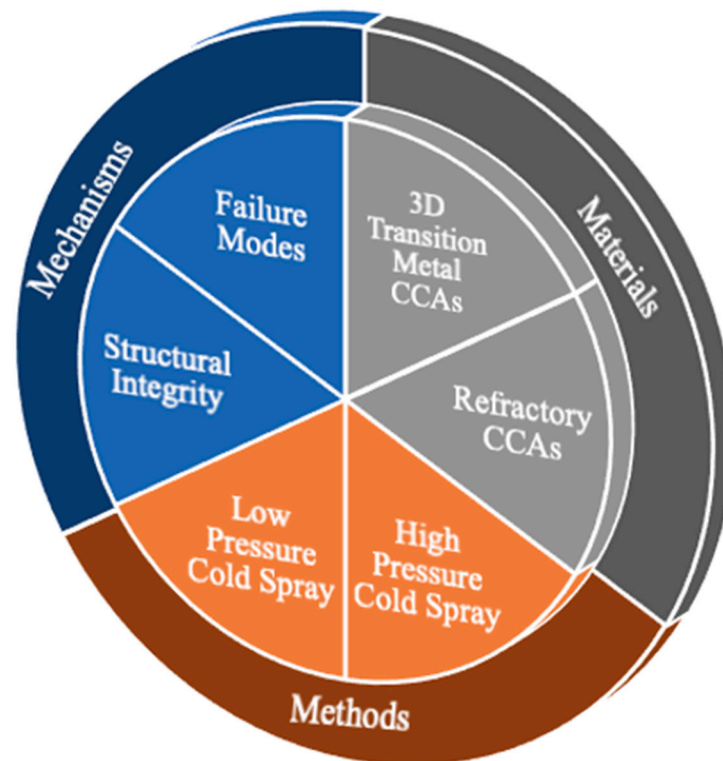


Figure 18. Future perspectives for cold sprayed CCA-based coatings for structural and functional applications.

7.1. Materials

The application of cold spray on dilute metallic alloys as feedstock and substrate has been well studied, although there is still room for improvement. Generally, the process parameters have also been optimized for some systems, especially Cu, Al and Al-based alloys, Ti and Ti-based alloys, Ta and Ta-based alloys, and ferrous alloys. Concerted efforts in simulation-driven cold spray processes have also been carried out, which are thoroughly reviewed in Section 4.

The field of CCAs is less than 30 years old and most of the alloy families show better structural and functional properties than dilute or conventional alloy systems [185,298–300]. As coating material, the classes of CCAs fall under the broad category of 3D transition and refractory metals. When properly developed, these classes of CCAs can be used across the temperature spectrum—from ambient to intermediate to high and ultrahigh temperatures. This will be critical for applications in the thermal barrier coatings (TBCs) for power generation and propulsion [28,29,205,301]. Thus, the CCA-based coatings are best suited for a combination of ambient and high-temperature properties such as strength, oxidation, ductility, thermal stability, and wear resistance. A proof of concept has been carried out using NiCoCrAlSi CCAs through the high-velocity oxy-fuel and air plasma spray (APS) processes as a metallic bond coating for TBCs [205].

Extensive research in the literature showed the elements that are frequently being used for various types of thermal spray applications. They are given in Figure 19 with Cu, Co, Ni, Al, and Fe being the most frequently used elements. Although most of the elements are 3D transition metals, two of the refractory base metals were also used, which could be attributed to the high-temperature oxidation behavior. Figure 19 shows less than

a tenth of the stable metallic elements on the periodic table that could easily be explored for next generation coating materials. This is one of the identified gaps which requires urgent attention and could contribute significantly to understanding the emerging fields of low-cost CCA-based coatings, where the concept of scrap and nature-mixing pre-alloy design concepts can be used.

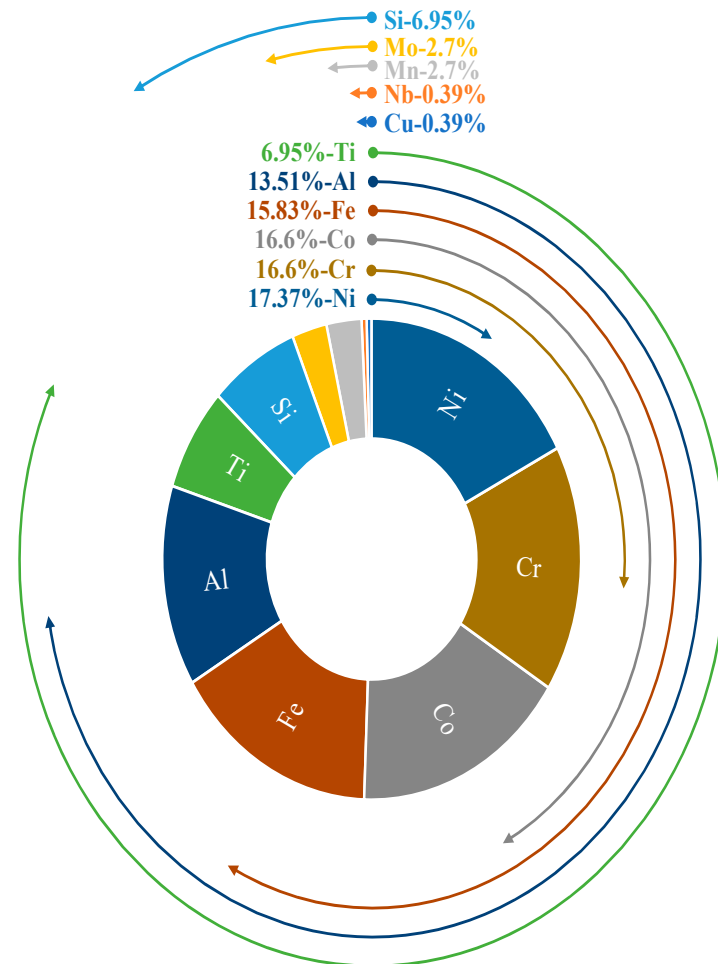


Figure 19. Frequency of use of elements on the periodic table for CCA-based thermal spray coatings as of 2020 [28].

The design and development of new BMG alloys and cold spray coatings with tailored properties are needed for various structural and functional properties. These properties, such as improved mechanical strength, corrosion resistance, and biocompatibility, are critical to produce robust and next generation bulk metallic glass coatings in a cost-effective manner.

7.2. Methods

The two types for cold spray coating are given in Figure 4. These methods need further investigation for depositing pre-alloyed cold spray coating feedstock on various similar and dissimilar substrates of CCAs. Currently, the high-pressure technique is mostly used for most of the coating processes with varying process parameters. Although the results for some classes of CCAs are impressive, the application of cold spray to CCAs is still in its infancy since the first process on CrCoFeMnNi was carried out in 2019 [200]. The search suggests less than 35 research-based articles have been published from 2019 to January 2023. The majority used the high-pressure cold spray approach to deposit the coatings.

Pre-processing of pre-alloyed CCA powders is one area requiring immediate attention. The current powder metallurgy routes such as gas and water atomization and mechanical alloying coupled with spheroidization lead to challenges with oxidation. Approaches such as the ultrasonic atomization process are being explored but could be quite expensive and not easily scalable. Other factors hindering scalability have been highlighted [2,20,185].

Full-scale and detailed mechanical and microstructural characterizations of the particle–substrate and particle–particle interactions need to be ascertained. This will contribute to understanding the mechanism associated with the bond strength. For mechanical characterization, little has been carried out. Therefore, techniques such as tensile adhesion, stud-pull, pin and ring, shear load, peel, laser shock adhesion, scratch, and interfacial indentation tests at the nano- and microscale will be necessary. By conducting thorough mechanical and microstructural assessments, deeper understanding of the physical metallurgy and the mechanisms of these cold spray coatings and how to use them in industrial applications can be implemented effectively.

Porosity is one of the main defects associated with thermal spray coating processes. There is the need to understand the effect of porosity on structural integrity of CCA-based cold spray coatings. Thus, various porosity measurement techniques such as mercury intrusion porosimetry (MIP), gas (He) pycnometry, water absorption or Archimedes (immersion) method, X-ray computed microtomography (CMT), ultrasmall-angle X-ray scattering (USAXS), and electrochemical tests need to be established for the coatings. The working principles of these techniques are reviewed elsewhere [29]. Similarly, measurement of residual stresses using conventional non-destructive methods such as X-ray, synchrotron, laser excitation, and neutron diffraction techniques should also be explored. The implications of these results will contribute to explaining the role of defects in overall structural integrity and overarching mechanisms.

Computational and numerical modeling approaches to studying various aspects of CCA-based cold spray coatings require further attention. Most of these approaches have been adequately discussed for conventional alloys and the highlights are summarized in Section 4. These simulations and physic-based systems can be adapted for CCAs by revisiting the underlying assumptions. By using these computational approaches synergistically with experiments, the concept of rational development of coatings is more guided leveraging from the merits of both approaches. This builds into the material innovation infrastructure where computations, data science and experimental tools are harnessed to design alloys and coatings within acceptable timelines reducing the material lifecycle (concepts to scalable material or coating) significantly.

7.3. Mechanisms

The main underlying mechanisms of cold spray from microstructural perspectives have been metallurgical interlocking and adiabatic heating. This has been shown for most of the dilute or conventional principal element-based alloys. Similar results have been observed for some CCAs, especially the Cantor alloys and their derivatives. This was expected as the compositions are close to highly alloyed stainless steels, Ni-based superalloys, and Ti-based alloys. However, there is the need to investigate the mechanism of bonding and failure modes as these mechanisms, especially solid-state deformation of particles and bonding to the substrate and each other, are yet to be fully understood. The effects and contributions of various microstructural defects are listed in Figure 14 and Table 9.

The interaction between the cocktail of constituent elements and defects such as stacking faults and dislocations and the effects on bonding mechanisms needs further attention. This will necessitate and drive the next frontiers of cold spray coatings to tailor the coating and substrate microstructures.

There is the need to focus research on process optimization for these classes of coatings. This will require understanding of the process parameters such as spray distance, gas pressure, and powder feed rate. The optimized process parameters can lead to improve-

ments in coating properties, such as density, thickness, and adhesion strength. The coating properties can be studied using advanced mechanical and microstructural characterization techniques to establish the relevant nano- and micromechanisms for better understanding of the performance of BMG and CCA cold spray coatings.

Large-scale applications of these coatings are also areas for further research. Issues that could hinder scalability should be investigated and studied for applications in biomedical, aerospace, and automotive industries. Scaling up is relevant to exploring factors that could have been missed during miniature-sized coating fabrications. Translating laboratory-scale curiosity and science to large-scale industrial applications is critical for BMG and CCA cold spray coatings. This will ensure that issues around standardization of coating systems and mechanisms are investigated. This will allow for consistency and uniformity while providing new insights for further research.

8. Summary and Concluding Remarks

A comprehensive overview of cold spray technology as applied to the emerging fields of complex concentrated alloys is presented. Based on the literature and discussions, the summary and concluding remarks are as follows:

- Cold spray involves feedstock produced from CCAs with relatively low particle size distribution. This is true for CCAs with single, metastable, and multiple phases, a critical parameter which enhances the overall mechanical properties at the coating–substrate interface.
- There is a correlation between processing parameters (e.g., critical velocity, spray angle, stand-off distance, gas pressure, and temperature), bonding mechanism, deposition efficiency, adhesion, and cohesion strength of the coating.
- Although the bonding mechanism has been a bone of contention regarding the particle–substrate and particle–particle interaction, metallurgical bonding is the main mechanism. For the CCA-based feedstock on ductile substrate, mechanical interlocking was observed.
- The computational and numerical simulations employed for cold spray processes are reviewed. The challenges associated with the mesh-based and mesh-free finite element methods are highlighted. Although the Johnson–Cook plasticity model is widely used, its inefficiency at relatively high strains was highlighted. Modifications to the JC model as well as others were discussed considering current research applications. Emphasis was on PTW, VA, and ZA models and how they have been applied to dilute alloy designs.
- The fundamental concepts of bulk and coating based on complex concentrated alloys are highlighted. The influence of the core effects of the CCAs and their contributing factors to enhancing the mechanical and microstructural characterization are discussed. The mechanical, chemical, and physical properties are comparable to those of the conventional bulk and coating materials. According to the technology and innovation maturation timeline of CCA-based coatings, the estimated plateau of productivity is expected by 2030.
- Trend analyses of the CCA-based cold spray coatings on various metallic substrates showed less than 40 publications between 2019 and 2023. The major themes in these publications focused on alloy systems for efficient deposition and tuning of microstructural features to induce desirable mechanical properties. Some have looked at wear resistance, post-processing treatments coupled with other manufacturing routes such as friction stir welding, and other forms of additive manufacturing. The main elements which are constantly being explored for cold spray and other thermal spray coatings are C, Cr, Co, Mn, Fe, Ni, Mo, Nb, Si, and Ti. These elements are the base for Cantor alloys and derivatives, and refractory CCAs.
- The strengthening and hardening mechanisms of the CCA-based cold spray coatings are due to work hardening, grain refinement, and dispersion strengthening. This is because of the severe plastic deformation associated with the high-impact velocity

resulting from the bombardment of the feedstock particles onto the substrate. These mechanisms are different from the precipitation hardening, solid solution strengthening, dislocation strengthening, and oxide formation associated with other forms of thermal spray coating techniques. The deformation mechanisms, which are dependent on the energy density, result in localized adiabatic shear as a function of properties of the particles and the process parameters.

- Microstructural defects across different length scales associated with cold spray mechanisms are highlighted. These defects include intergranular cracks, voids, porosities, delamination, transverse cracks, pull-outs, and metallic inclusions. The effects of these defects on structural and functional properties have been discussed.
- The need for rational alloy and coating design approaches is highlighted. The application of computational, numerical, simulation, and experimental approaches for the design of next generation CCA and BMG coatings is required. By using simulations, the processing parameters can be optimized to ensure the designed and desired mechanical properties, while inducing the required microstructural features.
- This overview provides the theoretical framework for new frontiers in developing and accelerating the next generation of CCA-based cold spray coatings. Furthermore, it highlights challenges and open-ended questions that require future research efforts focusing on materials systems (3D transition and refractory metals), cold spray methods (low- and high-pressure cold spray approaches), and mechanisms underlying structural integrity.

Author Contributions: Conceptualization, D.K., M.B., J.v.d.M., N.R. and W.S.; methodology, D.K., T.A., T.B., M.V. and M.B.; formal analysis, D.K., T.A., M.V. and M.B.; investigation, D.K., T.A., M.V. and M.B.; resources, M.B., J.v.d.M., N.R. and W.S.; writing—original draft preparation, D.K., T.A., T.B., M.B. and M.V.; writing—review and editing, D.K., M.B., J.v.d.M., N.R. and W.S.; visualization, D.K., T.A., T.B. and M.V.; supervision, J.v.d.M., N.R. and W.S.; project administration, N.R. and W.S.; funding acquisition, N.R. and W.S. All authors have read and agreed to the published version of the manuscript.

Funding: This research was supported by the Army Research Laboratory (ARL) Grant No. W911NF-19-2-0108. The contributions from the Worcester Polytechnic Institute Global fellowship is also acknowledged.

Institutional Review Board Statement: Not applicable.

Informed Consent Statement: Not applicable.

Data Availability Statement: Not applicable.

Conflicts of Interest: The authors declare no conflict of interest.

References

1. Klenam, D.; Rahbar, N.; Soboyejo, W. Mechanical Properties of Complex Concentrated Alloys: Implications for Structural Integrity. In *Reference Module in Materials Science and Materials Engineering*; Elsevier: Amsterdam, The Netherlands, 2022. [\[CrossRef\]](#)
2. Klenam, D.; Rahbar, N.; Soboyejo, W. Critical Review of Limitations of Equiatomic Composition Alloying Strategy of Complex Concentrated Alloys. In *Reference Module in Materials Science and Materials Engineering*; Elsevier: Amsterdam, The Netherlands, 2022. [\[CrossRef\]](#)
3. Vandadi, M.; Klenam, D.; Rahbar, N.; Soboyejo, W. Advances in the Structural Integrity of Cold Sprayed Alloys—A Critical Review of Process Models and Mechanical Properties. In *Reference Module in Materials Science and Materials Engineering*; Elsevier: Amsterdam, The Netherlands, 2022. [\[CrossRef\]](#)
4. Cantor, B. Multicomponent high-entropy Cantor alloys. *Prog. Mater. Sci.* **2021**, *120*, 100754. [\[CrossRef\]](#)
5. Cantor, B.; Chang, I.T.H.; Knight, P.; Vincent, A.J.B. Microstructural development in equiatomic multicomponent alloys. *Mater. Sci. Eng. A* **2004**, *375–377*, 213–218. [\[CrossRef\]](#)
6. Yin, S.; Cavaliere, P.; Aldwell, B.; Jenkins, R.; Liao, H.; Li, W.; Lupoi, R. Cold spray additive manufacturing and repair: Fundamentals and applications. *Addit. Manuf.* **2018**, *21*, 628–650. [\[CrossRef\]](#)
7. Luo, X.-T.; Li, C.-X.; Shang, F.-L.; Yang, G.-J.; Wang, Y.-Y.; Li, C.-J. High velocity impact induced microstructure evolution during deposition of cold spray coatings: A review. *Surf. Coat. Technol.* **2014**, *254*, 11–20. [\[CrossRef\]](#)
8. Cavaliere, P.; Silvello, A. Crack Repair in Aerospace Aluminum Alloy Panels by Cold Spray. *J. Therm. Spray Technol.* **2017**, *26*, 661–670. [\[CrossRef\]](#)

9. Guo, D.; Kazasidis, M.; Hawkins, A.; Fan, N.; Leclerc, Z.; MacDonald, D.; Nastic, A.; Nikbakht, R.; Ortiz-Fernandez, R.; Rahmati, S.; et al. Cold Spray: Over 30 Years of Development Toward a Hot Future. *J. Therm. Spray Technol.* **2022**, *31*, 866–907. [[CrossRef](#)]
10. Vaz, R.F.; Garfias, A.; Albaladejo, V.; Sanchez, J.; Cano, I.G. A Review of Advances in Cold Spray Additive Manufacturing. *Coatings* **2023**, *13*, 267. [[CrossRef](#)]
11. Kumar, A.; Goyal, D.K.; Kant, R.; Singh, H. Enhancing Corrosion Performance of Cold-Sprayed Titanium/Baghdadite (Ti/BAG) Bio-Composite Coatings via Laser Treatment. *Coatings* **2022**, *12*, 1010. [[CrossRef](#)]
12. Dzhurinskiy, D.; Babu, A.; Dautov, S.; Lama, A.; Mangrulkar, M. Modification of Cold-Sprayed Cu-Al-Ni-Al₂O₃ Composite Coatings by Friction Stir Technique to Enhance Wear Resistance Performance. *Coatings* **2022**, *12*, 1113. [[CrossRef](#)]
13. Chen, X.; Li, C.; Gao, Q.; Duan, X.; Liu, H. Comparison of Microstructure, Microhardness, Fracture Toughness, and Abrasive Wear of WC-17Co Coatings Formed in Various Spraying Ways. *Coatings* **2022**, *12*, 814. [[CrossRef](#)]
14. Cinca, N.; Lavigne, O.; Peres, R.N.; Conze, S.; Hoehn, S.; Dosta, S.; Koivuluoto, H.; Kim, C.; da Silva, F.S.; Matikainen, V.; et al. Electrochemical Corrosion Characterization of Submicron WC-12Co Coatings Produced by CGS and HVOF Compared with Sintered Bulks. *Coatings* **2022**, *12*, 620. [[CrossRef](#)]
15. Manap, A.; Afandi, N.; Mahalingam, S.; Yusof, S.N.A.; Rosli, Z.M. Mechanical and Tribological Study on Aluminum Coatings with High-Pressure and Low-Pressure Cold-Spray Processes. *Coatings* **2022**, *12*, 1792. [[CrossRef](#)]
16. Maev, R.G.; Tjong, J.; Leshchinsky, E.; Pantea, M.; Leshchinsky, V. Cold-Sprayed Multilayer Thermal Barrier–Catalytic Coatings for Engine Pistons: Coatings Design and Properties. *Coatings* **2022**, *12*, 1332. [[CrossRef](#)]
17. Adaan-Nyiaq, M.A.; Tihamiyu, A.A. Recent advances on bonding mechanism in cold spray process: A review of single-particle impact methods. *J. Mater. Res.* **2022**, *38*, 69–95. [[CrossRef](#)] [[PubMed](#)]
18. Cavaliere, P.; Perrone, A.; Silvello, A.; Laska, A.; Blasi, G.; Cano, I.; Sadeghi, B.; Nagy, S. Cyclic behavior of FeCoCrNiMn high entropy alloy coatings produced through cold spray. *J. Alloys Compd.* **2023**, *931*, 167550. [[CrossRef](#)]
19. Champagne, V.; Helfritch, D. Critical Assessment 11: Structural repairs by cold spray. *Mater. Sci. Technol.* **2015**, *31*, 627–634. [[CrossRef](#)]
20. Klenam, D.; Rahbar, N.; Soboyejo, W. Critical Review of Factors Hindering Scalability of Complex Concentrated Alloys. In *Reference Module in Materials Science and Materials Engineering*; Elsevier: Amsterdam, The Netherlands, 2022. [[CrossRef](#)]
21. Lu, K.; Zhu, J.; Guo, D.; Yang, M.; Sun, H.; Wang, Z.; Hui, X.; Wu, Y. Microstructures, Corrosion Resistance and Wear Resistance of High-Entropy Alloys Coatings with Various Compositions Prepared by Laser Cladding: A Review. *Coatings* **2022**, *12*, 1023. [[CrossRef](#)]
22. Li, J.; Huang, Y.; Meng, X.; Xie, Y. A Review on High Entropy Alloys Coatings: Fabrication Processes and Property Assessment. *Adv. Eng. Mater.* **2019**, *21*, 1900343. [[CrossRef](#)]
23. Bagherifard, S.; Guagliano, M. Fatigue performance of cold spray deposits: Coating, repair and additive manufacturing cases. *Int. J. Fatigue* **2020**, *139*, 105744. [[CrossRef](#)]
24. Raelison, R.N.; Verdy, C.; Liao, H. Cold gas dynamic spray additive manufacturing today: Deposit possibilities, technological solutions and viable applications. *Mater. Des.* **2017**, *133*, 266–287. [[CrossRef](#)]
25. Blose, R.; Walker, B.; Walker, R.; Froes, S. New opportunities to use cold spray process for applying additive features to titanium alloys. *Met. Powder Rep.* **2006**, *61*, 30–37. [[CrossRef](#)]
26. Srikanth, A.; Basha, G.M.T.; Venkateshwarlu, B. A Brief Review on Cold Spray Coating Process. *Mater. Today Proc.* **2020**, *22*, 1390–1397. [[CrossRef](#)]
27. Assadi, H.; Gärtner, F.; Stoltenhoff, T.; Kreye, H. Bonding mechanism in cold gas spraying. *Acta Mater.* **2003**, *51*, 4379–4394. [[CrossRef](#)]
28. Meghwal, A.; Anupam, A.; Murty, B.S.; Berndt, C.C.; Kottada, R.S.; Ang, A.S.M. Thermal spray high-entropy alloy coatings: A review. *J. Therm. Spray Technol.* **2020**, *29*, 857–893. [[CrossRef](#)]
29. Ang, A.S.; Berndt, C. A review of testing methods for thermal spray coatings. *Int. Mater. Rev.* **2014**, *59*, 179–223. [[CrossRef](#)]
30. Ahmed, R.; Yu, H.; Stoica, V.; Edwards, L.; Santisteban, J. Neutron diffraction residual strain measurements in post-treated thermal spray cermet coatings. *Mater. Sci. Eng. A* **2008**, *498*, 191–202. [[CrossRef](#)]
31. Suhonen, T.; Varis, T.; Dosta, S.; Torrell, M.; Guilemany, J.M. Residual stress development in cold sprayed Al, Cu and Ti coatings. *Acta Mater.* **2013**, *61*, 6329–6337. [[CrossRef](#)]
32. Valarezo, A.; Sampath, S. An Integrated Assessment of Process-Microstructure-Property Relationships for Thermal-Sprayed NiCr Coatings. *J. Therm. Spray Technol.* **2011**, *20*, 1244–1258. [[CrossRef](#)]
33. Yildirim, B.; Muftu, S.; Gouldstone, A. Modeling of high velocity impact of spherical particles. *Wear* **2011**, *270*, 703–713. [[CrossRef](#)]
34. Shayegan, G.; Mahmoudi, H.; Ghelichi, R.; Villafuerte, J.; Wang, J.; Guagliano, M.; Jahed, H. Residual stress induced by cold spray coating of magnesium AZ31B extrusion. *Mater. Des.* **2014**, *60*, 72–84. [[CrossRef](#)]
35. Li, W.; Yang, K.; Zhang, D.; Zhou, X. Residual Stress Analysis of Cold-Sprayed Copper Coatings by Numerical Simulation. *J. Therm. Spray Technol.* **2016**, *25*, 131–142. [[CrossRef](#)]
36. Lin, E.; Chen, Q.; Ozdemir, O.C.; Champagne, V.K.; Müftü, S. Effects of Interface Bonding on the Residual Stresses in Cold-Sprayed Al-6061: A Numerical Investigation. *J. Therm. Spray Technol.* **2019**, *28*, 472–483. [[CrossRef](#)]
37. Oviedo, F.; Valarezo, A. Residual Stress in High-Velocity Impact Coatings: Parametric Finite Element Analysis Approach. *J. Therm. Spray Technol.* **2020**, *29*, 1268–1288. [[CrossRef](#)]
38. Fardan, A.; Berndt, C.C.; Ahmed, R. Numerical modelling of particle impact and residual stresses in cold sprayed coatings: A review. *Surf. Coat. Technol.* **2021**, *409*, 126835. [[CrossRef](#)]

39. Zhang, K.; Song, Y.; Cai, S.; Wang, Z.; Chen, W.; Xie, L. Multiscale Simulation of Shot-Peening-Assisted Low-Pressure Cold Spraying Based on Al-Zn-Al₂O₃ Coatings. *Coatings* **2022**, *12*, 1490. [\[CrossRef\]](#)
40. Wang, S.; Li, Y.; Yao, M.; Wang, R. Compressive residual stress introduced by shot peening. *J. Mater. Process. Technol.* **1998**, *73*, 64–73. [\[CrossRef\]](#)
41. Wei, Y.-K.; Luo, X.-T.; Li, C.-X.; Li, C.-J. Optimization of In-Situ Shot-Peening-Assisted Cold Spraying Parameters for Full Corrosion Protection of Mg Alloy by Fully Dense Al-Based Alloy Coating. *J. Therm. Spray Technol.* **2017**, *26*, 173–183. [\[CrossRef\]](#)
42. Kobayashi, M.; Matsui, T.; Murakami, Y. Mechanism of creation of compressive residual stress by shot peening. *Int. J. Fatigue* **1998**, *20*, 351–357. [\[CrossRef\]](#)
43. Hammersley, G.; Hackel, L.A.; Harris, F. Surface prestressing to improve fatigue strength of components by laser shot peening. *Opt. Lasers Eng.* **2000**, *34*, 327–337. [\[CrossRef\]](#)
44. Torres, M.A.S.; Voorwald, H.J.C. An evaluation of shot peening, residual stress and stress relaxation on the fatigue life of AISI 4340 steel. *Int. J. Fatigue* **2002**, *24*, 877–886. [\[CrossRef\]](#)
45. Kendall, O.; Paradowska, A.; Abrahams, R.; Reid, M.; Qiu, C.; Mutton, P.; Yan, W. Residual Stress Measurement Techniques for Metal Joints, Metallic Coatings and Components in the Railway Industry: A Review. *Materials* **2023**, *16*, 232. [\[CrossRef\]](#) [\[PubMed\]](#)
46. Song, X.; Everaerts, J.; Zhai, W.; Zheng, H.; Tan, A.W.Y.; Sun, W.; Li, F.; Marinescu, I.; Liu, E.; Korsunsky, A.M. Residual stresses in single particle splat of metal cold spray process—Numerical simulation and direct measurement. *Mater. Lett.* **2018**, *230*, 152–156. [\[CrossRef\]](#)
47. Li, W.; Cao, C.; Yin, S. Solid-state cold spraying of Ti and its alloys: A literature review. *Prog. Mater. Sci.* **2020**, *110*, 100633. [\[CrossRef\]](#)
48. Schmidt, T.; Gärtner, F.; Assadi, H.; Kreye, H. Development of a generalized parameter window for cold spray deposition. *Acta Mater.* **2006**, *54*, 729–742. [\[CrossRef\]](#)
49. Schmidt, T.; Assadi, H.; Gärtner, F.; Richter, H.; Stoltenhoff, T.; Kreye, H.; Klassen, T. From Particle Acceleration to Impact and Bonding in Cold Spraying. *J. Therm. Spray Technol.* **2009**, *18*, 794–808. [\[CrossRef\]](#)
50. Klinkov, S.V.; Kosarev, V.F.; Rein, M. Cold spray deposition: Significance of particle impact phenomena. *Aerosp. Sci. Technol.* **2005**, *9*, 582–591. [\[CrossRef\]](#)
51. Champagne, V.; Nardi, A.; Cote, D. Materials characterization of advanced cold-spray aluminum alloys. *Int. J. Powder Metall.* **2015**, *51*, 37–47.
52. Walker, M. Microstructure and bonding mechanisms in cold spray coatings. *Mater. Sci. Technol.* **2018**, *34*, 2057–2077. [\[CrossRef\]](#)
53. Viscusi, A.; Astarita, A.; Della Gatta, R.; Rubino, F. A perspective review on the bonding mechanisms in cold gas dynamic spray. *Surf. Eng.* **2019**, *35*, 743–771. [\[CrossRef\]](#)
54. Champagne, V.; Helfritch, D. The unique abilities of cold spray deposition. *Int. Mater. Rev.* **2016**, *61*, 437–455. [\[CrossRef\]](#)
55. Hussain, T.; McCartney, D.G.; Shipway, P.H.; Zhang, D. Bonding Mechanisms in Cold Spraying: The Contributions of Metallurgical and Mechanical Components. *J. Therm. Spray Technol.* **2009**, *18*, 364–379. [\[CrossRef\]](#)
56. Grujicic, M.; Saylor, J.; Beasley, D.; DeRosset, W.; Helfritch, D. Computational analysis of the interfacial bonding between feed-powder particles and the substrate in the cold-gas dynamic-spray process. *Appl. Surf. Sci.* **2003**, *219*, 211–227. [\[CrossRef\]](#)
57. Li, W.-Y.; Gao, W. Some aspects on 3D numerical modeling of high velocity impact of particles in cold spraying by explicit finite element analysis. *Appl. Surf. Sci.* **2009**, *255*, 7878–7892. [\[CrossRef\]](#)
58. Aleksieieva, O.; Dereviankina, L.; Breuninger, P.; Bozoglu, M.; Tretiakov, P.; Toporov, A.; Antonyuk, S. Simulation of Particle Interaction with Surface Microdefects during Cold Gas-Dynamic Spraying. *Coatings* **2022**, *12*, 1297. [\[CrossRef\]](#)
59. Nélias, D.; Xie, J.; Walter-Le Berre, H.; Ichikawa, Y.; Ogawa, K. Simulation of the Cold Spray Deposition Process for Aluminum and Copper using Lagrangian, ALE and CEL Methods. In *Thermomechanical Industrial Processes: Modeling and Numerical Simulation*; Bergheau, J.-M., Ed.; John Wiley & Sons, Inc.: Hoboken, NJ, USA, 2014; pp. 321–358.
60. Xie, J.; Nelias, D.; Berre, H.W.-L.; Ogawa, K.; Ichikawa, Y. Simulation of the Cold Spray Particle Deposition Process. *J. Tribol.* **2015**, *137*, 041101. [\[CrossRef\]](#)
61. Li, W.-Y.; Liao, H.; Li, C.-J.; Li, G.; Coddet, C.; Wang, X. On high velocity impact of micro-sized metallic particles in cold spraying. *Appl. Surf. Sci.* **2006**, *253*, 2852–2862. [\[CrossRef\]](#)
62. Li, W.-Y.; Zhang, C.; Li, C.-J.; Liao, H. Modeling Aspects of High Velocity Impact of Particles in Cold Spraying by Explicit Finite Element Analysis. *J. Therm. Spray Technol.* **2009**, *18*, 921–933. [\[CrossRef\]](#)
63. Panfilov, P.; Gornostyrev, Y.N.; Kuznetsov, A.R. Breakdown of relationship between chemical bonding and deformation behavior of crystalline materials. *TMS Annu. Meet.* **2010**, *2*, 13–24.
64. Li, W.-Y.; Yang, K.; Yin, S.; Guo, X.P. Numerical Analysis of Cold Spray Particles Impacting Behavior by the Eulerian Method: A Review. *J. Therm. Spray Technol.* **2016**, *25*, 1441–1460. [\[CrossRef\]](#)
65. Hemeda, A.; Zhang, C.; Hu, X.; Fukuda, D.; Cote, D.; Nault, I.; Nardi, A.; Champagne, V.; Ma, Y.; Palko, J. Particle-based simulation of cold spray: Influence of oxide layer on impact process. *Addit. Manuf.* **2021**, *37*, 101517. [\[CrossRef\]](#)
66. Liu, M.B.; Liu, G.R. Smoothed Particle Hydrodynamics (SPH): An Overview and Recent Developments. *Arch. Comput. Methods Eng.* **2010**, *17*, 25–76. [\[CrossRef\]](#)
67. Hoover, W.; Hoover, C.; Kum, O.; Castillo, V. Smooth particle applied mechanics. *Comput. Methods Sci. Technol.* **1996**, *2*, 65–72. [\[CrossRef\]](#)
68. Liu, G.R.; Liu, M.B. *Smoothed Particle Hydrodynamics—A Meshfree Particle Method*; World Scientific Publishing Company: Singapore, 2003.

69. Shadloo, M.; Oger, G.; Le Touzé, D. Smoothed particle hydrodynamics method for fluid flows, towards industrial applications: Motivations, current state, and challenges. *Comput. Fluids* **2016**, *136*, 11–34. [[CrossRef](#)]
70. Lemiale, V.; King, P.; Rudman, M.; Prakash, M.; Cleary, P.; Jahedi, M.; Gulizia, S. Temperature and strain rate effects in cold spray investigated by smoothed particle hydrodynamics. *Surf. Coat. Technol.* **2014**, *254*, 121–130. [[CrossRef](#)]
71. Gnanasekaran, B.; Liu, G.-R.; Fu, Y.; Wang, G.; Niu, W.; Lin, T. A Smoothed Particle Hydrodynamics (SPH) procedure for simulating cold spray process—A study using particles. *Surf. Coat. Technol.* **2019**, *377*, 124812. [[CrossRef](#)]
72. Li, W.-Y.; Yin, S.; Wang, X.-F. Numerical investigations of the effect of oblique impact on particle deformation in cold spraying by the SPH method. *Appl. Surf. Sci.* **2010**, *256*, 3725–3734. [[CrossRef](#)]
73. Yin, S.; Wang, X.-F.; Xu, B.-P.; Li, W.-Y. Examination on the Calculation Method for Modeling the Multi-Particle Impact Process in Cold Spraying. *J. Therm. Spray Technol.* **2010**, *19*, 1032–1041. [[CrossRef](#)]
74. King, P.C.; Bae, G.; Zahiri, S.H.; Jahedi, M.; Lee, C. An Experimental and Finite Element Study of Cold Spray Copper Impact onto Two Aluminum Substrates. *J. Therm. Spray Technol.* **2010**, *19*, 620–634. [[CrossRef](#)]
75. Yin, S.; Wang, X.-F.; Li, W.-Y.; Xu, B.-P. Numerical Investigation on Effects of Interactions Between Particles on Coating Formation in Cold Spraying. *J. Therm. Spray Technol.* **2009**, *18*, 686–693. [[CrossRef](#)]
76. Bolelli, G.; Dosta, S.; Lusvarghi, L.; Manfredini, T.; Guilemany, J.; Cano, I. Building up WC-Co coatings by cold spray: A finite element simulation. *Surf. Coat. Technol.* **2019**, *374*, 674–689. [[CrossRef](#)]
77. Song, X.; Ng, K.L.; Chea, J.M.-K.; Sun, W.; Tan, A.W.-Y.; Zhai, W.; Li, F.; Marinescu, I.; Liu, E. Coupled Eulerian-Lagrangian (CEL) simulation of multiple particle impact during Metal Cold Spray process for coating porosity prediction. *Surf. Coat. Technol.* **2020**, *385*, 125433. [[CrossRef](#)]
78. Li, Y.; Wang, X.-F.; Yin, S.; Xu, S.-L. Influence of Particle Initial Temperature on High Velocity Impact Process in Cold Spraying. *Procedia Environ. Sci.* **2012**, *12*, 298–304. [[CrossRef](#)]
79. Morris, J.P.; Fox, P.J.; Zhu, Y. Modeling Low Reynolds Number Incompressible Flows Using SPH. *J. Comput. Phys.* **1997**, *136*, 214–226. [[CrossRef](#)]
80. Liu, M.; Liu, G.; Lam, K. Constructing smoothing functions in smoothed particle hydrodynamics with applications. *J. Comput. Appl. Math.* **2003**, *155*, 263–284. [[CrossRef](#)]
81. Lucy, L.B. A numerical approach to the testing of the fission hypothesis. *Astron. J.* **1977**, *82*, 1013–1024. [[CrossRef](#)]
82. Chun, D.-M.; Ahn, S.-H. Deposition mechanism of dry sprayed ceramic particles at room temperature using a nano-particle deposition system. *Acta Mater.* **2011**, *59*, 2693–2703. [[CrossRef](#)]
83. Park, H.; Kwon, J.; Lee, I.; Lee, C. Shock-induced plasticity and fragmentation phenomena during alumina deposition in the vacuum kinetic spraying process. *Scr. Mater.* **2015**, *100*, 44–47. [[CrossRef](#)]
84. Manap, A.; Nooririnah, O.; Misran, H.; Okabe, T.; Ogawa, K. Experimental and SPH study of cold spray impact between similar and dissimilar metals. *Surf. Eng.* **2014**, *30*, 335–341. [[CrossRef](#)]
85. Vural, M.; Ravichandran, G.; Rittel, D. Large strain mechanical behavior of 1018 cold-rolled steel over a wide range of strain rates. *Met. Mater. Trans. A* **2003**, *34*, 2873–2885. [[CrossRef](#)]
86. Johnson, G.R.; Cook, W.H. Fracture characteristics of three metals subjected to various strains, strain rates, temperatures and pressures. *Eng. Fract. Mech.* **1985**, *21*, 31–48. [[CrossRef](#)]
87. Preston, D.L.; Tonks, D.L.; Wallace, D.C. Model of plastic deformation for extreme loading conditions. *J. Appl. Phys.* **2003**, *93*, 211–220. [[CrossRef](#)]
88. Grujicic, M.; Zhao, C.; DeRosset, W.; Helfritsch, D. Adiabatic shear instability based mechanism for particles/substrate bonding in the cold-gas dynamic-spray process. *Mater. Des.* **2004**, *25*, 681–688. [[CrossRef](#)]
89. Rahmati, S.; Ghaei, A. The Use of Particle/Substrate Material Models in Simulation of Cold-Gas Dynamic-Spray Process. *J. Therm. Spray Technol.* **2014**, *23*, 530–540. [[CrossRef](#)]
90. Bae, G.; Xiong, Y.; Kumar, S.; Kang, K.; Lee, C. General aspects of interface bonding in kinetic sprayed coatings. *Acta Mater.* **2008**, *56*, 4858–4868. [[CrossRef](#)]
91. Guetta, D.; Berger, M.-H.; Borit, F.; Guipont, V.; Jeandin, M.; Boustie, M.; Ichikawa, Y.; Sakaguchi, K.; Ogawa, K. Influence of Particle Velocity on Adhesion of Cold-Sprayed Splats. *J. Therm. Spray Technol.* **2009**, *18*, 331–342. [[CrossRef](#)]
92. Hassani-Gangaraj, M.; Veysset, D.; Champagne, V.K.; Nelson, K.A.; Schuh, C.A. Adiabatic shear instability is not necessary for adhesion in cold spray. *Acta Mater.* **2018**, *158*, 430–439. [[CrossRef](#)]
93. Ahmed, R.A.; Rahneshein, V.; Bond, T.; Vandadi, M.; Oghenevweta, J.E.; Navabi, A.; Oyewole, O.K.; Obayemi, J.D.; Rahbar, N.; Soboyejo, W.O. On the Role of Deformation and Cracking in the Cold Spray Processing of Refractory Ta Powders onto Ta or 4340 Steel Substrates: Effects of Topical Oxide Layers and Spray Velocity. *Met. Mater. Trans. A* **2022**, *53*, 3381–3391. [[CrossRef](#)]
94. Navabi, A.; Vandadi, M.; Bond, T.; Rahneshein, V.; Obayemi, J.; Ahmed, R.; Oghenevweta, J.; Champagne, V.; Rahbar, N.; Soboyejo, W. Deformation and cracking phenomena in cold sprayed 6061 Al alloy powders with nanoscale aluminum oxide films. *Mater. Sci. Eng. A* **2022**, *841*, 143036. [[CrossRef](#)]
95. Bansal, P.; Shipway, P.; Leen, S. A hybrid implicit—Explicit finite element methodology for coating formation in the high-velocity oxy-fuel spraying process. *Proc. Inst. Mech. Eng. L J. Mater. Des. Appl.* **2007**, *221*, 285–297. [[CrossRef](#)]
96. Micunovic, M.; Albertini, C.; Montagnani, M. High Strain Rate Thermo-Inelasticity of Damaged AISI 316H. *Int. J. Damage Mech.* **2003**, *12*, 267–303. [[CrossRef](#)]

97. Ghelichi, R.; Bagherifard, S.; Guagliano, M.; Verani, M. Numerical simulation of cold spray coating. *Surf. Coat. Technol.* **2011**, *205*, 5294–5301. [[CrossRef](#)]
98. Zhang, D.-N.; Shangguan, Q.-Q.; Xie, C.-J.; Liu, F. A modified Johnson–Cook model of dynamic tensile behaviors for 7075-T6 aluminum alloy. *J. Alloys Compd.* **2015**, *619*, 186–194. [[CrossRef](#)]
99. Lin, Y.; Chen, X.-M.; Liu, G. A modified Johnson–Cook model for tensile behaviors of typical high-strength alloy steel. *Mater. Sci. Eng. A* **2010**, *527*, 6980–6986. [[CrossRef](#)]
100. Chakrabarty, R.; Song, J. A modified Johnson–Cook material model with strain gradient plasticity consideration for numerical simulation of cold spray process. *Surf. Coat. Technol.* **2020**, *397*, 125981. [[CrossRef](#)]
101. Zhao, Y.; Sun, J.; Li, J.; Yan, Y.; Wang, P. A comparative study on Johnson–Cook and modified Johnson–Cook constitutive material model to predict the dynamic behavior laser additive manufacturing FeCr alloy. *J. Alloys Compd.* **2017**, *723*, 179–187. [[CrossRef](#)]
102. Rahmati, S.; Jodoin, B. Physically Based Finite Element Modeling Method to Predict Metallic Bonding in Cold Spray. *J. Therm. Spray Technol.* **2020**, *29*, 611–629. [[CrossRef](#)]
103. Su, J.; Kang, J.-J.; Yue, W.; Ma, G.-Z.; Fu, Z.-Q.; Zhu, L.-N.; She, D.-S.; Wang, H.-D.; Wang, C.-B. Review of cold spraying and its use for metallic glass coatings. *Mater. Sci. Technol.* **2019**, *35*, 1908–1923. [[CrossRef](#)]
104. Jočbalis, G.; Kačianauskas, R.; Borodinas, S.; Rojek, J. Comparative numerical study of rate-dependent continuum-based plasticity models for high-velocity impacts of copper particles against a substrate. *Int. J. Impact Eng.* **2023**, *172*, 104394. [[CrossRef](#)]
105. Henao, J.; Bolelli, G.; Concustell, A.; Lusvardi, L.; Dosta, S.; Cano, I.; Guilemany, J. Deposition behavior of cold-sprayed metallic glass particles onto different substrates. *Surf. Coat. Technol.* **2018**, *349*, 13–23. [[CrossRef](#)]
106. Grujicic, M.; Pandurangan, B.; Yen, C.-F.; Cheeseman, B.A. Modifications in the AA5083 Johnson–Cook Material Model for Use in Friction Stir Welding Computational Analyses. *J. Mater. Eng. Perform.* **2012**, *21*, 2207–2217. [[CrossRef](#)]
107. Chen, Q.; Alizadeh, A.; Xie, W.; Wang, X.; Champagne, V.; Gouldstone, A.; Lee, J.-H.; Müftü, S. High-Strain-Rate Material Behavior and Adiabatic Material Instability in Impact of Micron-Scale Al-6061 Particles. *J. Therm. Spray Technol.* **2018**, *27*, 641–653. [[CrossRef](#)]
108. Schreiber, J.; Smid, I.; Eden, T.; Koudela, K.; Cote, D.; Champagne, V. Cold spray particle impact simulation using the Preston–Tonks–Wallace plasticity model. *Finite Elem. Anal. Des.* **2021**, *191*, 103557. [[CrossRef](#)]
109. Banerjee, B. An evaluation of plastic flow stress models for the simulation of high-temperature and high-strain-rate deformation of metals. *arXiv* **2005**, arXiv:cond-mat/0512466.
110. Fraser, K.; Kiss, L.I.; St-Georges, L.; Drolet, D. Optimization of Friction Stir Weld Joint Quality Using a Meshfree Fully-Coupled Thermo-Mechanics Approach. *Metals* **2018**, *8*, 101. [[CrossRef](#)]
111. Weiller, S.; Delloro, F. A numerical study of pore formation mechanisms in aluminium cold spray coatings. *Addit. Manuf.* **2022**, *60*, 103193. [[CrossRef](#)]
112. Henao, J.; Concustell, A.; Dosta, S.; Cinca, N.; Cano, I.G.; Guilemany, J.M. Influence of the Substrate on the Formation of Metallic Glass Coatings by Cold Gas Spraying. *J. Therm. Spray Technol.* **2016**, *25*, 992–1008. [[CrossRef](#)]
113. Voyiadjis, G.Z.; Abed, F.H. Microstructural based models for bcc and fcc metals with temperature and strain rate dependency. *Mech. Mater.* **2005**, *37*, 355–378. [[CrossRef](#)]
114. Abed, F.H.; Voyiadjis, G.Z. A consistent modified Zerilli–Armstrong flow stress model for BCC and FCC metals for elevated temperatures. *Acta Mech.* **2005**, *175*, 1–18. [[CrossRef](#)]
115. Khan, A.S.; Liang, R. Behaviors of three BCC metal over a wide range of strain rates and temperatures: Experiments and modeling. *Int. J. Plast.* **1999**, *15*, 1089–1109. [[CrossRef](#)]
116. Khan, A.S.; Liang, R. Behaviors of three BCC metals during non-proportional multi-axial loadings: Experiments and modeling. *Int. J. Plast.* **2000**, *16*, 1443–1458. [[CrossRef](#)]
117. Gao, C.; Zhang, L. Constitutive modelling of plasticity of fcc metals under extremely high strain rates. *Int. J. Plast.* **2012**, *32–33*, 121–133. [[CrossRef](#)]
118. Telford, M. The base for bulk metallic glass. *Mater. Today* **2003**, *7*, 36–43. [[CrossRef](#)]
119. Suryanarayana, C.; Inoue, A. Iron-based bulk metallic glasses. *Int. Mater. Rev.* **2013**, *58*, 131–166. [[CrossRef](#)]
120. Wang, Q.; Han, P.; Yin, S.; Niu, W.-J.; Zhai, L.; Li, X.; Mao, X.; Han, Y. Current Research Status on Cold Sprayed Amorphous Alloy Coatings: A Review. *Coatings* **2021**, *11*, 206. [[CrossRef](#)]
121. Miracle, D.B. A structural model for metallic glasses. *Nat. Mater.* **2004**, *3*, 697–702. [[CrossRef](#)] [[PubMed](#)]
122. Miracle, D.B. A Structural Model for Metallic Glasses. *Microsc. Microanal.* **2004**, *10* (Suppl. 2), 786–787. [[CrossRef](#)]
123. Inoue, A.; Takeuchi, A. Recent development and application products of bulk glassy alloys. *Acta Mater.* **2011**, *59*, 2243–2267. [[CrossRef](#)]
124. Das, J.; Tang, M.B.; Kim, K.B.; Theissmann, R.; Baier, F.; Wang, W.H.; Eckert, J. “Work-Hardenable” Ductile Bulk Metallic Glass. *Phys. Rev. Lett.* **2005**, *94*, 205501. [[CrossRef](#)]
125. Greer, J.R.; De Hosson, J.T. Plasticity in small-sized metallic systems: Intrinsic versus extrinsic size effect. *Prog. Mater. Sci.* **2011**, *56*, 654–724. [[CrossRef](#)]
126. Greer, A.; Cheng, Y.; Ma, E. Shear bands in metallic glasses. *Mater. Sci. Eng. R Rep.* **2013**, *74*, 71–132. [[CrossRef](#)]
127. Gao, M.; Lu, W.; Yang, B.; Zhang, S.; Wang, J. High corrosion and wear resistance of Al-based amorphous metallic coating synthesized by HVAF spraying. *J. Alloys Compd.* **2018**, *735*, 1363–1373. [[CrossRef](#)]
128. Shen, Y.; Perepezko, J. Al-based amorphous alloys: Glass-forming ability, crystallization behavior and effects of minor alloying additions. *J. Alloys Compd.* **2017**, *707*, 3–11. [[CrossRef](#)]

129. Goldman, M.E.; Ünlü, N.; Shiflet, G.J.; Scully, J.R. Selected Corrosion Properties of a Novel Amorphous Al-Co-Ce Alloy System. *Electrochem. Solid-State Lett.* **2005**, *8*, B1. [\[CrossRef\]](#)
130. Wang, D.; Li, P. Thermodynamic and mechanical properties of Cu–Zr–Al–Ti bulk metallic glasses. *AIP Adv.* **2018**, *8*, 125003. [\[CrossRef\]](#)
131. Wang, Y.; Li, M.; Sun, L.; Zhang, X.; Shen, J. Environmentally assisted fracture behavior of Fe-based amorphous coatings in chloride-containing solutions. *J. Alloys Compd.* **2018**, *738*, 37–48. [\[CrossRef\]](#)
132. Lin, J.; Wang, Z.; Cheng, J.; Kang, M.; Fu, X.; Hong, S. Effect of Initial Surface Roughness on Cavitation Erosion Resistance of Arc-Sprayed Fe-Based Amorphous/Nanocrystalline Coatings. *Coatings* **2017**, *7*, 200. [\[CrossRef\]](#)
133. Yasir, M.; Zhang, C.; Wang, W.; Xu, P.; Liu, L. Wear behaviors of Fe-based amorphous composite coatings reinforced by Al₂O₃ particles in air and in NaCl solution. *Mater. Des.* **2015**, *88*, 207–213. [\[CrossRef\]](#)
134. Qiao, J.-H.; Jin, X.; Qin, J.-H.; Liu, H.-T.; Luo, Y.; Zhang, D.-K. A super-hard superhydrophobic Fe-based amorphous alloy coating. *Surf. Coat. Technol.* **2018**, *334*, 286–291. [\[CrossRef\]](#)
135. Zhou, H.; Zhang, C.; Wang, W.; Yasir, M.; Liu, L. Microstructure and Mechanical Properties of Fe-based Amorphous Composite Coatings Reinforced by Stainless Steel Powders. *J. Mater. Sci. Technol.* **2015**, *31*, 43–47. [\[CrossRef\]](#)
136. Bahrami, F.; Amini, R.; Taghvaei, A.H. Microstructure and corrosion behavior of electrodeposited Ni-based nanocomposite coatings reinforced with Ni 60 Cr 10 Ta 10 P 16 B 4 metallic glass particles. *J. Alloys Compd.* **2017**, *714*, 530–536. [\[CrossRef\]](#)
137. Suresh, K.; Yugeswaran, S.; Rao, K.; Kobayashi, A.; Shum, P. Sliding wear behavior of gas tunnel type plasma sprayed Ni-based metallic glass composite coatings. *Vacuum* **2013**, *88*, 114–117. [\[CrossRef\]](#)
138. Wang, B.; Xu, K.; Shi, X.; Zhang, M.; Qiao, J.; Gao, C.; Wu, Y. Electrochemical and chemical corrosion behaviors of the in-situ Zr-based metallic glass matrix composites in chloride-containing solutions. *J. Alloys Compd.* **2019**, *770*, 679–685. [\[CrossRef\]](#)
139. Zhang, Y.; Yan, L.; Zhao, X.; Ma, L. Enhanced chloride ion corrosion resistance of Zr-based bulk metallic glasses with cobalt substitution. *J. Non-Cryst. Solids* **2018**, *496*, 18–23. [\[CrossRef\]](#)
140. Astarita, A.; Coticelli, F.; Prisco, U. Repairing of an Engine Block Through the Cold Gas Dynamic Spray Technology. *Mater. Res.* **2016**, *19*, 1226–1231. [\[CrossRef\]](#)
141. Concustell, A.; Henao, J.; Dosta, S.; Cinca, N.; Cano, I.; Guilemany, J. On the formation of metallic glass coatings by means of Cold Gas Spray technology. *J. Alloys Compd.* **2015**, *651*, 764–772. [\[CrossRef\]](#)
142. Moridi, A.; Hassani-Gangaraj, S.M.; Guagliano, M.; Dao, M. Cold spray coating: Review of material systems and future perspectives. *Surf. Eng.* **2014**, *30*, 369–395. [\[CrossRef\]](#)
143. Su, J.; Kang, J.-J.; Yue, W.; Ma, G.-Z.; Fu, Z.-Q.; Zhu, L.-N.; She, D.-S.; Wang, H.-D.; Wang, C.-B. Comparison of tribological behavior of Fe-based metallic glass coatings fabricated by cold spraying and high velocity air fuel spraying. *J. Non-Cryst. Solids* **2019**, *522*, 119582. [\[CrossRef\]](#)
144. Henao, J.; Concustell, A.; Cano, I.G.; Dosta, S.; Cinca, N.; Guilemany, J.M.; Suhonen, T. Novel Al-based metallic glass coatings by Cold Gas Spray. *Mater. Des.* **2016**, *94*, 253–261. [\[CrossRef\]](#)
145. Lahiri, D.; Gill, P.K.; Scudino, S.; Zhang, C.; Singh, V.; Karthikeyan, J.; Munroe, N.; Seal, S.; Agarwal, A. Cold sprayed aluminum based glassy coating: Synthesis, wear and corrosion properties. *Surf. Coat. Technol.* **2013**, *232*, 33–40. [\[CrossRef\]](#)
146. List, A.; Gärtner, F.; Mori, T.; Schulze, M.; Assadi, H.; Kuroda, S.; Klassen, T. Cold Spraying of Amorphous Cu₅₀Zr₅₀ Alloys. *J. Therm. Spray Technol.* **2014**, *24*, 108–118. [\[CrossRef\]](#)
147. Yoon, S.; Bae, G.; Xiong, Y.; Kumar, S.; Kang, K.; Kim, J.-J.; Lee, C. Strain-enhanced nanocrystallization of a CuNiTiZr bulk metallic glass coating by a kinetic spraying process. *Acta Mater.* **2009**, *57*, 6191–6199. [\[CrossRef\]](#)
148. Ajdelsztajn, L.; Jodoin, B.; Richer, P.; Sansoucy, E.; Lavernia, E.J. Cold Gas Dynamic Spraying of Iron-Base Amorphous Alloy. *J. Therm. Spray Technol.* **2006**, *15*, 495–500. [\[CrossRef\]](#)
149. Yoon, S.; Kim, J.; Bae, G.; Kim, B.; Lee, C. Formation of coating and tribological behavior of kinetic sprayed Fe-based bulk metallic glass. *J. Alloys Compd.* **2011**, *509*, 347–353. [\[CrossRef\]](#)
150. List, A.; Gärtner, F.; Schmidt, T.; Klassen, T. Impact Conditions for Cold Spraying of Hard Metallic Glasses. *J. Therm. Spray Technol.* **2012**, *21*, 531–540. [\[CrossRef\]](#)
151. Choi, H.; Yoon, S.; Kim, G.; Jo, H.; Lee, C. Phase evolutions of bulk amorphous NiTiZrSiSn feedstock during thermal and kinetic spraying processes. *Scr. Mater.* **2005**, *53*, 125–130. [\[CrossRef\]](#)
152. Yoon, S.; Lee, C.; Choi, H.; Jo, H. Kinetic spraying deposition behavior of bulk amorphous NiTiZrSiSn feedstock. *Mater. Sci. Eng. A* **2006**, *415*, 45–52. [\[CrossRef\]](#)
153. Kang, N.; Coddet, P.; Liao, H.; Coddet, C. The effect of heat treatment on microstructure and tensile properties of cold spray Zr base metal glass/Cu composite. *Surf. Coat. Technol.* **2015**, *280*, 64–71. [\[CrossRef\]](#)
154. Zhang, S.; Wang, Z.; Chang, X.; Hou, W.; Wang, J. Identifying the role of nanoscale heterogeneities in pitting behaviour of Al-based metallic glass. *Corros. Sci.* **2011**, *53*, 3007–3015. [\[CrossRef\]](#)
155. Jeong, J.I.; Lee, S.H.; Jeon, J.-B.; Kim, S.J. Excessively High Vapor Pressure of Al-Based Amorphous Alloys. *Metals* **2015**, *5*, 1878–1886. [\[CrossRef\]](#)
156. Sansoucy, E.; Kim, G.; Moran, A.; Jodoin, B. Mechanical Characteristics of Al-Co-Ce Coatings Produced by the Cold Spray Process. *J. Therm. Spray Technol.* **2007**, *16*, 651–660. [\[CrossRef\]](#)
157. Xueqing, W.; Mo, M.; Chaogui, T.; Xiufeng, W.; Jianguo, L. Comparative Study on Thermodynamical and Electrochemical Behavior of Al₈₈Ni₆La₆ and Al₈₆Ni₆La₆Cu₂ Amorphous Alloys. *J. Rare Earths* **2007**, *25*, 381–384. [\[CrossRef\]](#)

158. Wang, X.; Wu, X.; Lin, J.; Ma, M. The influence of heat treatment on the corrosion behaviour of as-spun amorphous Al88Ni6La6 alloy in 0.01 M NaCl solution. *Mater. Lett.* **2007**, *61*, 1715–1717. [[CrossRef](#)]
159. Wu, J.; Peng, Z. Effects of microadditions on glass transition and hardness of Cu-based bulk metallic glasses. *Appl. Phys. A* **2018**, *124*, 632. [[CrossRef](#)]
160. Kim, J.; Kang, K.; Yoon, S.; Lee, C. Enhancement of metallic glass properties of Cu-based BMG coating by shroud plasma spraying. *Surf. Coat. Technol.* **2011**, *205*, 3020–3026. [[CrossRef](#)]
161. Lee, K.-A.; Jung, D.J.; Park, D.Y.; Kang, W.G.; Lee, J.K.; Kim, H.J. Study on the fabrication and physical properties of cold-sprayed, Cu-based amorphous coating. *J. Phys. Conf. Ser.* **2009**, *144*, 012113. [[CrossRef](#)]
162. Kim, K.-H.; Lee, S.-W.; Ahn, J.-P.; Fleury, E.; Kim, Y.-C.; Lee, J.-C. A Cu-based amorphous alloy with a simultaneous improvement in its glass forming ability and plasticity. *Met. Mater. Int.* **2007**, *13*, 21–24. [[CrossRef](#)]
163. Aldhameer, A.; El-Eskandarany, M.S.; Kishk, M.; Alajmi, F.; Banyan, M. Mechanical Alloying Integrated with Cold Spray Coating for Fabrication Cu₅₀(Ti_{50-x}Ni_x), x; 10, 20, 30, and 40 at.% Antibiofilm Metallic Glass Coated/SUS304 Sheets. *Nanomaterials* **2022**, *12*, 1681. [[CrossRef](#)]
164. Wang, W.; Zhang, C.; Zhang, Z.-W.; Li, Y.-C.; Yasir, M.; Wang, H.-T.; Liu, L. Toughening Fe-based Amorphous Coatings by Reinforcement of Amorphous Carbon. *Sci. Rep.* **2017**, *7*, 4084. [[CrossRef](#)]
165. Tian, W.-P.; Yang, H.-W.; Zhang, S.-D. Synergistic Effect of Mo, W, Mn and Cr on the Passivation Behavior of a Fe-Based Amorphous Alloy Coating. *Acta Met. Sin. (Engl. Lett.)* **2018**, *31*, 308–320. [[CrossRef](#)]
166. Jiao, J.; Luo, Q.; Wei, X.; Wang, Y.; Shen, J. Influence of sealing treatment on the corrosion resistance of Fe-based amorphous coatings in HCl solution. *J. Alloys Compd.* **2017**, *714*, 356–362. [[CrossRef](#)]
167. Wu, J.; Zhang, S.; Sun, W.; Gao, Y.; Wang, J. Enhanced corrosion resistance in Fe-based amorphous coatings through eliminating Cr-depleted zones. *Corros. Sci.* **2018**, *136*, 161–173. [[CrossRef](#)]
168. Cinca, N.; Drehmann, R.; Dietrich, D.; Gaertner, F.; Klassen, T.; Lampke, T.; Guilemany, J.M. Mechanically induced grain refinement, recovery and recrystallization of cold-sprayed iron aluminide coatings. *Surf. Coat. Technol.* **2019**, *380*, 125069. [[CrossRef](#)]
169. Rojas, D.F.; Li, H.; Orhan, O.K.; Shao, C.; Hogan, J.D.; Ponga, M. Mechanical and microstructural properties of a CoCrFe0.75-NiMo0.3Nb0.125 high-entropy alloy additively manufactured via cold-spray. *J. Alloys Compd.* **2022**, *893*, 162309. [[CrossRef](#)]
170. Han, P.; Wang, W.; Liu, Z.; Zhang, T.; Liu, Q.; Guan, X.; Qiao, K.; Ye, D.; Cai, J.; Xie, Y.; et al. Modification of cold-sprayed high-entropy alloy particles reinforced aluminum matrix composites via friction stir processing. *J. Alloys Compd.* **2022**, *907*, 164426. [[CrossRef](#)]
171. Kwon, J.; Park, H.; Lee, I.; Lee, C. Effect of gas flow rate on deposition behavior of Fe-based amorphous alloys in vacuum kinetic spray process. *Surf. Coat. Technol.* **2014**, *259*, 585–593. [[CrossRef](#)]
172. White, B.; Story, W.A.; Brewer, L.; Jordon, J. Fracture mechanics methods for evaluating the adhesion of cold spray deposits. *Eng. Fract. Mech.* **2019**, *205*, 57–69. [[CrossRef](#)]
173. Cavaliere, P.; Perrone, A.; Silvello, A. Crystallization Evolution of Cold-Sprayed Pure Ni Coatings. *J. Therm. Spray Technol.* **2016**, *25*, 1158–1167. [[CrossRef](#)]
174. Sample, C.M.; Champagne, V.K.; Nardi, A.T.; Lados, D.A. Factors governing static properties and fatigue, fatigue crack growth, and fracture mechanisms in cold spray alloys and coatings/repairs: A review. *Addit. Manuf.* **2020**, *36*, 101371. [[CrossRef](#)]
175. Singh, R.; Schrufer, S.; Wilson, S.; Gibmeier, J.; Vassen, R. Influence of coating thickness on residual stress and adhesion-strength of cold-sprayed Inconel 718 coatings. *Surf. Coat. Technol.* **2018**, *350*, 64–73. [[CrossRef](#)]
176. Shi, H.; Liu, M.; Cong, L.; Wang, L. A study on preparation and mechanism of Ni based ternary alloy. *Mater. Express* **2019**, *9*, 681–685. [[CrossRef](#)]
177. Wang, A.P.; Zhang, T.; Wang, J.Q. Ni-based fully amorphous metallic coating with high corrosion resistance. *Philos. Mag. Lett.* **2006**, *86*, 5–11. [[CrossRef](#)]
178. Yoon, S.; Kim, H.J.; Lee, C. Deposition behavior of bulk amorphous NiTiZrSiSn according to the kinetic and thermal energy levels in the kinetic spraying process. *Surf. Coat. Technol.* **2006**, *200*, 6022–6029. [[CrossRef](#)]
179. Wang, A.; Chang, X.; Hou, W.; Wang, J. Preparation and corrosion behaviour of amorphous Ni-based alloy coatings. *Mater. Sci. Eng. A* **2007**, *449–451*, 277–280. [[CrossRef](#)]
180. Yoon, S.; Lee, C.; Choi, H. Evaluation of the effects of the crystallinity of kinetically sprayed Ni–Ti–Zr–Si–Sn bulk metallic glass on the scratch response. *Mater. Sci. Eng. A* **2007**, *449–451*, 285–289. [[CrossRef](#)]
181. Sugita, K.; Matsumoto, M.; Mizuno, M.; Araki, H.; Shirai, Y. Electron irradiation damage and the recovery in a Zr-based bulk amorphous alloy Zr₅₅Cu₃₀Al₁₀Ni₅. *J. Phys. Conf. Ser.* **2008**, *106*, 012024. [[CrossRef](#)]
182. Sun, Y.-S.; Zhang, W.; Kai, W.; Liaw, P.K.; Huang, H.-H. Evaluation of Ni-free Zr–Cu–Fe–Al bulk metallic glass for biomedical implant applications. *J. Alloys Compd.* **2014**, *586*, S539–S543. [[CrossRef](#)]
183. Liu, L.; Qiu, C.; Huang, C.; Yu, Y.; Huang, H.; Zhang, S. Biocompatibility of Ni-free Zr-based bulk metallic glasses. *Intermetallics* **2009**, *17*, 235–240. [[CrossRef](#)]
184. Yeh, J.-W.; Chen, S.K.; Lin, S.-J.; Gan, J.-Y.; Chin, T.-S.; Shun, T.-T.; Tsau, C.-H.; Chang, S.-Y. Nanostructured High-Entropy Alloys with Multiple Principal Elements: Novel Alloy Design Concepts and Outcomes. *Adv. Eng. Mater.* **2004**, *6*, 299–303. [[CrossRef](#)]
185. Akinbami, O.; Mohlala, L.M.; Klenam, D.; van der Merwe, J.; Bodunrin, M. The Status of High Entropy Alloys Studies in Africa: An Overview. *Key Eng. Mater.* **2022**, *917*, 41–53. [[CrossRef](#)]
186. Owen, L.; Jones, N. Quantifying local lattice distortions in alloys. *Scr. Mater.* **2020**, *187*, 428–433. [[CrossRef](#)]

187. Chen, H.; Kauffmann, A.; Laube, S.; Choi, I.-C.; Schwaiger, R.; Huang, Y.; Lichtenberg, K.; Müller, F.; Gorr, B.; Christ, H.-J.; et al. Contribution of Lattice Distortion to Solid Solution Strengthening in a Series of Refractory High Entropy Alloys. *Met. Mater. Trans. A* **2018**, *49*, 772–781. [[CrossRef](#)]
188. Owen, L.R.; Jones, N.G. Lattice distortions in high-entropy alloys. *J. Mater. Res.* **2018**, *33*, 2954–2969. [[CrossRef](#)]
189. Owen, L.; Pickering, E.; Playford, H.; Stone, H.; Tucker, M.; Jones, N. An assessment of the lattice strain in the CrMnFeCoNi high-entropy alloy. *Acta Mater.* **2017**, *122*, 11–18. [[CrossRef](#)]
190. Diao, H.; Santodonato, L.J.; Tang, Z.; Egami, T.; Liaw, P.K. Local Structures of High-Entropy Alloys (HEAs) on Atomic Scales: An Overview. *Jom* **2015**, *67*, 2321–2325. [[CrossRef](#)]
191. Guo, W.; Dmowski, W.; Noh, J.-Y.; Rack, P.; Liaw, P.K.; Egami, T. Local Atomic Structure of a High-Entropy Alloy: An X-Ray and Neutron Scattering Study. *Met. Mater. Trans. A* **2013**, *44*, 1994–1997. [[CrossRef](#)]
192. Santodonato, L.J.; Zhang, Y.; Feygenson, M.; Parish, C.M.; Gao, M.C.; Weber, R.J.; Neuefeind, J.C.; Tang, Z.; Liaw, P.K. Deviation from high-entropy configurations in the atomic distributions of a multi-principal-element alloy. *Nat. Commun.* **2015**, *6*, 5964. [[CrossRef](#)]
193. Abbasi, E.; Luo, Q.; Owens, D. A comparison of microstructure and mechanical properties of low-alloy-medium-carbon steels after quench-hardening. *Mater. Sci. Eng. A* **2018**, *725*, 65–75. [[CrossRef](#)]
194. Ahmady, A.R.; Ekhlasi, A.; Nouri, A.; Nazarpak, M.H.; Gong, P.; Solouk, A. High entropy alloy coatings for biomedical applications: A review. *Smart Mater. Manuf.* **2023**, *1*, 100009. [[CrossRef](#)]
195. Assadi, H.; Kreye, H.; Gärtner, F.; Klassen, T. Cold spraying—A materials perspective. *Acta Mater.* **2016**, *116*, 382–407. [[CrossRef](#)]
196. Ren, Y.; King, P.; Yang, Y.; Xiao, T.; Chu, C.; Gulizia, S.; Murphy, A. Characterization of heat treatment-induced pore structure changes in cold-sprayed titanium. *Mater. Charact.* **2017**, *132*, 69–75. [[CrossRef](#)]
197. Kiplangat, R.S.; Lin, T.-T.; Kipkirui, N.G.; Chen, S.-H. Microstructure and Mechanical Properties of the Plasma-Sprayed and Cold-Sprayed Al_{0.5}CoCrFeNi₂Ti_{0.5} High-Entropy Alloy Coatings. *J. Therm. Spray Technol.* **2022**, *31*, 1207–1221. [[CrossRef](#)]
198. Nikbakht, R.; Assadi, H.; Jodoin, B. Intermetallic Phase Evolution of Cold-Sprayed Ni-Ti Composite Coatings: Influence of As-Sprayed Chemical Composition. *J. Therm. Spray Technol.* **2021**, *30*, 119–130. [[CrossRef](#)]
199. Dai, C.-D.; Fu, Y.; Guo, J.-X.; Du, C.-W. Effects of substrate temperature and deposition time on the morphology and corrosion resistance of FeCoCrNiMo_{0.3} high-entropy alloy coating fabricated by magnetron sputtering. *Int. J. Miner. Met. Mater.* **2020**, *27*, 1388–1397. [[CrossRef](#)]
200. Yin, S.; Li, W.; Song, B.; Yan, X.; Kuang, M.; Xu, Y.; Wen, K.; Lupoi, R. Deposition of FeCoNiCrMn high entropy alloy (HEA) coating via cold spraying. *J. Mater. Sci. Technol.* **2019**, *35*, 1003–1007. [[CrossRef](#)]
201. Cavaliere, P.; Perrone, A.; Silvello, A.; Laska, A.; Blasi, G.; Cano, I.G. Fatigue Bending of V-Notched Cold-Sprayed FeCoCrNiMn Coatings. *Metals* **2022**, *12*, 780. [[CrossRef](#)]
202. Nair, R.B.; Perumal, G.; McDonald, A. Effect of Microstructure on Wear and Corrosion Performance of Thermally Sprayed AlCoCrFeMo High-Entropy Alloy Coatings. *Adv. Eng. Mater.* **2022**, *24*, 2101713. [[CrossRef](#)]
203. Rokni, M.R.; Widener, C.; Champagne, V.R. Microstructural Evolution of 6061 Aluminum Gas-Atomized Powder and High-Pressure Cold-Sprayed Deposition. *J. Therm. Spray Technol.* **2014**, *23*, 514–524. [[CrossRef](#)]
204. Hsu, W.-L.; Yang, Y.-C.; Chen, C.-Y.; Yeh, J.-W. Thermal sprayed high-entropy NiCo_{0.6}Fe_{0.2}Cr_{1.5}SiAlTi_{0.2} coating with improved mechanical properties and oxidation resistance. *Intermetallics* **2017**, *89*, 105–110. [[CrossRef](#)]
205. Ma, X.; Ruggiero, P.; Bhattacharya, R.; Senkov, O.N.; Rai, A.K. Evaluation of New High Entropy Alloy as Thermal Sprayed Bondcoat in Thermal Barrier Coatings. *J. Therm. Spray Technol.* **2022**, *31*, 1011–1020. [[CrossRef](#)]
206. Feng, S.; Guan, S.; Story, W.A.; Ren, J.; Zhang, S.; Te, A.; Gleason, M.A.; Heelan, J.; Walde, C.; Birt, A.; et al. Cold Spray Additive Manufacturing of CoCrFeNiMn High-Entropy Alloy: Process Development, Microstructure, and Mechanical Properties. *J. Therm. Spray Technol.* **2022**, *31*, 1222–1231. [[CrossRef](#)]
207. Lehtonen, J.; Koivuluoto, H.; Ge, Y.; Juselius, A.; Hannula, S.-P. Cold Gas Spraying of a High-Entropy CrFeNiMn Equiatomic Alloy. *Coatings* **2020**, *10*, 53. [[CrossRef](#)]
208. Cheng, J.; Liang, X.; Xu, B. Effect of Nb addition on the structure and mechanical behaviors of CoCrCuFeNi high-entropy alloy coatings. *Surf. Coat. Technol.* **2014**, *240*, 184–190. [[CrossRef](#)]
209. Cheng, J.; Liu, D.; Liang, X.; Chen, Y. Evolution of microstructure and mechanical properties of in situ synthesized TiC-TiB₂/CoCrCuFeNi high entropy alloy coatings. *Surf. Coat. Technol.* **2015**, *281*, 109–116. [[CrossRef](#)]
210. Cheng, J.B.; Liang, X.B.; Wang, Z.H.; Xu, B.S. Formation and Mechanical Properties of CoNiCuFeCr High-Entropy Alloys Coatings Prepared by Plasma Transferred Arc Cladding Process. *Plasma Chem. Plasma Process.* **2013**, *33*, 979–992. [[CrossRef](#)]
211. Lu, J.; Wang, B.; Qiu, X.; Peng, Z.; Ma, M. Microstructure evolution and properties of CrCuFe x NiTi high-entropy alloy coating by plasma cladding on Q235. *Surf. Coat. Technol.* **2017**, *328*, 313–318. [[CrossRef](#)]
212. Cai, Z.; Wang, Y.; Cui, X.; Jin, G.; Li, Y.; Liu, Z.; Dong, M. Design and microstructure characterization of FeCoNiAlCu high-entropy alloy coating by plasma cladding: In comparison with thermodynamic calculation. *Surf. Coat. Technol.* **2017**, *330*, 163–169. [[CrossRef](#)]
213. Fang, Q.; Chen, Y.; Li, J.; Liu, Y.; Liu, Y. Microstructure and mechanical properties of FeCoCrNiNb high-entropy alloy coatings. *Phys. B Condens. Matter* **2018**, *550*, 112–116. [[CrossRef](#)]
214. Xiang, K.; Chen, L.-Y.; Chai, L.; Guo, N.; Wang, H. Microstructural characteristics and properties of CoCrFeNiNbx high-entropy alloy coatings on pure titanium substrate by pulsed laser cladding. *Appl. Surf. Sci.* **2020**, *517*, 146214. [[CrossRef](#)]

215. Chen, L.; Wang, Y.; Hao, X.; Zhang, X.; Liu, H. Lightweight refractory high entropy alloy coating by laser cladding on Ti-6Al-4V surface. *Vacuum* **2021**, *183*, 109823. [[CrossRef](#)]
216. Li, Y.; Liang, H.; Nie, Q.; Qi, Z.; Deng, D.; Jiang, H.; Cao, Z. Microstructures and Wear Resistance of CoCrFeNi₂V_{0.5}Ti_x High-Entropy Alloy Coatings Prepared by Laser Cladding. *Crystals* **2020**, *10*, 352. [[CrossRef](#)]
217. Wu, W.; Jiang, L.; Jiang, H.; Pan, X.; Cao, Z.; Deng, D.; Wang, T.; Li, T. Phase Evolution and Properties of Al₂CrFeNiMo_x High-Entropy Alloys Coatings by Laser Cladding. *J. Therm. Spray Technol.* **2015**, *24*, 1333–1340. [[CrossRef](#)]
218. Zhang, H.; Pan, Y.; He, Y.; Jiao, H. Microstructure and properties of 6FeNiCoSiCrAlTi high-entropy alloy coating prepared by laser cladding. *Appl. Surf. Sci.* **2011**, *257*, 2259–2263. [[CrossRef](#)]
219. Gu, Z.; Mao, P.; Gou, Y.; Chao, Y.; Xi, S. Microstructure and properties of MgMoNbFeTi₂Y_x high entropy alloy coatings by laser cladding. *Surf. Coat. Technol.* **2020**, *402*, 126303. [[CrossRef](#)]
220. Qiu, X.; Zhang, Y.; Liu, C. Effect of Ti content on structure and properties of Al₂CrFeNiCoCuTi_x high-entropy alloy coatings. *J. Alloys Compd.* **2014**, *585*, 282–286. [[CrossRef](#)]
221. Li, X.; Feng, Y.; Liu, B.; Yi, D.; Yang, X.; Zhang, W.; Chen, G.; Liu, Y.; Bai, P. Influence of NbC particles on microstructure and mechanical properties of AlCoCrFeNi high-entropy alloy coatings prepared by laser cladding. *J. Alloys Compd.* **2019**, *788*, 485–494. [[CrossRef](#)]
222. Qiu, X. Microstructure, hardness and corrosion resistance of Al₂CoCrCuFeNiTi_x high-entropy alloy coatings prepared by rapid solidification. *J. Alloys Compd.* **2018**, *735*, 359–364. [[CrossRef](#)]
223. Zhang, H.; Pan, Y.; He, Y.-Z. Synthesis and characterization of FeCoNiCrCu high-entropy alloy coating by laser cladding. *Mater. Des.* **2011**, *32*, 1910–1915. [[CrossRef](#)]
224. Ni, C.; Shi, Y.; Liu, J.; Huang, G. Characterization of Al_{0.5}FeCu_{0.7}NiCoCr high-entropy alloy coating on aluminum alloy by laser cladding. *Opt. Laser Technol.* **2018**, *105*, 257–263. [[CrossRef](#)]
225. Shu, F.; Wu, L.; Zhao, H.; Sui, S.; Zhou, L.; Zhang, J.; He, W.; He, P.; Xu, B. Microstructure and high-temperature wear mechanism of laser clad CoCrBFeNiSi high-entropy alloy amorphous coating. *Mater. Lett.* **2018**, *211*, 235–238. [[CrossRef](#)]
226. Shu, F.; Zhang, B.; Liu, T.; Sui, S.; Liu, Y.; He, P.; Liu, B.; Xu, B. Effects of laser power on microstructure and properties of laser clad CoCrBFeNiSi high-entropy alloy amorphous coatings. *Surf. Coat. Technol.* **2019**, *358*, 667–675. [[CrossRef](#)]
227. Jiang, Y.; Li, J.; Juan, Y.; Lu, Z.; Jia, W. Evolution in microstructure and corrosion behavior of AlCoCrFeNi high-entropy alloy coatings fabricated by laser cladding. *J. Alloys Compd.* **2019**, *775*, 1–14. [[CrossRef](#)]
228. Zhang, H.; Wu, W.; He, Y.; Li, M.; Guo, S. Formation of core-shell structure in high entropy alloy coating by laser cladding. *Appl. Surf. Sci.* **2016**, *363*, 543–547. [[CrossRef](#)]
229. Guo, Y.; Shang, X.; Liu, Q. Microstructure and properties of in-situ TiN reinforced laser cladding CoCr₂FeNiTi high-entropy alloy composite coatings. *Surf. Coat. Technol.* **2018**, *344*, 353–358. [[CrossRef](#)]
230. Guo, Y.; Liu, Q. MoFeCrTiWAlNb refractory high-entropy alloy coating fabricated by rectangular-spot laser cladding. *Intermetallics* **2018**, *102*, 78–87. [[CrossRef](#)]
231. Chao, Q.; Guo, T.; Jarvis, T.; Wu, X.; Hodgson, P.; Fabijanic, D. Direct laser deposition cladding of Al CoCrFeNi high entropy alloys on a high-temperature stainless steel. *Surf. Coat. Technol.* **2017**, *332*, 440–451. [[CrossRef](#)]
232. Juan, Y.; Li, J.; Jiang, Y.; Jia, W.; Lu, Z. Modified criterions for phase prediction in the multi-component laser-clad coatings and investigations into microstructural evolution/wear resistance of FeCrCoNiAlMox laser-clad coatings. *Appl. Surf. Sci.* **2019**, *465*, 700–714. [[CrossRef](#)]
233. Shu, F.; Yang, B.; Dong, S.; Zhao, H.; Xu, B.; Xu, F.; Liu, B.; He, P.; Feng, J. Effects of Fe-to-Co ratio on microstructure and mechanical properties of laser clad FeCoCrBNiSi high-entropy alloy coatings. *Appl. Surf. Sci.* **2018**, *450*, 538–544. [[CrossRef](#)]
234. Cai, Z.; Cui, X.; Jin, G.; Liu, Z.; Zheng, W.; Li, Y.; Wang, L. Microstructure and thermal stability of a Ni-Cr-Co-Ti-V-Al high-entropy alloy coating by laser surface alloying. *Met. Mater. Int.* **2017**, *23*, 1012–1018. [[CrossRef](#)]
235. Cai, Z.; Jin, G.; Cui, X.; Liu, Z.; Zheng, W.; Li, Y.; Wang, L. Synthesis and microstructure characterization of Ni-Cr-Co-Ti-V-Al high entropy alloy coating on Ti-6Al-4V substrate by laser surface alloying. *Mater. Charact.* **2016**, *120*, 229–233. [[CrossRef](#)]
236. Zhang, S.; Wu, C.; Zhang, C.; Guan, M.; Tan, J. Laser surface alloying of FeCoCrAlNi high-entropy alloy on 304 stainless steel to enhance corrosion and cavitation erosion resistance. *Opt. Laser Technol.* **2016**, *84*, 23–31. [[CrossRef](#)]
237. Zhang, S.; Wu, C.; Yi, J.; Zhang, C. Synthesis and characterization of FeCoCrAlCu high-entropy alloy coating by laser surface alloying. *Surf. Coat. Technol.* **2015**, *262*, 64–69. [[CrossRef](#)]
238. Ye, Q.; Feng, K.; Li, Z.; Lu, F.; Li, R.; Huang, J.; Wu, Y. Microstructure and corrosion properties of CrMnFeCoNi high entropy alloy coating. *Appl. Surf. Sci.* **2017**, *396*, 1420–1426. [[CrossRef](#)]
239. Zhang, S.; Wu, C.; Zhang, C. Phase evolution characteristics of FeCoCrAlCuV_xNi high entropy alloy coatings by laser high-entropy alloying. *Mater. Lett.* **2015**, *141*, 7–9. [[CrossRef](#)]
240. Wu, C.; Zhang, S.; Zhang, C.; Zhang, H.; Dong, S. Phase evolution and properties in laser surface alloying of FeCoCrAlCuNi high-entropy alloy on copper substrate. *Surf. Coat. Technol.* **2017**, *315*, 368–376. [[CrossRef](#)]
241. Smyrnova, K.V.; Pogrebnjak, A.D.; Beresnev, V.M.; Litovchenko, S.V.; Borba-Pogrebnjak, S.O.; Manokhin, A.S.; Klimenko, S.A.; Zhollybekov, B.; Kupchishin, A.I.; Kravchenko, Y.O.; et al. Microstructure and Physical-Mechanical Properties of (TiAlSiY)N Nanostructured Coatings Under Different Energy Conditions. *Met. Mater. Int.* **2018**, *24*, 1024–1035. [[CrossRef](#)]

242. Pogrebnyak, A.; Yakushchenko, I.V.; Bondar, O.; Beresnev, V.M.; Oyoshi, K.; Ivasishin, O.M.; Amekura, H.; Takeda, Y.; Opielak, M.; Kozak, C. Irradiation resistance, microstructure and mechanical properties of nanostructured (TiZrHfVNbTa)N coatings. *J. Alloys Compd.* **2016**, *679*, 155–163. [[CrossRef](#)]
243. Yu, X.; Wang, J.; Wang, L.; Huang, W. Fabrication and characterization of CrNbSiTiZr high-entropy alloy films by radio-frequency magnetron sputtering via tuning substrate bias. *Surf. Coat. Technol.* **2021**, *412*, 127074. [[CrossRef](#)]
244. Wang, J.; Kuang, S.; Yu, X.; Wang, L.; Huang, W. Tribo-mechanical properties of CrNbTiMoZr high-entropy alloy film synthesized by direct current magnetron sputtering. *Surf. Coat. Technol.* **2020**, *403*, 126374. [[CrossRef](#)]
245. Alvi, S.; Jarzabek, D.M.; Kohan, M.G.; Hedman, D.; Jencyk, P.; Natile, M.M.; Vomiero, A.; Akhtar, F. Synthesis and Mechanical Characterization of a CuMoTaWV High-Entropy Film by Magnetron Sputtering. *ACS Appl. Mater. Interfaces* **2020**, *12*, 21070–21079. [[CrossRef](#)]
246. Li, X.; Zheng, Z.; Dou, D.; Li, J. Microstructure and Properties of Coating of FeAlCuCrCoMn High Entropy Alloy Deposited by Direct Current Magnetron Sputtering. *Mater. Res.* **2016**, *19*, 802–806. [[CrossRef](#)]
247. Cao, F.; Munroe, P.; Zhou, Z.; Xie, Z. Microstructure and mechanical properties of a multilayered CoCrNi/Ti coating with varying crystal structure. *Surf. Coat. Technol.* **2018**, *350*, 596–602. [[CrossRef](#)]
248. Braic, V.; Vladescu, A.; Balaceanu, M.; Luculescu, C.; Braic, M. Nanostructured multi-element (TiZrNbHfTa)N and (TiZrNbHfTa)C hard coatings. *Surf. Coat. Technol.* **2012**, *211*, 117–121. [[CrossRef](#)]
249. Zhang, W.; Tang, R.; Yang, Z.; Liu, C.; Chang, H.; Yang, J.; Liao, J.; Yang, Y.; Liu, N. Preparation, structure, and properties of an AlCrMoNbZr high-entropy alloy coating for accident-tolerant fuel cladding. *Surf. Coat. Technol.* **2018**, *347*, 13–19. [[CrossRef](#)]
250. Lin, C.; Duh, J. Corrosion behavior of (Ti–Al–Cr–Si–V)_xN_y coatings on mild steels derived from RF magnetron sputtering. *Surf. Coat. Technol.* **2008**, *203*, 558–561. [[CrossRef](#)]
251. Huang, P.-K.; Yeh, J.-W. Effects of nitrogen content on structure and mechanical properties of multi-element (AlCrNbSiTiV)N coating. *Surf. Coat. Technol.* **2009**, *203*, 1891–1896. [[CrossRef](#)]
252. Ren, B.; Shen, Z.; Liu, Z. Structure and mechanical properties of multi-element (AlCrMnMoNiZr)N_x coatings by reactive magnetron sputtering. *J. Alloys Compd.* **2013**, *560*, 171–176. [[CrossRef](#)]
253. Tsai, D.-C.; Deng, M.-J.; Chang, Z.-C.; Kuo, B.-H.; Chen, E.-C.; Chang, S.-Y.; Shieu, F.-S. Oxidation resistance and characterization of (AlCrMoTaTi)-Six-N coating deposited via magnetron sputtering. *J. Alloys Compd.* **2015**, *647*, 179–188. [[CrossRef](#)]
254. Johansson, K.; Riekehr, L.; Fritze, S.; Lewin, E. Multicomponent Hf-Nb-Ti-V-Zr nitride coatings by reactive magnetron sputter deposition. *Surf. Coat. Technol.* **2018**, *349*, 529–539. [[CrossRef](#)]
255. Tüten, N.; Canadinc, D.; Motallebzadeh, A.; Bal, B. Microstructure and tribological properties of TiTaHfNbZr high entropy alloy coatings deposited on Ti 6Al 4V substrates. *Intermetallics* **2019**, *105*, 99–106. [[CrossRef](#)]
256. Alamdari, A.A.; Unal, U.; Motallebzadeh, A. Investigation of microstructure, mechanical properties, and biocorrosion behavior of Ti1.5ZrTa0.5Nb0.5W0.5 refractory high-entropy alloy film doped with Ag nanoparticles. *Surf. Interfaces* **2022**, *28*, 101617. [[CrossRef](#)]
257. Chen, L.; Bobzin, K.; Zhou, Z.; Zhao, L.; Öte, M.; Königstein, T.; Tan, Z.; He, D. Wear behavior of HVOF-sprayed Al_{0.6}TiCrFeCoNi high entropy alloy coatings at different temperatures. *Surf. Coat. Technol.* **2019**, *358*, 215–222. [[CrossRef](#)]
258. Löbel, M.; Lindner, T.; Lampke, T. High-temperature wear behaviour of AlCoCrFeNiTi_{0.5} coatings produced by HVOF. *Surf. Coat. Technol.* **2020**, *403*, 126379. [[CrossRef](#)]
259. Abhijith, N.V.; Kumar, D.; Kalyansundaram, D. Development of Single-Stage TiNbMoMnFe High-Entropy Alloy Coating on 304L Stainless Steel Using HVOF Thermal Spray. *J. Therm. Spray Technol.* **2022**, *31*, 1032–1044. [[CrossRef](#)]
260. Hsu, W.-L.; Murakami, H.; Yeh, J.-W.; Yeh, A.-C.; Shimoda, K. On the study of thermal-sprayed Ni 0.2 Co 0.6 Fe 0.2 CrSi 0.2 AlTi 0.2 HEA overlay coating. *Surf. Coat. Technol.* **2017**, *316*, 71–74. [[CrossRef](#)]
261. Tian, L.; Feng, Z.; Xiong, W. Microstructure, Microhardness, and Wear Resistance of AlCoCrFeNiTi/Ni₆₀ Coating by Plasma Spraying. *Coatings* **2018**, *8*, 112. [[CrossRef](#)]
262. Wang, W.; Qi, W.; Xie, L.; Yang, X.; Li, J.; Zhang, Y. Microstructure and Corrosion Behavior of (CoCrFeNi)₉₅Nb₅ High-Entropy Alloy Coating Fabricated by Plasma Spraying. *Materials* **2019**, *12*, 694. [[CrossRef](#)]
263. Ang, A.S.M.; Berndt, C.C.; Sesso, M.L.; Anupam, A.; Praveen, S.; Kottada, R.S.; Murty, B.S. Plasma-Sprayed High Entropy Alloys: Microstructure and Properties of AlCoCrFeNi and MnCoCrFeNi. *Metall. Mater. Trans. A* **2015**, *46*, 791–800. [[CrossRef](#)]
264. Xiao, J.-K.; Tan, H.; Wu, Y.-Q.; Chen, J.; Zhang, C. Microstructure and wear behavior of FeCoNiCrMn high entropy alloy coating deposited by plasma spraying. *Surf. Coat. Technol.* **2020**, *385*, 125430. [[CrossRef](#)]
265. Xiao, J.-K.; Wu, Y.-Q.; Chen, J.; Zhang, C. Microstructure and tribological properties of plasma sprayed FeCoNiCrSiAl_x high entropy alloy coatings. *Wear* **2020**, *448–449*, 203209. [[CrossRef](#)]
266. Anupam, A.; Kottada, R.S.; Kashyap, S.; Meghwal, A.; Murty, B.; Berndt, C.; Ang, A. Understanding the microstructural evolution of high entropy alloy coatings manufactured by atmospheric plasma spray processing. *Appl. Surf. Sci.* **2020**, *505*, 144117. [[CrossRef](#)]
267. Wang, L.; Chen, C.; Yeh, J.; Ke, S. The microstructure and strengthening mechanism of thermal spray coating Ni_xCo_{0.6}Fe_{0.2}CrySi_zAlTi_{0.2} high-entropy alloys. *Mater. Chem. Phys.* **2011**, *126*, 880–885. [[CrossRef](#)]
268. Tian, L.-H.; Xiong, W.; Liu, C.; Lu, S.; Fu, M. Microstructure and Wear Behavior of Atmospheric Plasma-Sprayed AlCoCrFeNiTi High-Entropy Alloy Coating. *J. Mater. Eng. Perform.* **2016**, *25*, 5513–5521. [[CrossRef](#)]

269. Anupam, A.; Kumar, S.; Chavan, N.M.; Murty, B.S.; Kottada, R.S. First report on cold-sprayed AlCoCrFeNi high-entropy alloy and its isothermal oxidation. *J. Mater. Res.* **2019**, *34*, 796–806. [[CrossRef](#)]
270. Hushchuk, D.V.; Yurkova, A.I.; Cherniavsky, V.V.; Bilyk, I.I.; Nakonechnyy, S.O. Nanostructured AlNiCoFeCrTi high-entropy coating performed by cold spray. *Appl. Nanosci.* **2020**, *10*, 4879–4890. [[CrossRef](#)]
271. Zou, Y. Cold Spray Additive Manufacturing: Microstructure Evolution and Bonding Features. *Acc. Mater. Res.* **2021**, *2*, 1071–1081. [[CrossRef](#)]
272. Nikbakht, R.; Saadati, M.; Kim, T.-S.; Jahazi, M.; Kim, H.S.; Jodoin, B. Cold spray deposition characteristic and bonding of CrMnCoFeNi high entropy alloy. *Surf. Coat. Technol.* **2021**, *425*, 127748. [[CrossRef](#)]
273. Xu, Y.; Li, W.; Qu, L.; Yang, X.; Song, B.; Lupoi, R.; Yin, S. Solid-state cold spraying of FeCoCrNiMn high-entropy alloy: An insight into microstructure evolution and oxidation behavior at 700–900 °C. *J. Mater. Sci. Technol.* **2021**, *68*, 172–183. [[CrossRef](#)]
274. Yurkova, A.I.; Hushchuk, D.V.; Minitsky, A.V. Synthesis of High-Entropy AlNiCoFeCrTi Coating by Cold Spraying. *Powder Met. Met. Ceram.* **2021**, *59*, 681–694. [[CrossRef](#)]
275. Ahn, J.-E.; Kim, Y.-K.; Yoon, S.-H.; Lee, K.-A. Tuning the Microstructure and Mechanical Properties of Cold Sprayed Equiatomic CoCrFeMnNi High-Entropy Alloy Coating Layer. *Met. Mater. Int.* **2021**, *27*, 2406–2415. [[CrossRef](#)]
276. Lordejani, A.A.; Colzani, D.; Guagliano, M.; Bagherifard, S. An inclusive numerical framework to assess the role of feedstock features on the quality of cold spray deposits. *Mater. Des.* **2022**, *224*, 111374. [[CrossRef](#)]
277. Nikbakht, R.; Cojocar, C.V.; Aghasibeig, M.; Irissou, É.; Kim, T.-S.; Kim, H.S.; Jodoin, B. Cold Spray and Laser-Assisted Cold Spray of CrMnCoFeNi High Entropy Alloy Using Nitrogen as the Propelling Gas. *J. Therm. Spray Technol.* **2022**, *31*, 1129–1142. [[CrossRef](#)]
278. Sova, A.; Doubenskaia, M.; Trofimov, E.; Samodurova, M. Deposition of High-Entropy Alloy Coating by Cold Spray Combined with Laser Melting: Feasibility Tests. *J. Therm. Spray Technol.* **2022**, *31*, 1112–1128. [[CrossRef](#)]
279. Han, P.; Lin, J.; Wang, W.; Liu, Z.; Xiang, Y.; Zhang, T.; Liu, Q.; Guan, X.; Qiao, K.; Xie, Y.; et al. Friction Stir Processing of Cold-Sprayed High-Entropy Alloy Particles Reinforced Aluminum Matrix Composites: Corrosion and Wear Properties. *Met. Mater. Int.* **2022**, *29*, 845–860. [[CrossRef](#)]
280. Silvello, A.; Cavaliere, P.; Yin, S.; Lupoi, R.; Cano, I.G.; Dosta, S. Microstructural, Mechanical and Wear Behavior of HVOF and Cold-Sprayed High-Entropy Alloys (HEAs) Coatings. *J. Therm. Spray Technol.* **2022**, *31*, 1184–1206. [[CrossRef](#)]
281. Feng, L.; Yang, W.-J.; Ma, K.; Yuan, Y.-D.; An, G.-S.; Li, W.-S. Microstructure and Properties of Cold Spraying AlCoCrCuFeNi HEA Coatings Synthesized by Induction Remelting. *Mater. Technol.* **2022**, *37*, 2567–2579. [[CrossRef](#)]
282. Zou, Y.; Qiu, Z.; Huang, C.; Zeng, D.; Lupoi, R.; Zhang, N.; Yin, S. Microstructure and tribological properties of Al₂O₃ reinforced FeCoNiCrMn high entropy alloy composite coatings by cold spray. *Surf. Coat. Technol.* **2022**, *434*, 128205. [[CrossRef](#)]
283. Yu, P.; Fan, N.; Zhang, Y.; Wang, Z.; Li, W.; Lupoi, R.; Yin, S. Microstructure evolution and composition redistribution of FeCoNiCrMn high entropy alloy under extreme plastic deformation. *Mater. Res. Lett.* **2022**, *10*, 124–132. [[CrossRef](#)]
284. Zhu, J.; Cheng, X.; Zhang, L.; Hui, X.; Wu, Y.; Zheng, H.; Ren, Z.; Zhao, Y.; Wang, W.; Zhu, S.; et al. Microstructures, wear resistance and corrosion resistance of CoCrFeNi high entropy alloys coating on AZ91 Mg alloy prepared by cold spray. *J. Alloys Compd.* **2022**, *925*, 166698. [[CrossRef](#)]
285. Akisin, C.J.; Bennett, C.J.; Venturi, F.; Assadi, H.; Hussain, T. Numerical and Experimental Analysis of the Deformation Behavior of CoCrFeNiMn High Entropy Alloy Particles onto Various Substrates During Cold Spraying. *J. Therm. Spray Technol.* **2022**, *31*, 1085–1111. [[CrossRef](#)]
286. Zehtabi, N.P.; Lordejani, A.A.; Guagliano, M.; Bagherifard, S. Numerical Simulation of Cold Spray Bonding for CrFeNi Medium-Entropy Alloy. *Adv. Eng. Mater.* **2022**, *24*, 2200603. [[CrossRef](#)]
287. Mahaffey, J.; Vackel, A.; Whetten, S.; Melia, M.; Kustas, A.B. Structure Evolution and Corrosion Performance of CoCrFeMnNi High Entropy Alloy Coatings Produced Via Plasma Spray and Cold Spray. *J. Therm. Spray Technol.* **2022**, *31*, 1143–1154. [[CrossRef](#)]
288. Supekar, R.; Nair, R.B.; McDonald, A.; Stoyanov, P. Sliding wear behavior of high entropy alloy coatings deposited through cold spraying and flame spraying: A comparative assessment. *Wear* **2023**, *516–517*, 204596. [[CrossRef](#)]
289. Yuan, Z.; Tian, W.; Li, F.; Fu, Q.; Hu, Y.; Wang, X. Microstructure and properties of high-entropy alloy reinforced aluminum matrix composites by spark plasma sintering. *J. Alloys Compd.* **2019**, *806*, 901–908. [[CrossRef](#)]
290. Lu, F.-F.; Ma, K.; Li, C.-X.; Yasir, M.; Luo, X.-T.; Li, C.-J. Enhanced corrosion resistance of cold-sprayed and shot-peened aluminum coatings on LA43M magnesium alloy. *Surf. Coat. Technol.* **2020**, *394*, 125865. [[CrossRef](#)]
291. Marzbanrad, B.; Toyserkani, E.; Jahed, H. Characterization of single- and multilayer cold-spray coating of Zn on AZ31B. *Surf. Coat. Technol.* **2021**, *416*, 127155. [[CrossRef](#)]
292. Yao, H.-L.; Yi, Z.-H.; Yao, C.; Zhang, M.-X.; Wang, H.-T.; Li, S.-B.; Bai, X.-B.; Chen, Q.-Y.; Ji, G.-C. Improved corrosion resistance of AZ91D magnesium alloy coated by novel cold-sprayed Zn-HA/Zn double-layer coatings. *Ceram. Int.* **2020**, *46*, 7687–7693. [[CrossRef](#)]
293. Siddique, S.; Bernussi, A.A.; Husain, S.W.; Yasir, M. Enhancing structural integrity, corrosion resistance and wear properties of Mg alloy by heat treated cold sprayed Al coating. *Surf. Coat. Technol.* **2020**, *394*, 125882. [[CrossRef](#)]
294. Xiong, Y.; Zhang, M.-X. The effect of cold sprayed coatings on the mechanical properties of AZ91D magnesium alloys. *Surf. Coat. Technol.* **2014**, *253*, 89–95. [[CrossRef](#)]
295. Dayani, S.; Shaha, S.; Ghelichi, R.; Wang, J.; Jahed, H. The impact of AA7075 cold spray coating on the fatigue life of AZ31B cast alloy. *Surf. Coat. Technol.* **2018**, *337*, 150–158. [[CrossRef](#)]

296. Tao, Y.; Xiong, T.; Sun, C.; Kong, L.; Cui, X.; Li, T.; Song, G.-L. Microstructure and corrosion performance of a cold sprayed aluminium coating on AZ91D magnesium alloy. *Corros. Sci.* **2010**, *52*, 3191–3197. [[CrossRef](#)]
297. Mušálek, R.; Kovářík, O.; Matějčík, J. In-situ observation of crack propagation in thermally sprayed coatings. *Surf. Coat. Technol.* **2010**, *205*, 1807–1811. [[CrossRef](#)]
298. Klenam, D.E.P.; Bodunrin, M.O.; Akromah, S.; Gikunoo, E.; Andrews, A.; McBagonluri, F. Ferrous materials degradation: Characterisation of rust by colour—An overview. *Corros. Rev.* **2021**, *39*, 297–311. [[CrossRef](#)]
299. Bodunrin, M.O.; Chown, L.H.; van der Merwe, J.W.; Alaneme, K.K.; Oganbule, C.; Klenam, D.E.P.; Mphasha, N.P. Corrosion behavior of titanium alloys in acidic and saline media: Role of alloy design, passivation integrity, and electrolyte modification. *Corros. Rev.* **2020**, *38*, 25–47. [[CrossRef](#)]
300. Klenam, D.E.P.; Chown, L.H.; Papo, J.M.; Smith, M.; Cornish, L.A. Corrosion and Mechanical Behaviour of Typical Railway Axle Steels in Water. *Afr. Corros. J.* **2016**, *2*, 1–10.
301. Thurn, G.; Schneider, G.A.; Aldinger, F. High-temperature deformation of plasma-sprayed ZrO₂ thermal barrier coatings. *Mater. Sci. Eng. A* **1997**, *233*, 176–182. [[CrossRef](#)]

Disclaimer/Publisher’s Note: The statements, opinions and data contained in all publications are solely those of the individual author(s) and contributor(s) and not of MDPI and/or the editor(s). MDPI and/or the editor(s) disclaim responsibility for any injury to people or property resulting from any ideas, methods, instructions or products referred to in the content.